Unraveling the Neural Networks of Consumption: Novel Central Pathways in Feeding Control and Weight Loss

Elizabeth N. Godschall

Peabody, MA, USA

B.S. in Biology, University of Richmond, 2020

A Dissertation Presented to the Graduate Faculty of the University of Virginia in Candidacy for the Degree of Doctor of Philosophy

Department of Biology

University of Virginia

March 2025

Committee Members:
Ali D. Güler
John Campbell
Ignacio Provencio
Christopher Deppmann
Edward Nieh

Abstract

The regulation of feeding behavior and energy homeostasis involves complex interactions between circadian biology, neurobiology, and metabolic signaling. In these studies, we first provide key insights into the neurocircuitry underlying food entrainment. We developed the first single-nucleus RNA sequencing atlas of the dorsomedial hypothalamus (DMH), identifying DMH^{Lepr} neurons to play a critical role in orchestrating food anticipatory activity. Next, we investigate the mechanisms by which glucagon-like peptide 1 receptor agonists (GLP1RAs) influence feeding behavior and neuromodulatory networks. By generating novel $Glp1r^{S33W}$ mouse models expressing humanized GLP1R, we demonstrate that small-molecule and peptide GLP1RAs induce comparable effects in glucose dynamics, feeding, and behavioral patterns. We provide evidence that small-molecule GLP1RAs can directly access blood-brain barrier-impermeable regions such as the central amygdala (CeA), a discovery with significant implications for the treatment of brain-related disorders. Lastly, we identify CeA^{Glp1r} neurons as key modulators of mesolimbic dopamine release in response to highly palatable foods. These findings provide fundamental insights into the neurobiology of feeding and offer a framework for optimizing next-generation GLP1RA therapies for metabolic and neurological disorders.

Dedication

This work is dedicated to the army of people that helped me explore exciting science and stay sane throughout the PhD process. I have to especially thank the many mice who were sacrificed in the name of science, without them none of this would have been possible. I am eternally grateful for the mentorship I received from Ali Güler and John Campbell, along with the constant support I got from Qijun Tang during my first years. I am thankful for all of my labmates and undergraduates, without them science would not have been quite as fun and rewarding.

I wouldn't have made it without the constant love, support, and daily phone calls from my biggest cheerleaders, my mom and dad, along with my sister Sarah who has been my role model my entire life. I am forever thankful for love and support from my partner in everything, Matt, who has been by my side throughout this whole journey, and I can't wait for our next adventures together. I am grateful to all of my family and friends who have brought me so much joy and I could go on forever for the amount of people I could acknowledge. I am fortunate to have such a huge web of love and support.

Table of Contents

Preface

A complex interplay of cellular processes, signaling hormones, circuits, and pathways regulates hunger, energy balance, and metabolism. Homeostatic, hedonic, and circadian systems work both independently and together to shape feeding behavior and metabolic patterns. In obesity, many of these regulatory mechanisms become dysregulated, yet the precise ways they fail and how to restore them remain active areas of investigation. In this dissertation, I first examine how the dorsomedial hypothalamus contributes to circadian-mediated food entrainment utilizing single nuclei RNA-sequencing (Chapter 2). Next, I investigate the effects of next-generation oral GLP1R agonists on feeding and behavioral patterns, neural activity, and reward responses (Chapter 3). Finally, I explore how the circadian timing of GLP1R agonist administration influences consummatory behavior and weight loss outcomes (Addendum 1). These findings reveal key neural and hormonal mechanisms underlying feeding behavior, obesity, and GLP1R action, contributing to ongoing research aimed at developing more effective, time-sensitive interventions for metabolic health.

Chapter 1: Introduction

C1.1 Homeostatic, hedonic, and circadian control of feeding and metabolism

Homeostatic Driven Feeding

Energy homeostasis, a fundamental drive essential for survival, is a process largely conserved across all life forms—from bacteria to humans (*1*, *2*). While feeding is tightly regulated and critical for maintaining this balance, modern Western lifestyles have disrupted these homeostatic mechanisms, contributing to a significant burden of obesity and related metabolic disorders (*3*). From an evolutionary perspective, conserving caloric excess as fat was advantageous during the hunter-gatherer era, when food was scarce and the timing of the next meal was unpredictable. However, in today's developed world where calorie-dense and ultra-processed foods are readily available at all hours, this once-beneficial adaptation has become a liability (*4*, *5*). Our metabolic processes are ill-equipped to handle the constant access to high-calorie foods, driving the current obesity epidemic. According to the Centers for Disease Control and Prevention, nearly 50% of adult Americans are now classified as overweight or obese, underscoring the urgent need to address this growing public health challenge (*6*) .

The regulation of energy homeostasis involves a complex interplay between central and peripheral modulators (*7*), which work in unison to relay energy related information to the brain. In the periphery, gastric, intestinal, pancreatic, and adipose-derived metabolites respond dynamically to energy states, meals, and varying food compositions (*8*). In low-energy states, the stomach secretes ghrelin, a hormone that acts on the hypothalamus to stimulate hunger (*9*), along with motilin, which triggers the stomach "growls" associated with hunger (*10*). After a meal, the intestines release a variety of hormones, including glucagon-like peptide-1 (GLP-1), glucose-dependent insulinotropic polypeptide (GIP), oxyntomodulin (OXM), cholecystokinin (CCK), peptide YY (PYY), and serotonin (5-HT). GLP-1, GIP, and OXM, collectively known as

incretin hormones, play key roles in promoting satiety, slowing gastric emptying, and stimulating glucose-dependent insulin secretion by the pancreas (*11*, *12*). Interestingly, both GLP-1 and OXM are derived from the cleavage of proglucagon (*13*). These hormones are the foundation for many current treatments for type II diabetes and obesity (*14*, *15*). CCK and PYY also contribute to feelings of fullness by slowing gastric emptying and interacting with receptors in the brain to suppress appetite (*16*). Serotonin (5-HT), released after feeding by enterochromaffin cells lining the intestines, regulates nutrient absorption, storage, blood glucose levels, and intestinal motility (*17*). Together, these peripheral signals ensure precise communication with the brain to maintain energy balance.

Beyond the gastrointestinal tract, the pancreas and adipose tissue play crucial roles in generating hormonal and metabolic signals to convey energy states. The pancreas, which is highly sensitive to fluctuations in blood sugar levels, produces key hormones to regulate energy balance. Beta cells secrete insulin to lower blood sugar, while alpha cells release glucagon to raise it (*18*). Additionally, pancreatic polypeptide, produced by PP cells, controls the release of insulin and glucagon to modulate feeding behavior (*19*). White adipose tissue (WAT) also contributes significantly to energy regulation by releasing leptin and adiponectin. After feeding, leptin acts as a long-term satiety signal by targeting hunger-related regions in the brain to suppress appetite (*20*–*23*). Meanwhile, adiponectin enhances metabolism by improving insulin sensitivity and promoting energy expenditure (*24*–*26*). These hormonal interactions establish a dynamic, inter-organ communication network between the periphery and the brain, effectively creating an internal "energy meter" to maintain homeostasis.

Central regulators of energy homeostasis are extensive, with the brain integrating both central and peripheral signals to determine the body’s energy needs (*27*). Key brain regions involved in homeostatic feeding regulation include the hypothalamus and the hindbrain (*28*, *29*). These

areas not only process signals from peripheral hormones, but also produce their own neuropeptides and neurotransmitters to influence feeding behaviors.

In the arcuate nucleus of the hypothalamus, agouti-related peptide (AgRP) and neuropeptide Y (NPY) neurons act as potent stimulators of hunger (*30*–*32*). In contrast, pro-opiomelanocortin (POMC) neurons activate the melanocortin system to strongly inhibit feeding and promote satiety (*33*). The hindbrain also contributes to this regulation by producing hormones such as GLP-1, CCK, and NPY, which relay energy state-dependent information to other brain regions to influence food-seeking motivation and satiety (*34*–*38*). Serotonin (5-HT), a hormone also produced peripherally, plays a critical role in central homeostatic feeding regulation (*39*). Within the brain, 5-HT is released from the dorsal raphe nucleus (DRN) following food consumption (*40*, *41*). It reduces appetite and increases thermogenesis by signaling to orexigenic (hunger-promoting) and anorectic (satiety-promoting) populations in the hypothalamus (*42*). Conversely, low levels of DRN-derived serotonin are characteristic of hunger states, further emphasizing its dual role in balancing energy homeostasis. This tightly coordinated network ensures the brain integrates both internal and external cues, maintaining energy balance.

Reward Driven Feeding

While homeostatic feeding is driven by the physiological need to maintain energy balance, hedonic feeding is motivated by the reward value of food, independent of energy state (*43*). The highly palatable, carbohydrate- and fat-rich foods prevalent in Western societies today activate the mesolimbic dopamine system in a manner similar to addictive substances like cocaine or methamphetamine (*44*–*47*). Hedonic feeding primarily operates through dopamine-producing neurons in the ventral tegmental area (VTA), which project to the nucleus accumbens (NAc), enabling the processing and reinforcement of pleasurable stimuli (*48*). The amygdala and

prefrontal cortex also contribute to the mesolimbic dopamine system, driving executive and motivational functions that reinforce the consumption of highly palatable foods.

The lateral hypothalamus, the site of hypocretin (orexin)-producing neurons, plays a dual role in regulating both appetite and reward-driven behaviors (*49*). While orexin neurons respond to homeostatic cues like ghrelin to amplify hunger, they also enhance motivation for highly palatable foods (*50*–*52*). These neurons project to the VTA, increasing dopamine release in response to food rewards and amplifying their hedonic value. Notably, orexins are also implicated in drug-seeking behavior, linking them to the mesolimbic reward circuit (*53*–*55*).

The endocannabinoid system also plays a key role in hedonic feeding, primarily through activation of cannabinoid receptor 1 (CB1) (*56*–*58*) . CB1 activation stimulates appetite, enhances the hedonic appeal of palatable foods, and drives the well-known phenomenon of the "munchies" (*59*–*61*). Beyond feeding, the endocannabinoid system can relieve pain, inducing pleasure through the alleviation of discomfort, further reinforcing reward-driven behaviors (*62*). This interplay of neural circuits highlights the complex mechanisms underlying hedonic feeding and its strong overlap with reward and addiction pathways.

Circadian Driven Feeding

Circadian rhythms are highly conserved ~24-hour autonomous oscillations that persist without environmental input, but can entrain (synchronize) to external cues (*63*). These rhythms induce timed molecular, physiological, and behavioral patterns in organisms throughout dark and light cycles (*64*). Anticipation of external cues can optimize daily cycles including metabolic processes (*65*). Conserved cellular mechanisms, coined the transcription-translation feedback loop (TTFL), produce daily oscillations in nearly all tissue types (*66*). The core TTFL initiates when the transcription factors Circadian Locomotor Output Cycles Kaput (CLOCK) and Brain

and Muscle ARNT-Like protein (BMAL1) bind and form a heterodimer, inducing the transcription of E-box enhancer-containing genes (*67*, *68*). Transcription of circadian clock genes *Period* (*Per 1-3*) and *Cryptochrome* (*Cry 1-2*) results in CLOCK:BMAL1 repression and degradation (*69*). Kinases then phosphorylate PER and CRY, leading to their ubiquitination and subsequent targeted degradation to restart the rhythmic signaling cascade. This molecular clock cycles with a period of about 24 hours and persists autonomously in most cells (*70*).

Circadian rhythms are strongly regulated by light-mediated processes to synchronize whole body oscillations. The suprachiasmatic nucleus (SCN) in the hypothalamus is the principal pacemaker and functions as the light entrainable oscillator, to optimize daily physiological and metabolic outputs (*71*). While light is a strong entrainment signal, food cues are also capable of entraining peripheral body clocks independent of light input to the SCN (*72*). The food entrainable oscillator (FEO) mediates physiological, behavioral, and environmental synchrony, optimizing metabolic processes in anticipation of a meal (*73*–*75*). Though the presence of the food entrainable oscillator has been known for over a century, its precise anatomical location and molecular architecture is unknown (*76*).

The debate over the principal regulator of food entrainment has highlighted various central and peripheral regions that may contribute to this circadian-regulated process. Among the key peripheral tissues involved are the liver, gastrointestinal tract, pancreas, and adipose tissue, all of which relay energy state cues to the body and brain (*77*–*79*) . The liver clock, as measured by Per2 expression (*80*, *81*), adjusts to meal timing when food intake is restricted to a specific window. Research suggests that hepatokines and ketone bodies secreted by the liver play a crucial role in food anticipation and entrainment (*82*, *83*). Adipose and gastrointestinal hormones are also tightly linked to feeding, hunger, and metabolic regulation. These metabolic cues help coordinate physiological processes that prepare the body for feeding and digestion (*84*). For

example, when mealtimes are consistent over time, GLP-1 is secreted approximately one hour before a meal, triggering a cephalic phase insulin spike about 30 minutes before feeding (*85*, *86*). This illustrates how peripheral hormone secretion primes multiple organ systems, optimizing metabolic efficiency while maintaining a memory of regular mealtimes (*87*, *88*).

Evidence suggests that several central brain regions may contribute to the food-entrainable oscillation, including the dorsomedial hypothalamus (DMH), arcuate hypothalamus (Arc), nucleus of the solitary tract (NTS), parabrachial nucleus (PBN), and prefrontal cortex (PFC), among others (*89*, *90*). Studies have shown that specific neuronal populations within the DMH, particularly those expressing leptin receptors (Lepr) and prodynorphin (Pdyn) (*91*, *92*), play a critical role in FEO expression (*93*, *94*), However, some researchers argue that the DMH is not essential for FEO function (*95*–*97*). Neuron activation studies in time-restricted fed mice have found sustained activation in regions such as the Arc, DMH, PBN, and NTS, even after the feeding schedule ended (*89*). This persistent activity suggests that these regions may encode memory-like or clock-like properties. The PFC is implicated in planning and decision-making (*98*), including behaviors associated with food anticipation, such as running before a scheduled meal or conserving energy (*99*). It also integrates signals from other brain regions, including dopamine pathways, to regulate adaptive behaviors (*100*). Although the precise location of the FEO remains unclear, current research suggests that it functions as a distributed network across multiple brain regions and tissue types (*101*), rather than being a single, centralized light entrainable oscillator like the SCN.

C1.2 Central and Peripheral Dysregulation in Obesity

Both brain-derived and peripheral metabolic signals are tightly regulated by a network of checks and balances that maintain energy homeostasis. However, excess adipose tissue can disrupt these systems, leading to overweight and obesity (*102*). The development of obesity results

from a complex interplay of genetic predisposition, environmental factors, physical activity levels, and socioeconomic conditions (*103*). Chronic low-grade inflammation is a hallmark of obesity, contributing to widespread dysregulation across multiple organ systems. This inflammatory state is linked to an increased risk of metabolic disorders such as type II diabetes and metabolic dysfunction-associated steatohepatitis (MASH), certain cancers, and neurodegenerative diseases like Alzheimer's (*104–108*).

Repetitive hedonic feeding behaviors, driven by the pursuit of highly palatable, calorie-dense foods rich in fats and carbohydrates, can lead to a chronic caloric surplus. The dopamine system reinforces these rewarding behaviors, and the mesolimbic dopamine pathway can override homeostatic signals that regulate energy balance (*109*, *110*). Similarly, shift workers who consume most of their calories during the night, when they should be inactive, face a significantly higher risk of developing obesity and related metabolic disorders (*111–113*). These examples illustrate how disruptions in hedonic and circadian systems can impair energy homeostasis, leading to feedback system failures that contribute to the persistence of obesity.

Beyond inflammation, obesity is marked by chronic hyperglycemia, hyperinsulinemia, and hyperleptinemia (*114–117*). Leptin and insulin are key signals for satiety and meal termination and remain persistently elevated in obesity, indicating that their production is intact but their target cells fail to respond appropriately. This resistance impairs glucose uptake, leading to sustained high blood sugar levels. Insulin and leptin resistance are active areas of research, as scientists seek to understand how cells lose sensitivity to these crucial signaling hormones in disease states (*118*). Additionally, obesity is associated with elevated triglycerides and low-density lipoprotein (LDL), commonly referred to as "bad cholesterol" (*119*, *120*). These metabolic disturbances significantly increase the risk of cardiac, renal, and hepatic diseases, ultimately raising the likelihood of heart, kidney, and liver failure.

Centrally, leptin receptors in the hypothalamus and hindbrain become resistant in obesity, as do receptors for other peripheral hormones like insulin(*121*, *122*). Additionally, overactivation of the hypothalamic-pituitary-adrenal (HPA) axis elevates cortisol levels (*123*), contributing to high blood pressure and further metabolic dysregulation (*124*). Serotonin signaling within homeostatic circuits is also affected, with reduced activity potentially contributing to obesity. Studies show that suppressing central serotonin signaling can lead to hyperphagia and weight gain (*39*). Meanwhile, the mesolimbic dopamine system can become dysregulated, diminishing sensitivity to normal rewards and driving overconsumption of highly palatable foods to achieve pleasure (*125*). Limbic structures, such as the amygdala, may also become dysregulated, reinforcing emotional or binge-like eating behaviors (*126*). The hippocampus, which plays a key role in storing feeding-related memories, can be impaired in its ability to recall meal frequency and portion sizes, further disrupting energy balance (*127*). While this list is not exhaustive, the full extent of how these dysregulated circuits interact as a network to promote overconsumption and obesity remains an active area of research.

It is clear there is no one target, from the cellular to organ level that directly causes obesity, but a cascade of signals and circuit changes over time that contributes to the disease. Due to this, the pursuit to uncover efficacious and safe obesity treatments has been a century-long challenge, one which we are only now starting to find some successful interventions.

C1.3 History of Obesity Treatments

Therapies for Polygenic Obesity

Polygenic obesity is the most common form of the disease, arising from a complex interplay of genetic, environmental, socioeconomic, dietary, and activity-related factors (*128*). Because no single gene or target is responsible, the search for effective weight-loss treatments has been

ongoing for over a century. While diet and exercise remain the primary lifestyle recommendations for weight management, numerous factors such as metabolic adaptation, psychological health, and genetic predisposition can make sustained weight loss challenging and in many cases, beyond an individual's control (*129*). Traditional dieting often leads to cycles of weight loss and regain, known as "yo-yo dieting," which can leave individuals feeling frustrated and discouraged about the effectiveness of lifestyle interventions (*130*).

Reports dating back to the early 1900s indicate that thyroid extracts were used to enhance energy expenditure and promote fat loss (*131*, *132*). However, their severe cardiovascular side effects ultimately limited widespread use. Another early weight loss treatment discovered by Maurice Tainter at Stanford in the 1930s (*133*) was 2,4-Dinitrophenol (DNP). DNP is an uncoupler of oxidative phosphorylation and works to increase metabolic rate, leading to more fat burn (*134*). Interestingly, DNP was used in World War I as an important agent in manufacturing explosives, and even general overexposure to soldiers was reported to cause deaths (*135*). By 1938, DNP was declared unfit for human consumption by the Federal Food, Drug and Cosmetic Act following serious adverse side effects such as overheating, fever, and death (*136*).

By the 1940s, sympathomimetics such as amphetamines emerged as popular candidates for the treatment of obesity. In 1947, the Food and Drug Administration approved methamphetamine for weight loss purposes (*132*). Methamphetamine causes sharp increases in neurotransmitters such as dopamine, epinephrine, and serotonin (*137*). This drug also increases metabolic rate to burn fat while engaging hypothalamic circuits to inhibit feeding centers (*138*–*140*). However, due to its now well-documented addictive potential and profound neurotoxic effects, methamphetamine is no longer considered a viable obesity treatment (*141*, *142*). This led researchers to develop amphetamine congeners, structural variants designed to reduce addiction risk while maintaining weight-loss efficacy. These included phenmetrazine,

phendimetrazine, phentermine, and diethylpropion. While their likelihood of addiction and efficacy in weight loss are still not completely understood, these drugs were mainly approved for a short term use (*143*, *132*, *144*).

After recognizing the limitations of thyroid extracts and amphetamines as standalone weight-loss treatments, Clark & Clark introduced a combination drug therapy in 1941 called Clarkotabs, more famously known as "rainbow pills" (*132*). These pills were marketed as a personalized approach to weight loss, containing a mix of amphetamine sulfate, thyroid stimulants, phenobarbital, aloin, atropine sulfate, laxatives, diuretics, digitalis, and sedatives. The goal of this cocktail was to enhance weight loss and energy expenditure while mitigating side effects with additives like anti-anxiety benzodiazepines. Rainbow pills were heavily marketed to women, despite concerns over their safety. By 1968, the operation was largely shut down after being linked to 60 deaths (*145*).

Following the failures of methamphetamine and rainbow pills, amphetamines fell out of favor as weight-loss treatments. However, in 1973, serotonergic agents emerged as a new approach to obesity management (*146*, *147*). Over the next three decades, several drugs—including fenfluramine, phentermine-fenfluramine (phen-fen), dexfenfluramine, and sibutramine—were approved for obesity treatment (*148*–*151*). These agents worked by stimulating serotonin production and inhibiting serotonin and norepinephrine reuptake, mechanisms that engaged the melanocortin system to reduce food intake and promote weight loss (*152*, *153*). Beyond weight reduction, these drugs also improved key metabolic markers such as blood pressure, glycemia, and cholesterol levels, making them a seemingly promising non-addictive alternative for obesity treatment. However, by the late 1990s, all serotonergic weight-loss agents were pulled from the market after being linked to heart valve disease and pulmonary hypertension, ultimately halting their use in obesity management (*154*).

Nearly two decades after the withdrawal of earlier serotonergic weight-loss drugs, lorcaserin was approved as a new serotonin agonist for obesity treatment (*155*). Like its predecessors, lorcaserin was believed to work by activating satiety neurons in the hypothalamus and hindbrain, reducing food intake without significantly affecting energy expenditure (*156*). Beyond appetite suppression, lorcaserin also modulated dopamine responses, sparking interest in its potential as a treatment for substance abuse and binge eating disorders (*157*). It showed promise, particularly when combined with other type II diabetes and weight-reducing medications. Despite its initial success, lorcaserin was discontinued in 2020 after studies linked it to increased cancer risk and negative mental health outcomes, ultimately ending its use in obesity management (*158*).

After a century of failed monoamine-based therapies for obesity, new strategies targeting different mechanisms emerged. One approach was phentermine-topiramate, which combines a norepinephrine stimulant (phentermine) with an anticonvulsant (topiramate) to enhance satiety and promote weight loss (*159*). Orlistat, another breakthrough, works by inhibiting gastrointestinal lipase activity, reducing fat absorption in the gut and limiting overall fat retention (*160*). Rimonabant, an inverse agonist of the type I cannabinoid receptor (CB1R), was introduced as a weight-loss drug that also improved metabolic and cardiovascular health (*161*, *162*). However, it was quickly withdrawn from the market due to reports of serious psychiatric side effects, including depression and suicidal thoughts (*163*). Another combination therapy, naltrexone-bupropion, pairs an opioid receptor antagonist (naltrexone) with a dopamine reuptake inhibitor (bupropion) (*164*, *165*). This treatment suppresses cravings and appetite by modulating reward pathways and hypothalamic circuits, offering a different approach to obesity management (*166*).

Amid the rise and fall of numerous weight-loss drugs, a major breakthrough emerged in 1986 when researchers Habener, Mojsov, and others identified a cleavage product of glucagon known as glucagon-like peptide-1 (GLP-1) (*167*–*169*). Found in the gut, GLP-1 was soon recognized for its potent glycemic control and appetite-suppressing (anorectic) effects. Around the same time, John Eng was studying Gila monster venom and discovered a strikingly similar GLP-1 analog, later named exendin-4 (*170*, *171*). Unlike human GLP-1, which has a half-life of just ~1 minute, exendin-4 remained active for ~2 hours, making it a promising therapeutic candidate (*172*). This discovery led to the development of exenatide, the first GLP-1 receptor agonist (GLP-1RA), which was approved in 2005 to treat type II diabetes (*173*). A common side effect of exenatide was weight loss, laying the foundation for the modern era of GLP-1RAs (*174*), which are now among the most studied and widely used treatments for obesity and metabolic disorders.

Building on the success of synthetic GLP-1 analogs with improved half-lives, Novo Nordisk introduced liraglutide, a once-daily GLP-1 receptor agonist, in 2010 for type II diabetes (*175*), with approval for obesity following in 2014 (*176*, *177*). Structurally, liraglutide closely resembled endogenous GLP-1, with a single amino acid substitution and a 16-chain fatty acid attachment to extend its half-life (*178*). Liraglutide paved the way for semaglutide, a once-weekly injection with an even longer half-life, approved for type II diabetes in 2017 and obesity in 2021 (*179*, *180*). Novo Nordisk, alongside Eli Lilly, now dominate the obesity treatment market. Eli Lilly's tirzepatide, a dual GLP-1 and glucose-dependent insulinotropic polypeptide (GIP) agonist, received FDA approval for obesity in 2023 (*181*–*183*). Both semaglutide (Wegovy) and tirzepatide (Zepbound) have revolutionized obesity treatment, achieving ~20% body weight reduction (*184*), offering new hope for those struggling with obesity and metabolic disorders.

For the first time in over 50 years, obesity rates in the United States have begun to decline, a trend directly linked to the widespread adoption of glucagon-like peptide-1 receptor agonists (GLP1RAs) (*185*). Over the past five years, the use of GLP-1RAs has surged by 700% (*186*), with approximately 12% of the U.S. population having used these medications (*187*). This number is expected to continue rising as researchers develop new formulations, alternative delivery methods, and next-generation drugs that provide even greater efficacy with fewer side effects (*188*).

Therapies for Monogenic Obesity

Although monogenic obesity accounts for less than 5% of obesity cases, treatment strategies vary significantly depending on the specific genetic mutations (*189*, *190*). Monogenic obesity, which results from a single genetic mutation or deficiency, typically manifests as severe obesity from a young age accompanied by voracious hunger. For example, a leptin gene deficiency can be treated with metreleptin (*191*), a replacement therapy approved in 2014. In contrast, mutations in the leptin receptor gene lead to a similar obesity phenotype but currently lack any available treatments (*192*).

Mutations in the proopiomelanocortin (POMC) or melanocortin-4 receptor (MC4R) genes, which disrupt hypothalamic hunger circuits, also cause early-onset obesity (*193*–*195*). However, these mutations can be treated with setmelanotide, a MC4R agonist approved in 2020 (*196*). While progress has been made in treating certain forms of monogenic obesity, other genetic deficiencies, such as those involving the TUB, SIM1, BDNF, and PCSK1 genes, as well as syndromes like Prader-Willi, Alström, and Bardet-Biedl, still lack targeted therapeutic interventions (*197*–*199*). Much work remains to be done in the genetic realm to develop effective treatments for these rare, monogenic obesity disorders.

Alternate Interventions for Obesity

By the 1980s, obesity rates began to reach epidemic levels, as reported (*200*). As global body weights increased, treatment options remained limited or were frequently withdrawn after a few years due to safety or efficacy concerns. This period also coincided with the introduction of high fructose corn syrup, ultra-processed foods, and the rise of fast food chains, contributing to dietary shifts (*5*, *201–204*). Traditional treatments, such as diet and exercise, often failed due to issues with adherence and the lack of personalized plans for lifestyle changes.

Faced with few options, doctors and researchers began to explore surgical interventions. The first significant weight loss observation came in 1966, when a patient who underwent a gastrectomy for cancer showed marked weight loss, coining the term bariatric surgery (*205*, *206*). By 1994, laparoscopic gastric bypass surgery became safer and more feasible, expanding access to obesity treatment. Today, there are several types of bariatric surgery, including Roux-en-Y gastric bypass, sleeve gastrectomy, lap band, intragastric balloon, and biliopancreatic diversion with duodenal switch (*207*, *208*). These procedures vary slightly but all work by either shrinking or bypassing the stomach and/or the small intestine. These surgical options are highly effective, with patients typically losing over 50% of their body weight in the first year, and many are able to maintain long-term weight loss when combined with lifestyle interventions (*205*).

Surgical interventions for obesity can be life-changing and highly successful for some patients. However, there are significant barriers to accessing these treatments as Body Mass Index (BMI) of at least 40 is often required before surgery is even considered. The cost of bariatric surgery often exceeds $15,000, and insurance coverage is not always guaranteed making it inaccessible for many individuals (*209*). Additionally, long-term success can be compromised if stomach pouches stretch over time, potentially increasing food intake and contributing to weight

regain. Other complications include surgical risks, the development of ulcers, nutrient malabsorption, and dumping syndrome, which causes extreme gastrointestinal discomfort after consuming highly palatable foods (*210*, *211*). While surgery can be a powerful tool for weight loss, these barriers and risks should be carefully considered before opting for this treatment.

Seeking minimally invasive alternatives in the 1980s, doctors tested jaw wiring for severely obese patients (*212*). This procedure involved tying the jaw shut, making chewing and eating extremely difficult. While there are few studies, they boast that this treatment was as effective as bariatric surgery in reducing body weight, but “ineffective if applied to patients with poor motivation and immature personalities” (*213*, *214*). However, once the wires were removed, many patients regained the weight they had lost. Due to its logistical challenges and likely ethical concerns, jaw wiring was never widely accepted as a mainstream obesity treatment.

Beyond invasive options, lifestyle interventions are critical in addressing and curbing the obesity epidemic. For decades, maintaining a healthy diet and engaging in regular exercise have been the cornerstone to weight management. These approaches can be effective, but the science behind what constitutes a healthy diet for each individual, as well as the optimal amount and type of exercise, are still not fully understood. Dieting can be particularly discouraging because many people experience weight regain after initial loss, a phenomenon often referred to as the setpoint theory (*215*). This theory suggests that the body has a preferred weight range, and when individuals lose weight, metabolic rate decreases, and hunger levels rise, prompting the body to return to its prior weight. This complex feedback loop can make long-term weight loss challenging, even with consistent effort.

In addition to lifestyle changes, cognitive behavioral therapy (CBT) can be an effective option for addressing underlying emotional factors contributing to obesity, such as binge eating or

depression-associated obesity (*216*). CBT can help individuals develop healthier relationships with food and manage emotional eating patterns. Health and nutrition programs like Weight Watchers and Noom also provide structure to food choices and body weight management, offering a framework for sustainable weight loss (*217*). Trends such as intermittent fasting, the ketogenic diet, vegetarian and vegan diets, the carnivore diet, the Mediterranean diet, and the gluten-free diet have gained mainstream attention (*218*, *219*). While these diets are often touted for their benefits, they often lack strong scientific backing to support their long-term effectiveness. Although balanced nutrition and regular exercise are vital components of a healthy mental and physical lifestyle, many people find that these interventions alone are insufficient for sustained weight loss. As a result, the demand for effective, personalized treatments continues to grow.

Chapter 2. Leptin receptor neurons in the dorsomedial hypothalamus input to the circadian feeding network

Authors

Qijun Tang[1†], Elizabeth Godschall[1†], Charles D. Brennan[1], Qi Zhang[1], Ruei-Jen Abraham-Fan[1], Sydney P. Williams[1], Taha Buğra Güngül[1], Roberta Onoharigho[1], Aleyna Buyukaksakal[1], Ricardo Salinas[1], Isabelle R. Sajonia[1], Joey J. Olivieri[1], O. Yipkin Calhan[1], Christopher D. Deppmann[1-5], John N. Campbell[1,5*], Brandon Podyma[1,6†*], Ali D. Güler[1,2,5*]

1. Department of Biology, University of Virginia, Charlottesville, VA 22904, USA

2. Program in Fundamental Neuroscience, Charlottesville, VA 22904, USA

3. Department of Cell Biology, University of Virginia, Charlottesville, VA, 22904, USA

4. Department Biomedical Engineering, University of Virginia, Charlottesville, VA, 22904, USA

5. Department of Neuroscience, School of Medicine, University of Virginia, Charlottesville, VA 22903, USA

6. Medical Scientist Training Program, School of Medicine, University of Virginia, Charlottesville, VA 22903, USA

*Corresponding author. Email: aguler@virginia.edu, podyma@virginia.edu, jnc4e@virginia.edu.

†These authors contributed equally to this work.

This chapter was published in August 2023 in *Science Advances*. PMID: 37624889, PMCID: PMC10456850, DOI: 10.1126/sciadv.adh9570. This work was in close collaboration with Qijun Tang and Brandon Podyma. My major contributions have been extracted from the publication and each author's contributions are highlighted in the figure legends.

C2.1 Abstract

Salient cues, such as the rising sun or the availability of food, play a crucial role in entraining biological clocks, allowing for effective behavioral adaptation and ultimately, survival. While the light-dependent entrainment of the central circadian pacemaker (suprachiasmatic nucleus, SCN) is relatively well characterized, the molecular and neural mechanisms underlying entrainment associated with food availability remain elusive. Using single nucleus RNA sequencing during scheduled feeding (SF), we identified a leptin receptor (LepR) expressing neuron population in the dorsomedial hypothalamus (DMH) that upregulates circadian entrainment genes and exhibits rhythmic calcium activity prior to an anticipated meal. We found that disrupting DMH^{LepR} neuron activity had a profound impact on both molecular and behavioral food entrainment. Specifically, silencing DMH^{LepR} neurons, exogenous leptin administration, or chemogenetic stimulation of these neurons all interfered with the development of food entrainment. In a state of energy abundance, repetitive activation of DMH^{LepR} neurons led to the partitioning of a secondary bout of circadian locomotor activity that was in phase with the stimulation and dependent on an intact SCN. Lastly, we discovered that a subpopulation of DMH^{LepR} neurons project to the SCN with the capacity to influence the phase of the circadian clock. This direct DMH^{LepR}-SCN connection is well situated as a point of integration between the metabolic and circadian systems, facilitating the anticipation of meal times.

C2.2 Main

When we eat is as important for our health as what and how much we eat. Studies in both mice and humans have shown that eating during the rest phase (daytime for mice or nighttime for humans) is associated with increased risk of weight gain, glucose intolerance, hepatic steatosis, and cardiovascular disease (*220–223*). Efforts to mitigate these deleterious effects in mice by restricting when they eat have provided significant promise to improve metabolic health and

even extend lifespan. The potential benefits of time-restricted eating to human cardiometabolic health is the focus of many ongoing clinical studies (*224*–*228*). However, we have a limited mechanistic understanding of how meal timing influences our physiology and biological rhythms (*229*). Therefore, we sought to better understand the anatomical and molecular underpinnings of the interaction between feeding time and the circadian clock using a model of scheduled feeding (SF) that rapidly induces biological entrainment in rodents (*230*–*232*).

The suprachiasmatic nucleus (SCN) in the hypothalamus is the primary pacemaker that receives ambient light information from the retina, synchronizes circadian machinery throughout the body, and coordinates behavioral outputs (*70*, *233*). Interestingly and less well understood, in the absence of a functional SCN (*231*, *232*), the circadian system retains the ability to entrain to the timing of non-photic environmental cues, such as food (*230*). Numerous efforts have failed to identify any necessary genetic, molecular, or anatomic substrates of food entrainment (*76*, *234*). Emerging evidence suggests that the food entrainment system encompasses multiple food entrainable oscillators distributed across the central nervous system and peripheral organs, in which partial malfunction is compensated by other parts of the network (Fig. 1A) (*72*, *74*, *82*, *229*, *234*, *235*).

Here we used a time and calorie restricted feeding paradigm to rapidly induce food entrainment in mice (*236*), with a focus on the SCN and the dorsomedial hypothalamus (DMH) which are involved in the regulation of feeding, locomotor activity, sleep-wake cycles, and hormone rhythms (*237*–*240*). By using single nucleus RNA sequencing, we sought to identify neuronal populations in the SCN and DMH that show changes in circadian transcriptional programs. We did not observe appreciable transcriptional changes of genes associated with circadian rhythmicity or circadian entrainment pathways in the SCN during scheduled feeding (SF). However, we identified several neuronal populations in the DMH that altered their expression of

circadian entrainment genes in response to timed feeding, including the leptin-receptor (LepR) expressing neurons. Next, we demonstrated that chronic silencing or over-activation of the DMH^{LepR} neurons, as well as leptin administration, impairs development of food entrainment. Finally, we uncovered a direct neuronal projection from DMH^{LepR} neurons to the SCN and showed that DMH^{LepR} neuron stimulation is sufficient to phase shift the SCN circadian clock while altering the structure of circadian locomotor activity. These results define a mechanism that integrates mealtime information with the circadian clock via leptin signaling in the DMH.

C2.2.1 Scheduled feeding alters circadian entrainment gene expression in the DMH but not the SCN

In mammals, the SCN in the hypothalamus is the seat of the primary circadian clock which receives ambient light signals and synchronizes the biological clocks distributed throughout the body (*233*). Although it is not required for the expression of food anticipatory behavior (FAA) (*232*, *241*, *242*), the SCN has recently been shown to modify the robustness of food entrainment (measured by one of the behavioral outputs of food entrainment, FAA) (*243*) (Fig. 1A). We tested the entrainment of central and peripheral circadian systems using a scheduled feeding (SF) paradigm where we restricted both time and calories of the food delivered. In contrast to only time-restricted feeding regimens, which shift peripheral but not central circadian clocks (*77*), this SF paradigm induces a phase advance in the bioluminescent reported circadian rhythmicity of both the SCN and the liver from PER2::Luciferase (PER2LUC) transgenic mice (Fig. 1B) (*81*). Our observation is in line with previously demonstrated SCN rhythm phase shifts in time- and calorie-restricted animals (*244*, *245*). To further elucidate the transcriptional programs of hypothalamic regions in food entrainment, we harvested fresh brain tissues at 5 hours after lights on (*Zeitgeber* time or ZT 5) from mice that were subjected to three feeding conditions: *ad libitum*, overnight fasted, or fed at ZT 6 for ten days (SF; Fig. 1C-D). We isolated

SCN, as well as DMH, a hypothalamic region previously implicated in circadian and feeding regulation (Fig. 1E) (*237*, *246*). After brain region- and feeding condition-specific tissue collection and nuclei isolation, we performed single-nucleus RNA sequencing (snRNAseq), yielding raw datasets of 59,708 and 65,837 cells from SCN- and DMH-containing tissues, respectively.

Using previously defined SCN markers (e.g., *Avp, Vip, Vipr2, Prok2, Per2)* (*247*, *248*), we identified 8,957 cells as SCN neurons and clustered them by transcriptomic similarity into 8 candidate subtypes (Fig. 1F-I, Supplemental Fig. 1A-D). In the final SCN dataset, the mean number of genes and unique transcripts (unique molecular identifiers, UMIs) detected per cell in all SCN samples was 1,783 and 3,294, respectively (Supplemental Fig. 1C). We then compared SCN neuron gene expression across feeding conditions: SF versus *ad libitum*, SF versus fasting, and fasting versus *ad libitum* conditions. Using the Kyoto Encyclopedia of Genes and Genomes (KEGG) Mouse 2019 database, we performed gene enrichment analysis and identified the top five up- and down-regulated pathways in the SCN (Fig. 1J). Neither circadian entrainment nor circadian rhythm pathways were significantly altered in the SCN under SF relative to the other feeding conditions. Despite the primacy of the SCN in photically regulated pacemaking and the shift observed in *Per2* rhythmicity (Fig. 1B), these snRNAseq data show that transcriptional alteration of the circadian system is limited in the SCN in response to food based pacemaking, in line with previous work showing its expendability for food entrainment (*231*, *232*, *241*).

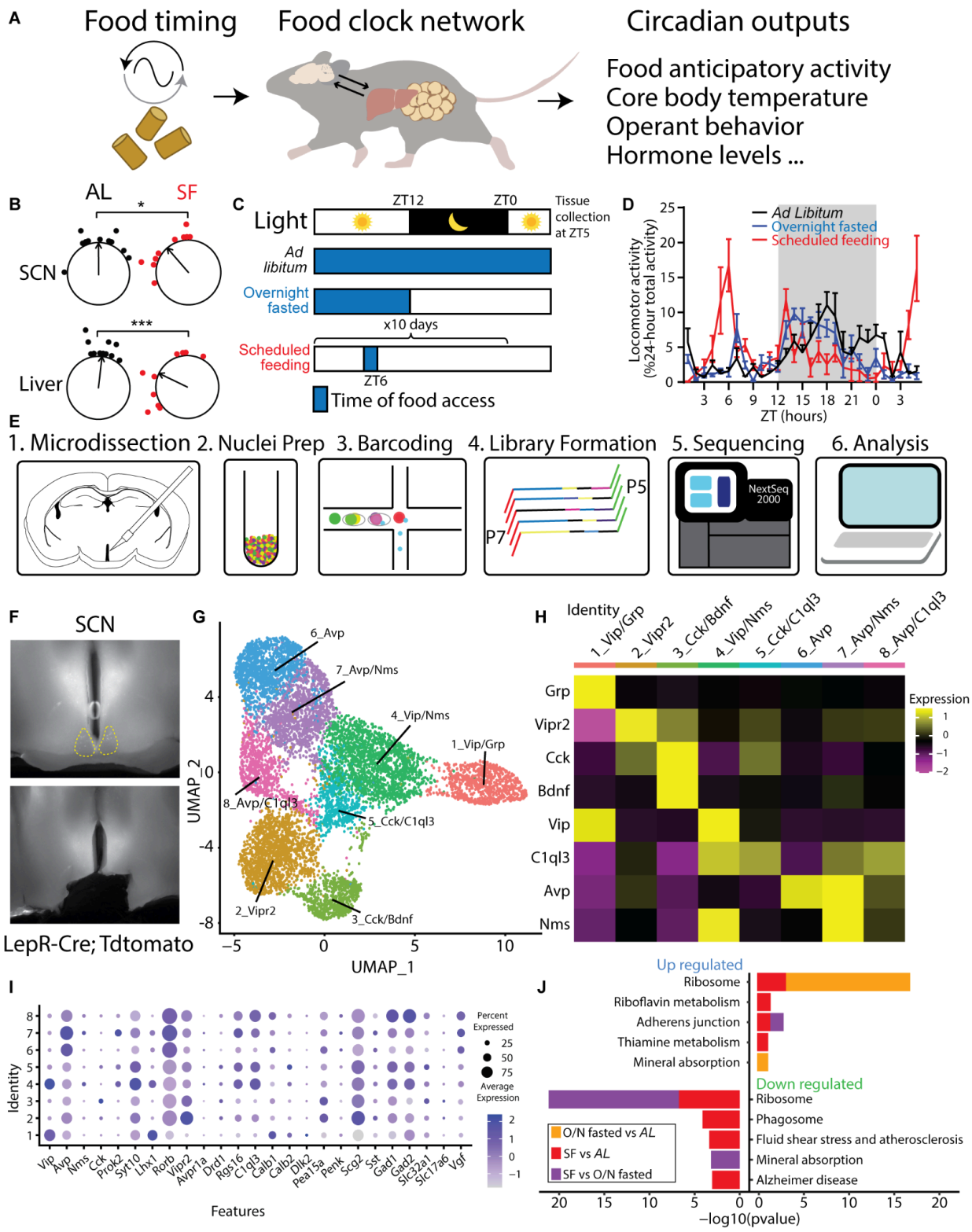

Figure 1. SCN snRNAseq reveals minimal alteration of circadian genes during SF A. (Qijun Tang) Diagram illustrating that food timing as a potent zeitgeber entraining an oscillatory network system in the brain and peripheral organs, relaying rhythmic behavior outputs. **B.**

(Elizabeth Godschall, Qijun Tang) The ZT phase of the first bioluminescence peak of SCN and liver from PER2::Luciferase mice that are either provided with scheduled food access for 4 days at ZT6 or *ad libitum* fed controls (untreated or given ZT6 saline injections). Phases of sample points are shown relative to the normalized mean phase of control SCN. Two-way ANOVA with Bonferroni post hoc comparison; n = 10-11 / group; $F_{treatment}$ (1, 38) = 19.05, p<0.001. **C. (Qijun Tang)** Schematic of experimental design. Mice were housed on a 12-12 light-dark cycle and either fed *ad libitum,* overnight fasted, or provided a scheduled meal for 10 days at ZT6. Blue shading denotes food access. All mice were sacrificed for tissue collection at ZT5. **D. (Elizabeth Godschall, Qijun Tang)** Normalized locomotor activity starting 29 hours before tissue collection. n=4 mice / condition. Data are represented as mean ± SEM. **E. (Elizabeth Godschall, Qijun Tang, Ruei-Jen Abraham-Fan, John Campbell)** Schematic of single nuclei RNA sequencing (snRNAseq) workflow using 10X Genomics. **F. (Elizabeth Godschall)** Representative images illustrating the area of dissection in the SCN for snRNAseq. **G. (Elizabeth Godschall)** Uniform Manifold Approximation and Projection (UMAP) plot of 8 molecularly distinct SCN neuron subtypes (n=8,957 neurons) **H. (Elizabeth Godschall)** Heatmap of cluster-average marker gene expression, scaled by gene. **I. (Elizabeth Godschall)** Dot plot of average expression level (dot color) and percent expression (dot size) for each SCN neuron cluster. Genes shown are previously defined as SCN markers (*247*, *248*) and validated based on Allen Brain Atlas Mouse Brain *in situ* hybridization data (*249*). **J. (Elizabeth Godschall)** Gene enrichment analysis comparing top 5 pathways up- and down-regulated among feeding conditions in all SCN neurons, using Kyoto Encyclopedia of Genes and Genomes (KEGG) Mouse 2019 database. Inclusion criteria required p-value <0.05 and log2 fold change >0.25.

We next turned our attention to the DMH, a neighboring hypothalamic region which has been strongly implicated in circadian behaviors and physiological processes (*237–240*). However, the extent of DMH involvement in food entrainment is controversial with substantial reproducibility concerns (*75*, *92–94*, *234*, *235*, *240*, *250–258*), potentially due to the heterogeneity of DMH neurons. Therefore, we used snRNAseq to compare the gene expression profiles of 16,281 DMH neurons from mice under *ad libitum*, fasted, or scheduled feeding conditions. We first identified DMH neurons from our snRNA-seq dataset based on their enriched expression of known DMH markers including *Gpr50, Grp, Rorb, Sulf1, Pcsk5, Lepr, Pdyn,* and *Ppp1r17* (*254*, *259*, *260*). We then clustered these putative DMH neurons into 14 candidate subtypes according to transcriptomic similarity and annotated them based on top marker genes (Fig. 2A-D,

Supplemental Fig. 1E-H). The mean number of genes and UMIs per cell detected in all DMH samples was 2,425 and 5,235, respectively (Supplemental Fig. 1G).

Our dataset contained clusters corresponding to previously identified DMH neuron populations, those expressing *Lepr*, *Pdyn*, or *Ppp1r17(92, 253, 254, 260)*, along with cluster-specific expression of 2_Tcf7l2 *(261)* or 12_Nfix that together previously were named *Lhx6*+ neurons (*262*). In sharp contrast to the SCN, DMH gene enrichment analysis revealed upregulation of the circadian entrainment genes (e.g. *Kcnj6, Ryr2, Nos1*, etc.), which are involved in transmitting salient extracellular signaling cues to the core molecular clock (*263*–*265*) (https://www.kegg.jp/entry/map04713; Supplemental Fig. 1I, 2). This upregulation was seen not only in SF vs *ad libitum*, but also SF vs fasted conditions, demonstrating that the effect on expression of circadian entrainment genes was not simply due to energy deficit, but adaptation to food timing (Fig. 2E). These results imply that the genes capable of influencing the DMH circadian clock are altered by scheduled feeding.

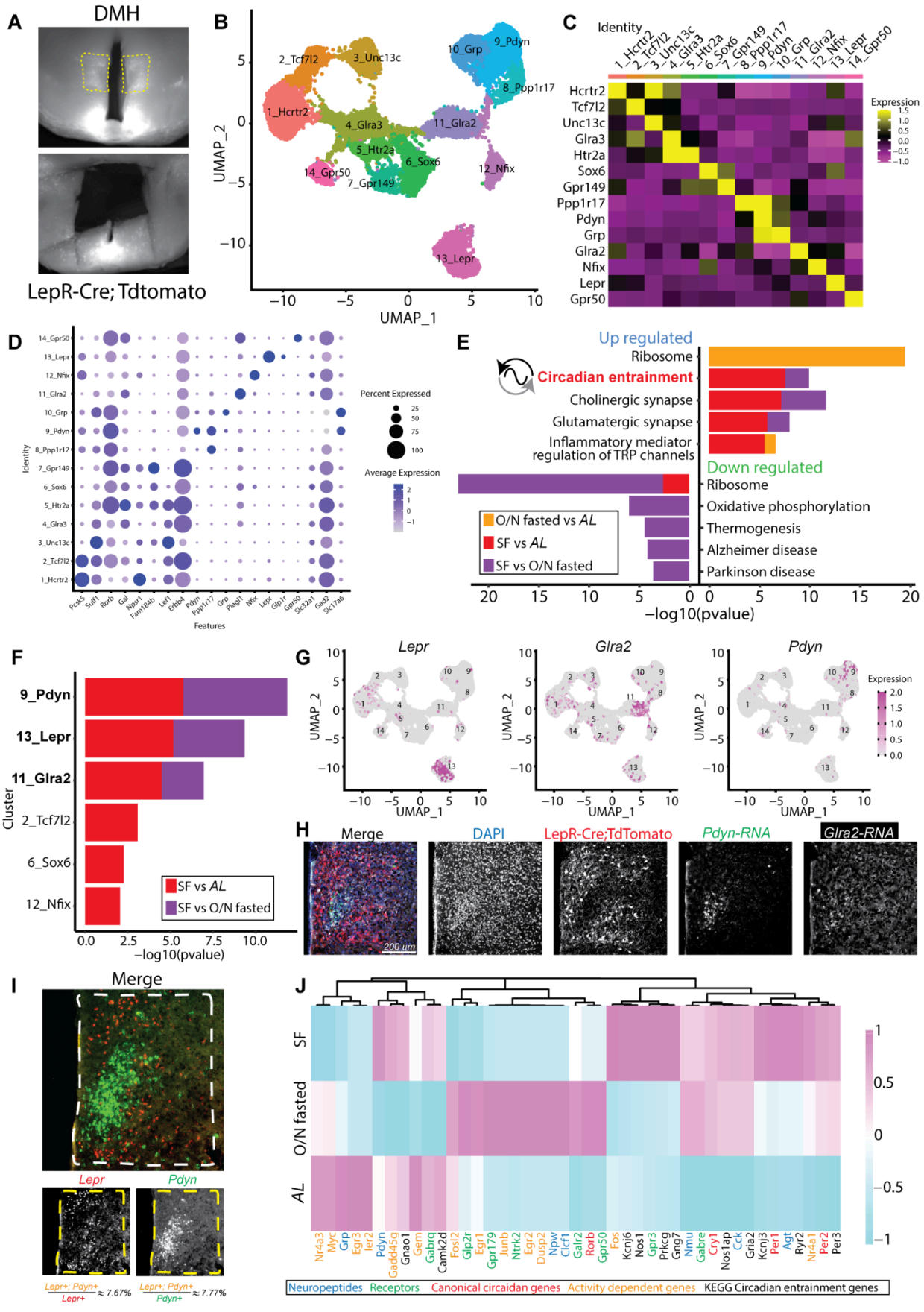
A
DMH
LepR-Cre; Tdtomato
B
UMAP_1
UMAP_2
1_Hcrtr2
2_Tcf7l2
3_Unc13c
4_Glra3
5_Htr2a
6_Sox6
7_Gpr149
8_Ppp1r17
9_Pdyn
10_Grp
11_Glra2
12_Nfix
13_Lepr
14_Gpr50
C
Identity
Expression
D
Percent Expressed
Average Expression
Features
E
Up regulated
Ribosome
Circadian entrainment
Cholinergic synapse
Glutamatergic synapse
Inflammatory mediator regulation of TRP channels
Down regulated
Ribosome
Oxidative phosphorylation
Thermogenesis
Alzheimer disease
Parkinson disease
O/N fasted vs AL
SF vs AL
SF vs O/N fasted
−log10(pvalue)
F
Cluster
SF vs AL
SF vs O/N fasted
−log10(pvalue)
G
Lepr
Glra2
Pdyn
Expression
H
Merge
DAPI
LepR-Cre;TdTomato
Pdyn-RNA
Glra2-RNA
200 um
I
Merge
Lepr
Pdyn
J
SF
O/N fasted
AL
Neuropeptides
Receptors
Canonical circaidan genes
Activity dependent genes
KEGG Circadian entrainment genes

Figure 2. SF alters circadian entrainment genes in specific DMH neuron subtypes. A. (Elizabeth Godschall) Representative images illustrating the DMH area dissected for snRNAseq. **B. (Elizabeth Godschall)** UMAP of 14 defined DMH neuron subtypes (n=16,281 neurons). **C. (Elizabeth Godschall)** Average gene expression heatmap labeled by cluster-specific markers in the DMH. **D. (Elizabeth Godschall)** Dot plot of average expression level (dot color) and percent expression (dot size) of genes of interest within DMH clusters. These genes were either previously identified in DMH (*254*, *259*, *260*, *266*) or validated as DMH markers by the Allen Brain Atlas Mouse Brain *in situ* hybridization data (*249*). **E. (Elizabeth Godschall)** Gene enrichment analysis comparing top 5 pathways up- and down-regulated across feeding conditions in all DMH neurons, using KEGG Mouse 2019 database. Inclusion criteria required p-value <0.05 and log2 fold change >0.25. **F. (Elizabeth Godschall)** DMH clusters with differentially regulated circadian entrainment pathways in at least one scheduled feeding comparison. **G. (Elizabeth Godschall)** Feature plots indicating spatial expression of *Lepr* (left), *Glra2* (middle), *Pdyn* (right), in DMH clusters. **H. (Elizabeth Godschall, Qijun Tang)** Representative coronal section image localizing expression of LepR, *Pdyn*, and *Glra2* in the DMH. LepR cells were marked by LepR-Cre;TdTomato protein, whereas *Pdyn* and *Glra2* transcripts were visualized by RNA FISH. See also supplemental Fig. 4F for zoomed-out view of the same brain section. **I. (Elizabeth Godschall, Qijun Tang)** Representative RNA FISH coronal section image showing *Lepr* and *Pdyn* transcripts in the DMH. Quantification of *Lepr* and *Pdyn* co-expressing cells is depicted at the bottom. n=3 mice. **J. (Elizabeth Godschall)** Heatmap of select genes that were differentially expressed across feeding conditions in DMH^{LepR} neurons.

C2.2.2 SF alters circadian entrainment gene expression in DMH^{LepR} neurons

The DMH is a heterogeneous hypothalamic nucleus with multiple functions containing numerous genetically distinct cell populations, two of which (expressing either *Pdyn* or *Ppp1r17*) have been previously investigated in food entrainment behavior (*92*, *253*, *254*). Thus, we sought to understand which DMH neuronal subpopulations exhibit the most significant change in circadian entrainment gene expression during SF. Of the 14 neuron clusters we identified in the DMH, six showed differential gene expression in circadian entrainment pathway during energy deficit, and three of these had differential gene expression in both SF vs. *ad libitum* and SF vs. fasted conditions: cluster 9, Pdyn [prodynorphin] neurons; cluster 13, Lepr [leptin receptor] neurons; and cluster 11, Glra2 [glycine receptor subunit alpha-2] neurons (Fig. 2F-H, Supplemental Fig. 3, 4).

Of these candidate DMH neuron subtypes, those expressing *Pdyn* and *Lepr* have putative connections with both circadian and feeding regulation (*238*, *253*), and exhibit strikingly different anatomic distributions within the DMH, while *Glra2* does not (Fig. 2H, Supplemental Fig. 4D-F)(*249*). For these reasons we chose to further investigate the *Pdyn*+ and *Lepr*+ neuron subtypes in our dataset. *Lepr*+ and *Pdyn*+ neurons partially overlap in the DMH (*260*). However, using RNA fluorescence *in situ* hybridization (RNA FISH), we found that this overlap is minimal: only ~7.67% of *Lepr*+ neurons are *Pdyn*+, while ~7.77% of *Pdyn*+ neurons are *Lepr*+ (Fig. 2I). Additionally, we observed that the *Lepr* expression is predominant in the dorsal and ventral DMH, whereas *Pdyn* expression is confined to the compact central DMH (Fig. 2I). The DMH^{Pdyn} neurons have been shown to entrain to scheduled feeding(*253*) and dampen the robustness of FAA when silenced (*92*). However, the contribution of DMH^{LepR} neurons to food entrainment is unknown despite their important role in feeding and energy homeostasis (*238*, *260*, *267*, *268*). Therefore, we chose to focus our attention on DMH^{LepR} neurons. Detailed analysis of the DMH cluster 13 Lepr neurons in our dataset revealed that SF alters transcription of circadian entrainment pathway genes (Supplemental Fig. 1I, 4C), as well as activity dependent genes, neuropeptides, receptors, and canonical circadian clock genes. Together, these transcriptional responses to scheduled feeding point to a significant role for DMH^{LepR} neurons in food entrainment (*92*, *253*) (Fig. 2J, Supplemental Fig. 4C).

C2.3 Discussion

The circadian system synchronizes to salient non-photic cues, such as timed availability of food, receptive mates, or exercise (*230*, *269*, *270*). In this work, we demonstrate that leptin, in combination with one of its central nervous system targets, the DMH^{LepR} neurons, forms an essential node that links food intake with the development of circadian food entrainment. In the process, we also identified an intriguing property of the circadian system whereby locomotor

activity is partitioned into at least two components in response to overactivation of the DMH^{LepR} neurons. By functional direct innervation to the SCN, DMH^{LepR} neurons have the potential to serve as an information conversion point for non-photic entrainment. The methodological paradigms presented here offer a new platform to test the involvement of other molecular signals and anatomic regions in the development and maintenance of food entrainment, and the relative function of inputs to the circadian system.

Impact of SF on canonical clock genes in the SCN and DMH

In our snRNAseq analysis of SCN and DMH, we did not observe a significant difference in the KEGG annotated circadian rhythm pathway (canonical circadian genes, e.g. *Bmal1*, *Clock*; https://www.kegg.jp/entry/map04710), except for *Per3* expression in the DMH (Supplemental Fig. 1I, 4C). However, we did observe a significant phase advance of PER2 bioluminescence in the SCN during SF (Fig. 1B). Therefore, we cannot rule out an alteration in the expression of other core circadian genes, since they are expressed at different phases, which might require snRNAseq analysis at multiple time points across the day to reveal a change. In contrast, we did identify genes in the circadian entrainment pathway to be altered in the DMH (Fig. 2, Supplemental Fig. 1I, 4C).

It has been increasingly acknowledged that when we eat, in addition to what and how much, plays a critical role in maintaining metabolic homeostasis and health (*223–225*, *227*, *271–273*). This bidirectional relationship between food and the circadian clock likely mediates dysfunction of both the circadian system and metabolic homeostasis in response to improperly timed feeding, e.g. nighttime snacking. Further understanding of the circuits that govern these food-circadian interactions will provide new avenues to improve metabolic health (*228*, *274–276*).

C2.4 Acknowledgements

We thank the members of the Güler, Deppmann, Campbell, and Provencio labs (University of Virginia), Yamazaki lab (University of Texas Southwestern Medical Center) and Steele lab (California State Polytechnic University, Pomona) for comments and suggestions on the preparation of the manuscript. We are thankful for technical advice from Austin Byler Keeler, Jianhua Cang and Chad Daniel Meliza (electrolytic lesion, University of Virginia), and Pantong Yao (*in vivo* calcium imaging data interpretation, University of California San Diego). Additionally, we are grateful for the access to the confocal microscope generously provided by Cang and Liu labs (University of Virginia). We are grateful for the statistical analysis consulting service provided by Jacob Goldstein-Greenwood (University of Virginia Library Research Data Services/StatLab). We are grateful for the generous gift of the cre dependent TeTx virus from Zweifel lab (Washington University). We thank the University of Virginia School of Medicine Genome Analysis and Technology Core, RRID:SCR_018883 for sequencing our samples and quality control. This work was supported by NIH T32-GM7267-39 and NIH T32-GM7055-45 (B.P.), NIH R01GM121937 and R35GM140854 (A.D.G.), NIH R01HL153916-01A1 and American Diabetes Association Pathway to Stop Diabetes award 1-18-INI-14 (J.N.C.), and a UVA Wagner Fellowship (B.P.).

C2.5 Author Contributions

Q.T., E.G., C.D.D, B.P., J.N.C., and A.D.G. conceived and designed the experiments, and wrote the manuscript with input from all co-authors. Q.T., E.G., and B.P. performed the generation of experimental cohorts, data collection, analysis and interpretation. Specifically, Q.T. performed calcium imaging. B.P. made the initial observations of leptin and DMH^{LepR} activation's behavioral effects. E.G. and R-J.A-F. conducted the snRNAseq experiments, whereas E.G. analyzed snRNAseq data. C.D.B. and Q.Z. contributed to intracranial surgery. R.O. and T.B.G. contributed

to body weight and food intake measurements during SF. Q.Z. and S.P.W. contributed to DMH^{LepR} neuron chemogenetic activation in constant darkness. C.D.B., E.G. and I.R.S. contributed to immunohistochemistry staining of tissues. E.G., T.B.G., Q.Z. and O.Y.C. contributed to bioluminescence experiments. C.D.B., Q.Z., S.P.W, T.B.G., R.O., A.B., R.S., and J.O. contributed to daily animal husbandry during long-term circadian behavior experiments.

C2.6 Data Availability

All data needed to evaluate the conclusions in the paper are present in the paper and/or the Supplementary Materials. Raw snRNAseq files can be found at gene expression omnibus (GEO) with accession code GSE211757.

C2.7 Materials and Methods

Single Nucleus RNA Sequencing (Figs 1-3, Supplemental Figs 1-4)

Mouse Lines

All experiments were carried out in compliance with the Association for Assessment of Laboratory Animal Care policies and approved by the University of Virginia Animal Care and Use Committee. Animals were housed on a 12-h light/dark cycle with food (PicoLab Rodent Diet 5053) and water *ad libitum* unless otherwise indicated. For generation of the 10X single nucleus RNA-seq data (Figs 1-3, Supplemental Figs 1-4), we used both male and female LepR-cre mice (B6.129-$Lepr^{tm3(cre)Mgmj}$/J, The Jackson Laboratory #032457, RRID:IMSR_JAX:032457) (*277*) crossed to Ai14 tdTomato reporter line (B6.Cg-*Gt(ROSA)26Sor*$^{tm14(CAG-tdTomato)Hze}$/J, Strain #007914, RRID:IMSR_JAX:007914) (*278*).

Scheduled Feeding in Comprehensive Lab Animal Monitoring System (CLAMS)

Indirect calorimetry in the CLAMS system (Columbus Instruments) was used to evaluate metabolic parameters and ambulatory locomotor activity during *ad libitum,* overnight fasted, or time and calorie restricted scheduled feeding (SF). All mice were on a 12:12 light-dark cycle with *ad libitum* access to food and water unless otherwise indicated. Lepr-cre; tdTomato mice were singly housed and acclimated to the CLAMS for 3 days prior to experiment start. The night before SF began, the SF cohort was fasted and cages were changed and thereafter were given 2-3 grams of food, which is ~60% of the normal daily food intake (PicoLab Rodent Diet 5053) at zeitgeber time (ZT) 6 for 10 days. The overnight fasted cohort had *ad libitum* food access until the night before sacrifice, when food was removed and cages were changed. We repeated this experiment a total of 3 times with 2 mice per condition each time (n = 6 mice / condition total).

Brain Extraction and Microdissection

All mice were sacrificed at ZT 5. Brains were immediately extracted and dropped into ice cold Hanks' Balanced Salt Solution (HBSS). After 2 minutes, brains were embedded in low melting point agarose (Precisionary Instruments, Natick, MA) and sectioned at 400 μm on a Compresstome VF-200 Vibrating Microtome (Precisionary Instruments, Natick, MA, USA) into DNAse/RNAse free 1x PBS. Hypothalamic sections of interest were immediately collected into RNAprotect (Qiagen, Hilden, Germany) and kept in RNAprotect at 4^{o}C overnight. The next day Lepr-Cre; TdTomato positive cells were visualized using a fluorescent stereoscope (Leica, Wetzlar, Germany). tdTomato fluorescence was used to approximate DMH and SCN boundaries during microdissection of these regions. DMH and SCN microdissected tissue samples were placed into Eppendorf tubes separated by brain region and feeding condition, and stored in -80^{o}C until nuclei isolation.

Isolation of Single Nucleus for RNA sequencing

DMH and SCN microdissected tissue samples were transferred from a -80°C freezer and into individual 2mL glass dounce homogenizer tubes (Kimble, Vineland, NJ, USA) to be homogenized according to a protocol modified from the method described previously (*279*). Tissue was homogenized in 1mL of buffer (16mM sucrose, 5mM CaCl, 3mM $Mg(Ac)_2$, 10mM Tris pH 7.8, 0.1mM EDTA, 1% NP40, 1mM beta-mercaptoethanol in H_2O) on ice, with 25 passes of pestle A and 25 passes of pestle B. An additional 4mL of buffer was added to the nuclei suspension and placed on ice for 5 minutes. Then 5 mL of 50% OptiPrep Density Gradient Medium [Sigma Aldrich, MO, USA] (30mM CaCl, 18mM $Mg(Ac)_2$, 60mM Tris pH 7.8, 0.1 mM PMSF, 6mM beta-mercaptoethanol in H_2O; in 60% (w/v) solution of iodixanol in sterile water) was added to nuclei on ice and inverted 10 times to mix. The nuclei suspension was layered onto 10 mL of 29% OptiPrep solution (Buffer + 50% OptiPrep) in a 38.5 mL Ultra-Clear tube (Beckman-Coulter, CA, USA) before being centrifuged at 7,333g for 30 minutes at 4°C. Supernatant was discarded and the nuclei pellet was resuspended in 1x PBS + 1% BSA (Sigma-Aldrich, MO, USA) + 2 mM Mg^{2+} + 0.1% RNase inhibitor (Sigma-Aldrich, MO, USA) for 15 minutes on ice. The nuclei suspension was pipetted through a 20 µm mesh filter along with 2 drops of propidium iodide (PI) Ready Flow reagent (Thermo Fisher, MA, USA) and immediately taken on ice to be FACS sorted using an SH800 (Sony, Tokyo, Japan) cell sorter. Sorting was gated to select for PI+ single nucleus. Nuclei were sorted through a 70 µm nozzle into a 2mL LoBind collection tube (VWR, PA, USA) containing 18.8uL of RT Reagent B from the Chromium Next GEM Single Cell 3' Reagent Kit v3.1. The remaining components of the 10X Step 1 mastermix were then gently mixed with the contents of the FACS collection tube and loaded into the 10X Genomics Chromium Controller Chip G.

Single-Nucleus RNA-Seq Workflow

The single-nucleus samples were processed into sequencing libraries using the Chromium Next GEM Single Cell 3' Reagent Kit v3.1 according to the manufacturer's protocol (version 3.1,

revision D). After generation of the GEMs (Gel Bead-In EMulsions) and reverse transcription of poly-adenylated mRNA, cDNA was amplified (10-14 cycles), enzymatically fragmented, and ligated to Illumina adapters. Sequencing libraries were indexed, size selected for 400-600 bp using SPRIselect (Beckman Coulter, Indianapolis, IN, USA), and quantified by Qubit (v4.0, 1X high-sensitivity dsDNA kit, Thermo Scientific) and Bioanalyzer (Agilent, Santa Clara, CA, USA). Size-corrected library concentrations were used to pool libraries for equimolar representation. The pooled concentration was measured by KAPA Library Quant qPCR according to the manufacturer's instructions (KAPA Biosciences, Wilmington, MA) and by Qubit. Library pools were sequenced using a P100 cycle kit on the NextSeq 2000 (Illumina, CA, USA) in the University of Virginia School of Medicine Genome Analysis and Technology Core, RRID:SCR_018883. The sequencing structure was as follows: Read 1 was 28 bp (16 bp barcode, 12 bp UMI), Read 2 was 98 bp (cDNA) and Index 1 was 8 bp (single index). Overall, we had 7 DMH and 5 SCN sequencing library pools. 10X Batch 1 & 2 contained mixed pools of all feeding conditions, but 10X Batch 3 contained a unique feeding condition per library pool (Supplemental Fig. 1A, E).

Single-Nucleus RNA-Seq Data Processing

Raw digital expression matrix files for each sequencing run were transferred to a high-performance cluster (HPC) server where they were demultiplexed based on sample index. We generated fastq files with bcl2fastq2 version 2.20.0, then used Cell Ranger version 5.0.0 to align transcripts to the Cell Ranger supplied mouse genome, mm10 2020-A (GENCODE vM23/Ensembl 98), quantify expression levels, and partition them according to their cell-specific barcode. We ran the Cell Ranger count program with the ”--include-introns” argument to include intronic reads in the gene expression quantitation.

Single-Nucleus RNA-Seq Analysis

Cell Ranger h5 files were read into Seurat v4 (*280*) in R (version 4.1.0) and RStudio (version 1.4.1717) and merged by brain region (DMH, SCN) for clustering analysis. We filtered the initial datasets to remove low quality samples (i.e., cells with less than 100 genes detected or greater than 0.5% mitochondrial reads). We then log-normalized the data; selected 2,000 most variable genes ("feature selection"), and scaled gene expression. We performed Principal Component Analysis (PCA) to linearly reduce the dimensionality of the highly variable gene set. We defined distance metrics based on K-nearest neighbor analysis, grouped cells with Louvian algorithm modality optimization, and visualized cell embeddings in low-dimensional space with Uniform Manifold Approximation and Projection (UMAP) nonlinear dimensionality reduction. To focus our analysis on neurons, we subsetted neuronal clusters based on their enriched expression of neuronal marker genes (*Syt1*, *Syn1*, *Tubb3*). To correct for batch effects, we integrated across sample batches using Seurat's function for reciprocal principal component analysis (RPCA). Next, we subsetted region-specific clusters based on expression of positive and negative marker genes for each target brain region (SCN, DMH), as described in the next section. We reclustered the identified DMH and SCN neurons using the following parameters: DMH, 2,000 most variable genes, first 15 PCs, resolution setting of 0.8; SCN, 2,000 most variable genes, first 13 PCs, resolution setting of 0.5 Finally, we assessed cluster markers with the Wilcoxon Rank Sum test using Seurat default settings. Cluster markers were selected based on top p-values (adjusted to correct for multiple comparisons), high percent expression within the cluster and low percent expression outside of the cluster, and validated based on Allen Brain Atlas mouse *in situ* hybridization data and previous literature.

Identification of DMH and SCN neurons

DMH neuron types were selected based on previously reported markers (*259*), as well as known highly expressed genes in the DMH including *Lepr, Pdyn, Ppp1r17, Cck* and *Grp (254, 266, 277)*. Markers were validated via the Allen Brain Atlas mouse *in situ* hybridization data.

Additionally, clusters enriched with genes expressed in surrounding hypothalamic regions but not DMH were excluded from further analysis, including the following: PVH (*Sim1*) (*281*), VMH (*Slit3, Qrfpr, Arpp21, Nr5a1, Fezf1*) (*282*), Arc (*Prlr, Nr5a2*) (*32*), LH (*Pvalb, Klk6, Nts*) (*283*, *284*) , or the tuberomammillary nucleus (*Hdc*) (*285*)[, (286)]. Cluster markers were prioritized based on multiple-comparison adjusted p-values, high percent expression within the cluster and low percent expression outside of the cluster. We defined SCN neuron populations based on previous literature by plotting expression of cluster specific markers and circadian genes from published datasets by our clusters (*247*, *248*, *287*)**.**

Functional Analysis of Differentially Expression Genes

To find differential gene expression between feeding condition groups (*ad libitum*, fasted, SF), we used Seurat's 'FindMarkers' function to run Wilcoxon Rank Sum statistical tests. False Discovery Rate (FDR) was calculated using the 'p.adjust' function. We set cutoffs of log2FC > 0.25 and FDR < 0.05 to quantify the total number of differentially expressed genes per feeding condition comparison. To visualize STRING functional protein interaction networks, we used Cytoscape open-source software (version 3.9.1). We input lists of differentially expressed genes in the cluster 13_Lepr between both SF and fasted and SF and *ad libitum* using the same criteria as previously described above. We ran KEGG functional enrichment analysis on the mouse genome to label genes involved in upregulated pathways during SF. We measured differentially expressed pathways among the three feeding conditions using the 'enrichR' package. To visualize genes and pathways differing significantly between feeding conditions, we used the 'DEenrichR' function which applies the Wilcoxon Rank Sum test to identify differentially expressed (DE) genes (log2(fold change) > 0.25, multiple-comparison adjusted p < 0.05). Significantly DE genes are then scored based on odds ratios to fall into pathways categories defined by the Kyoto Encyclopedia of Genes and Genomes (KEGG) 2019 Mouse database. With the 'ggplot2' package, we then graphed upregulated and downregulated pathways in each

comparison on a superimposed bar graph, colored by condition specific comparison, and ranked by maximum -log10(pvalue).

RNA Fluorescence In Situ Hybridization

RNA fluorescence *in situ* hybridization (RNA FISH) was performed on fixed brain slices with a probe to detect LepR and Pdyn RNA (RNAscope Multiplex Fluorescent Reagent Kit v2 Assay, ACD). All procedures were carried out according to the manufacturer's instructions. Briefly, sections were pretreated with RNAscope hydrogen peroxide to block the activity of endogenous peroxidases. After a wash in distilled water, sections were permeabilized with RNAscope protease IV for 30 min at 40°C. Sections were hybridized with the Lepr (ACD, cat# 402731), Pdyn (ACD, cat# 318771) and Glra2 (ACD, cat#510301) probe at 40°C for 2 h, followed by amplification incubation steps: Amp 1, 30 min at 40°C; Amp 2, 30 min at 40°C; Amp 3, 15 min at 40°C. HRP signals were developed with RNAscope Multiplex FL v2 HRP and TSA Plus fluorophores (HRP-C1 and 1:750 TSA Plus Cy3 for Lepr, Cy2 or Cy5 for Pdyn, Cy5 for Glra2). Sections were washed with the provided washing buffer 2 × 2 min in between each step. Sections were then coverslipped with DAPI Fluoromount-G (Southern Biotech). Confocal microscope imaging was performed on a Zeiss LSM 800 microscope (Carl Zeiss).

Automated quantification for RNA FISH images

RNA FISH labeled cells were counted using CellProfiler image analysis software, with an analysis pipeline modified from previously published work (*288*). In brief, DAPI staining of nuclei was used to identify cells, and then cells with more than three stained speckles, or >60% of cell area covered by staining, were considered as positive for the marker.

C2.8 Supplemental Figures

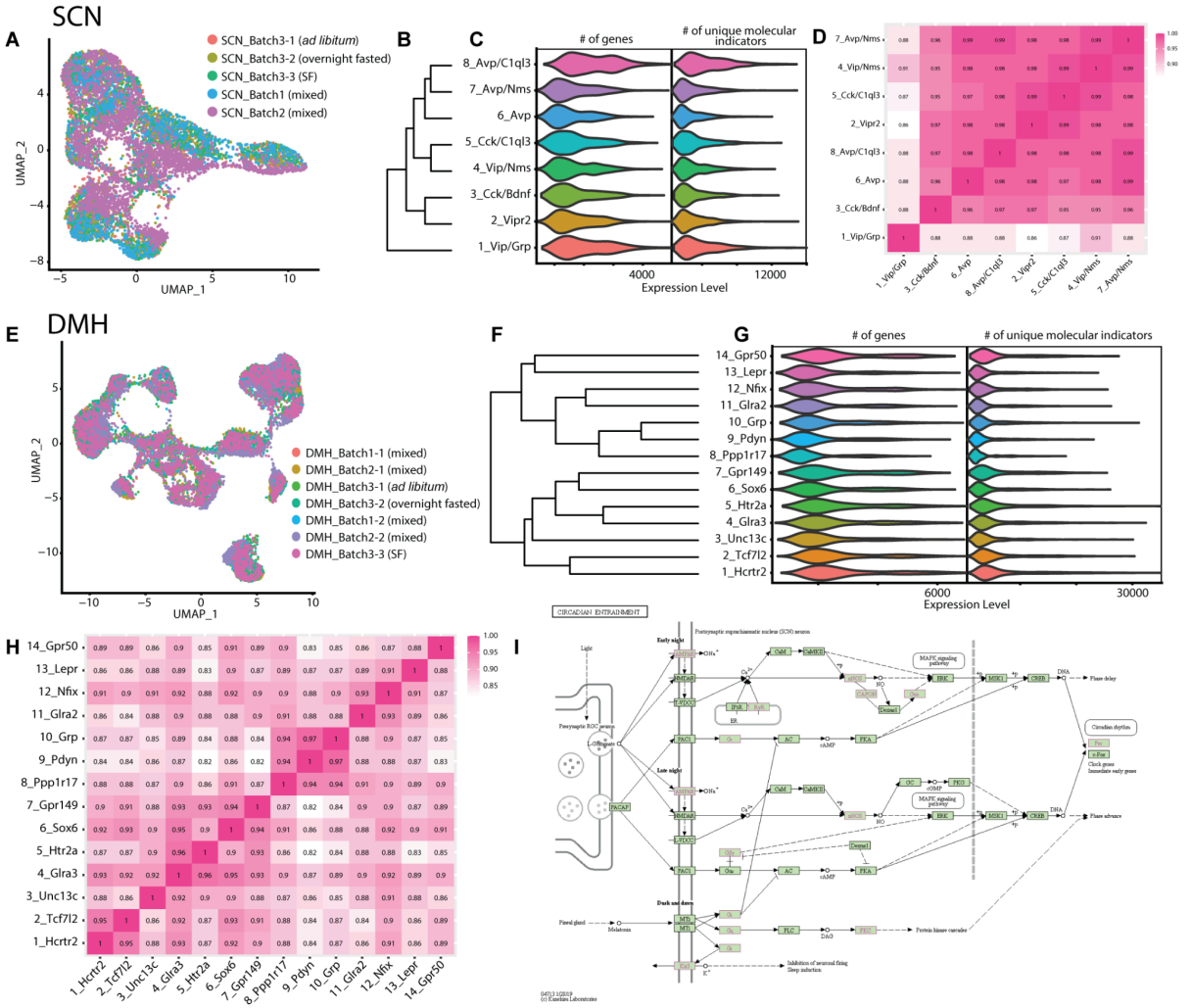

Supplemental figure 1- SCN and DMH single nuclei RNA-seq quality metrics and marker expression. A. (Elizabeth Godschall) UMAP of SCN neurons, colored by sequencing library identity, after batch correction. **B. (Elizabeth Godschall)** Phylogenetic tree indicating the relatedness of 8 SCN neuronal clusters. **C. (Elizabeth Godschall)** Expression level distribution of number of genes per cluster (left) and number of UMIs (unique molecular identifiers, representing unique gene transcripts; right) in SCN clusters. **D. (Elizabeth Godschall)** Correlation matrix of average expression of all genes between SCN neuronal clusters. Values within the boxes are Pearson correlation coefficients. **E. (Elizabeth Godschall)** UMAP of DMH neurons, colored by sequencing library identity, after batch correction. **F. (Elizabeth Godschall)** Phylogenetic tree indicating the relatedness of 14 DMH neuronal clusters. **G. (Elizabeth Godschall)** Expression level distribution of the number of genes per cluster (left) and number of UMIs (right) among DMH clusters. **H. (Elizabeth Godschall)** Correlation matrix of average expression of all genes within DMH neuronal clusters. Values within the boxes are Pearson correlation coefficients. **I. (Elizabeth Godschall)** KEGG circadian entrainment pathway map.

The genes upregulated (Supplemental Fig. 4C) in DMH^{LepR} neurons during SF are labeled as pink on the map.

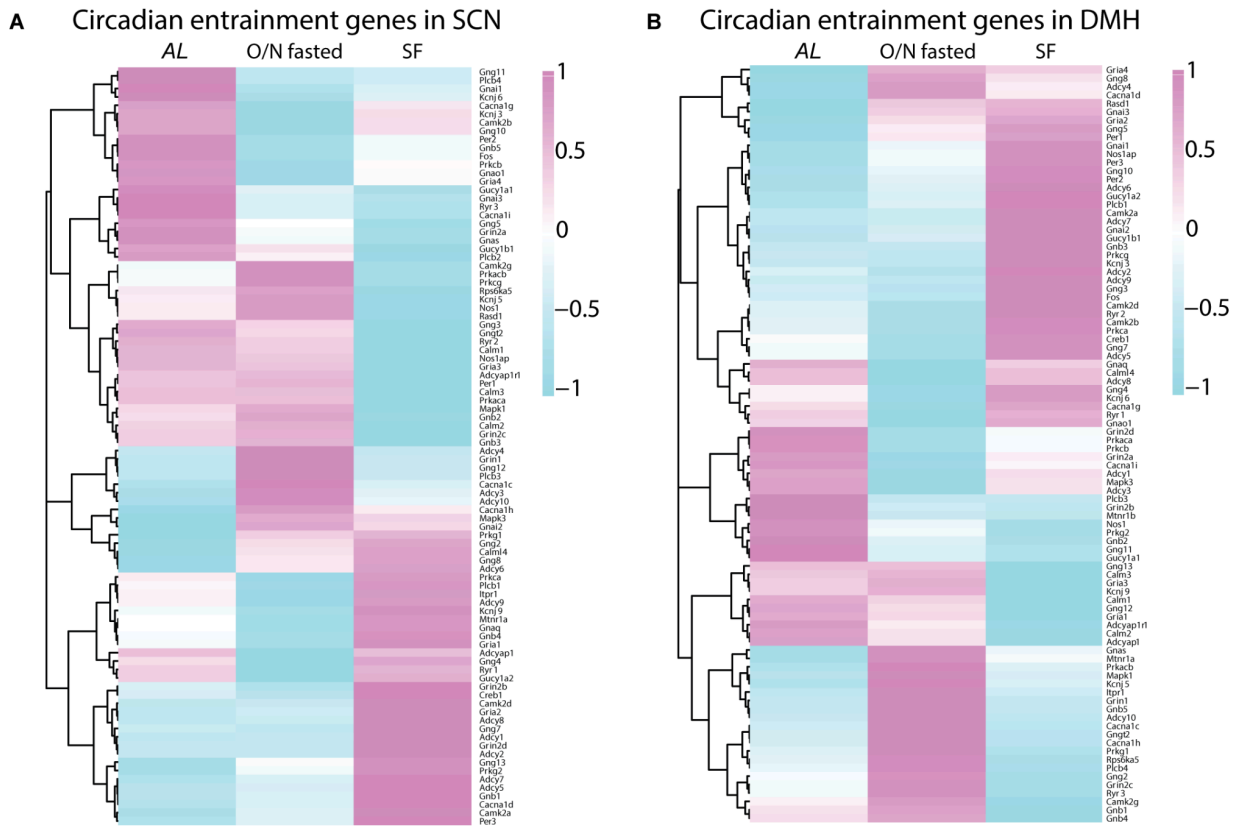

Supplemental figure 2- Relative expression level of KEGG circadian entrainment pathway across feeding conditions in SCN and DMH. A. (Elizabeth Godschall) Heatmap of all the genes in the KEGG circadian entrainment pathway across feeding conditions in SCN. **B. (Elizabeth Godschall)** Heatmap of all the genes in the KEGG circadian entrainment pathway across feeding conditions in DMH.

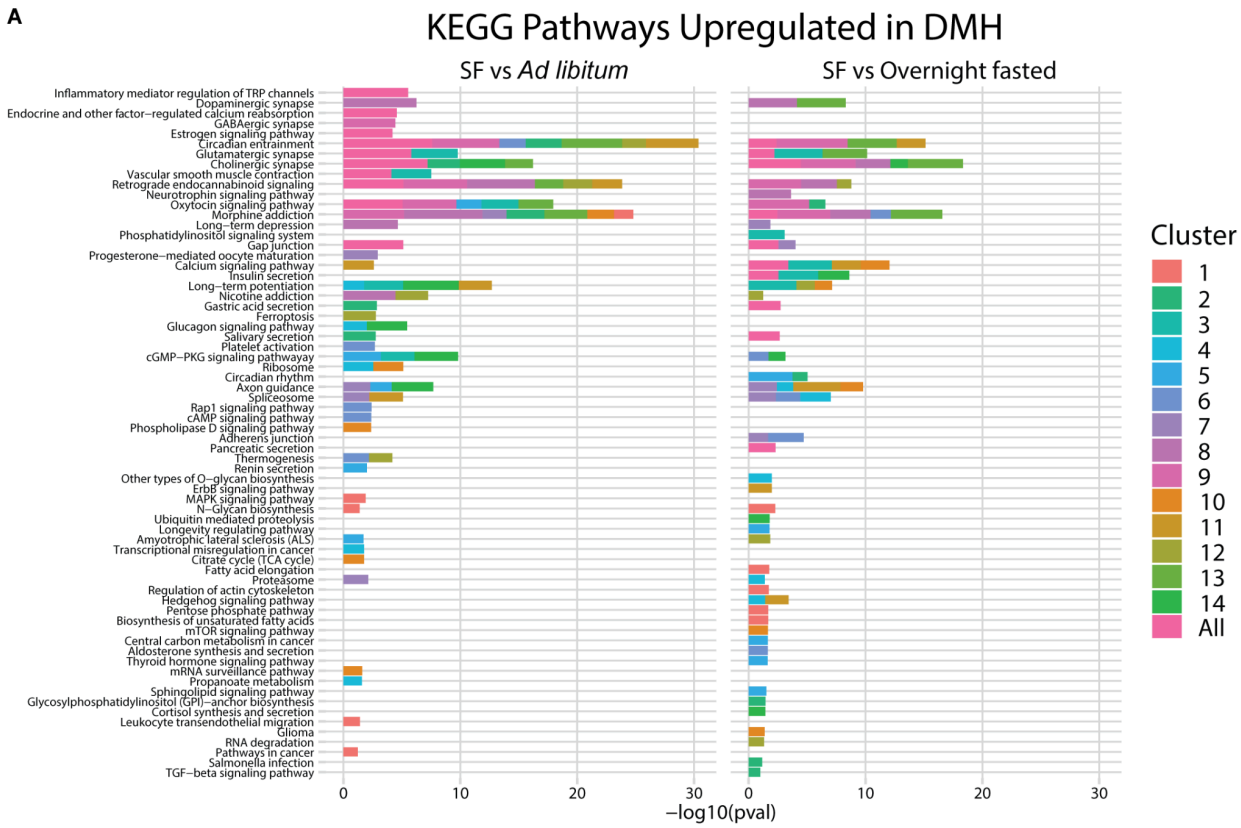

Supplemental figure 3- Cluster specific alteration of pathways in the DMH. A. (Elizabeth Godschall) Gene enrichment analysis comparing pathways upregulated among SF vs *ad libitum* and SF vs fasted feeding conditions in each DMH neuronal cluster and upregulated pathways in all DMH neurons, using KEGG Mouse 2019 database. Bars are colored by clusters. Inclusion criteria required p-value <0.05 and log2 fold change >0.25.

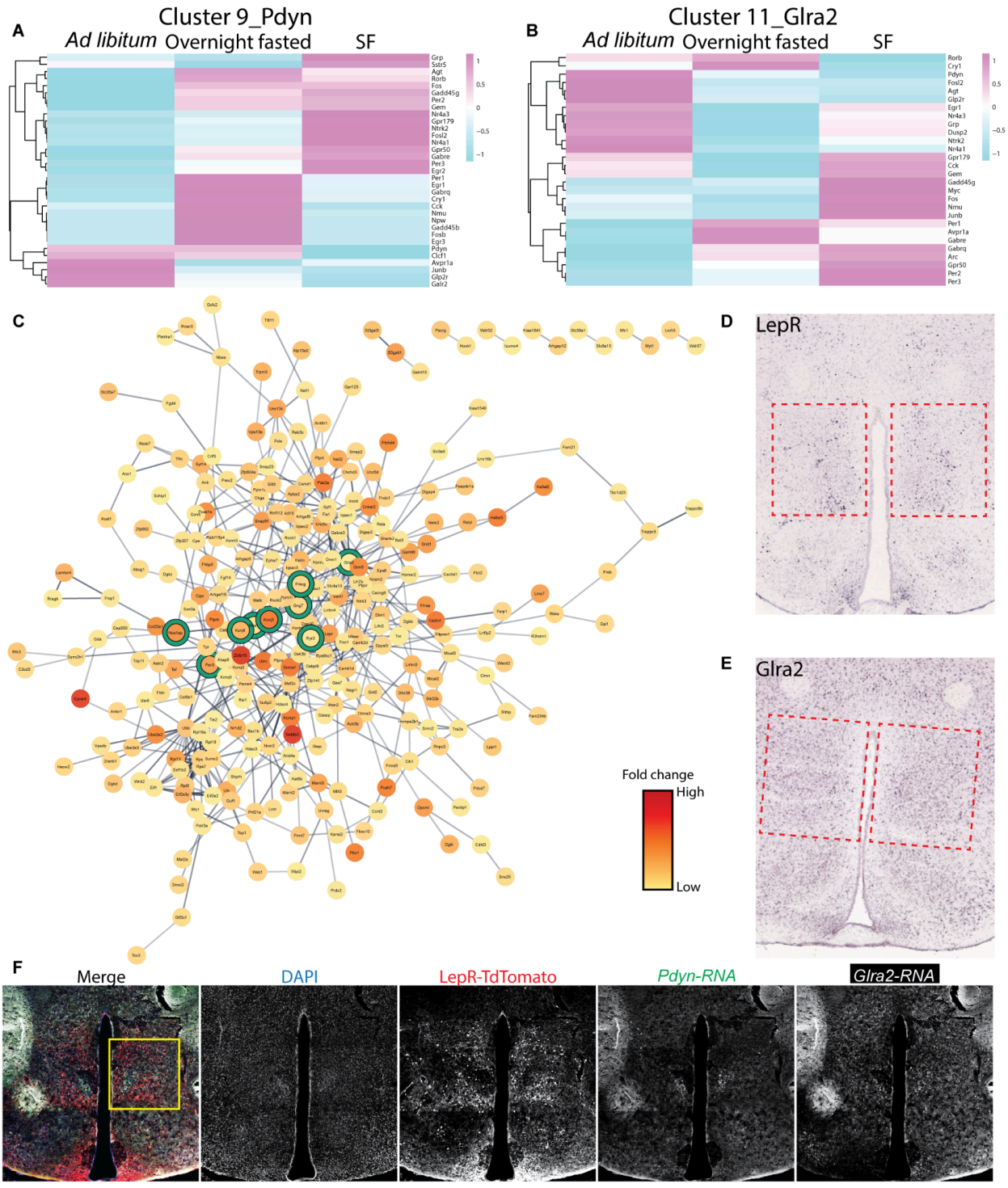

Supplemental figure 4- Network analysis of differentially expressed genes in the DMH between fasted and *ad libitum* conditions compared to scheduled feeding. A. (Elizabeth Godschall) Heatmap indicating expression level of genes up and downregulated among feeding conditions in the 9_Pdyn cluster. **B. (Elizabeth Godschall)** Heatmap indicating expression level of genes up and downregulated among feeding conditions in the 11_Glra2

cluster. **C.** STRING known and predicted protein interactions using Cytoscape platform to visualize molecular networks. Input genes were derived from cluster 13_Lepr differential testing using the Wilcoxon Rank Sum Test to compare SF to *ad libitum* and SF to fasting. Inclusion criteria required False Discovery Rate <0.05 and log2 fold change >0.25. The color of circles indicates the level of average log2 fold change between SF and fasting or *ad libitum* conditions. Functional enrichment of genes involved in circadian entrainment defined by KEGG 2019 database are circled in green. **D-E (Qijun Tang) .** *In situ* hybridization (ISH) of the RNA for (D) LepR, and (E) Glra2 on the brain sections that contain DMH (outlined by red boxes). The images are from Allen Mouse Brain Atlas (https://mouse.brain-map.org/search/index). **F. (Elizabeth Godschall, Qijun Tang)** Representative coronal section image showing the localization of LepR, Pdyn and Glra2 cells in the DMH. LepR cells were marked by LepR-Cre; TdTomato protein, Pdyn and Glra2 cells were marked by RNA FISH. The area indicated by the yellow box was re-imaged and presented as a zoomed-in representative image in Fig. 2H.

Chapter 3. A Brain Reward Circuit Inhibited By Next-Generation Weight Loss Drugs

Authors

Elizabeth N. Godschall[1†], Taha Bugra Gungul[1†], Isabelle R. Sajonia[1†], Aleyna K. Buyukaksakal[1], Sophia Ogilvie[1], Austin B. Keeler[1], YuChen Zhang[2], Tyler C. J. Deutsch[3], Yu Shi[1], Nicholas J. Conley[2], Addison N. Webster[2], O. Yipkin Calhan[1], Amani Akkoub[1], Karan Malik[1], Kaleigh I. West[1], Arun Karthikeyan[1], Grace van Gerven[1], Manoj K. Patel[3], John N. Campbell[1,2,4], Christopher D. Deppmann[1,2,4-6*], Ali D. Güler[1,2,4*]

[1]Department of Biology, University of Virginia; Charlottesville, VA 22904, USA.

[2]Department of Neuroscience, School of Medicine, University of Virginia; Charlottesville, VA 22903, USA.

[3]Department of Anesthesiology, University of Virginia Health System, Charlottesville, VA 22904, USA.

[4]Program in Fundamental Neuroscience; Charlottesville, VA 22904, USA.

[5]Department of Cell Biology, University of Virginia; Charlottesville, VA 22904, USA.

[6]Department of Biomedical Engineering, University of Virginia; Charlottesville, VA 22904, USA.

*Corresponding author. Email: aguler@virginia.edu and deppmann@virginia.edu.

[†]These authors contributed equally to this work.

This chapter is in revision at *Nature* and published in bioRxiv in December 2024. doi: https://doi.org/10.1101/2024.12.12.628169. This work was in close collaboration with Bugra Gungul and Isabelle Sajonia. All author's major contributions are highlighted in figure legends.

C3.1 Abstract

Glucagon-like peptide-1 receptor agonists (GLP1RAs) effectively reduce body weight and improve metabolic outcomes, yet established peptide-based therapies require injections and complex manufacturing. Small-molecule GLP1RAs promise oral bioavailability and scalable manufacturing, but their selective binding to human versus rodent receptors has limited mechanistic studies. The neural circuits through which these emerging therapeutics modulate feeding behavior remain undefined, particularly in comparison to established peptide-based GLP1RAs. Here, we developed humanized GLP1R mouse models to investigate how small-molecule GLP1RAs influence feeding behavior. Integrating genetic manipulations, calcium imaging, and behavior profiling, we discovered that these compounds regulate both homeostatic and hedonic feeding through parallel neural circuits. Beyond engaging canonical hypothalamic and hindbrain networks that control metabolic homeostasis, GLP1RAs recruit a discrete population of Glp1r-expressing neurons in the central amygdala, which selectively suppress the consumption of palatable foods by reducing dopamine release in the nucleus accumbens. Stimulating these central amygdalar neurons curtail hedonic feeding, whereas targeted deletion of the receptor in this cell population specifically diminishes the anorectic efficacy of GLP1RAs for reward-driven intake. These findings reveal a dedicated neural circuit through which small molecule GLP1RAs modulate reward processing, suggesting broad therapeutic potential in conditions of dysregulated dopamine signaling including substance use disorder or binge eating.

C3.2 Main

The global obesity epidemic has catalyzed an urgent search for effective pharmacological interventions, with glucagon-like peptide-1 receptor agonists (GLP1RAs) emerging as leading candidates. These compounds, notably liraglutide (Saxenda, Victoza) and semaglutide (Wegovy, Ozempic), promote weight loss by enhancing insulin secretion, suppressing glucagon

release, and inducing satiety (**Fig. 1a,b**)(*177*, *180*, *289–291*, *292*, *293–303*). Recent studies have highlighted crucial roles for hypothalamic and hindbrain regions in GLP1RA-mediated feeding suppression(*304–311*). However, peptide-based GLP1RAs require injection, cold storage, and complex manufacturing processes, with widespread global supply chain issues restricting patient access(*312–315*). Next-generation small-molecule GLP1RAs like danuglipron (PF06882961) and orforglipron (LY3502970) offer transformative advantages through oral bioavailability and scalable manufacturing (**Fig. 1a**)(*316*, *317–322*). Yet a critical challenge in developing these compounds has been their species-specific binding properties—many small-molecule GLP1RAs that effectively activate human GLP1R show minimal activity at rodent receptors, severely limiting preclinical investigation of their mechanisms of action(*321*, *323*, *324*, *325*). Notably, orforglipron has advanced into over ten registered Phase 3 clinical trials(*317–319*, *326*). The imminent clinical deployment of these small-molecules demands urgent investigation of their neural mechanisms, particularly given emerging evidence of GLP1RAs' effects on mood, motivation, and reward processing(*327–331*).

To overcome the species specificity of small-molecule GLP1RAs and enable preclinical investigation of their neural mechanisms, we engineered humanized GLP1R mouse models, providing an essential platform for *in vivo* studies that would otherwise be unattainable. Through integrated behavioral, neuroanatomical, and functional analyses, we uncovered a previously unknown multi-synaptic hindbrain-amygdala-midbrain circuit that specifically modulates rewarding food consumption through striatal dopaminergic signaling. This discovery advances our understanding of how Glp1R signaling influences not only feeding behavior but also fundamental reward processes, including addiction, mood disorders, and motivation(*293–303*, *332*), highlighting both the therapeutic potential and the need for caution as these treatments see broader use.

C3.2.1 Generation and Validation of Humanized Glp1r^{S33W} Mice for Investigating Small-Molecule GLP1RAs

While peptide GLP1RAs, like liraglutide, reduce food consumption in C57BL6J mice, many small-molecule GLP1RAs do not effectively activate rodent Glp1r (**Fig. 1b**) due to a single amino acid difference from tryptophan to serine at position 33 (**Fig. 1c**)(*323*), (*324*, *325*). Using CRISPR-Cas9-mediated genome editing, we inserted the S33W mutation into the mouse *Glp1r* locus, effectively humanizing it (**Fig. 1d,e**). Homozygous humanized Glp1r S33W mice (Glp1r^{S33W}) and wild type (WT) littermates did not exhibit differences in respiratory exchange ratio (RER) (**Extended Data Fig. 1a-d**), energy expenditure (EE) (**Extended Data Fig. 1e-h**) or body weight (**Extended Data Fig. 1i-j**), demonstrating that Glp1r^{S33W} mice maintain normal metabolic functions and energy homeostasis comparable to WT littermates. To evaluate the *in vivo* functionality of the S33W mutation, we performed glucose tolerance tests (GTT) and found that liraglutide improved glucose tolerance in both Glp1r^{S33W} mice and WT mice (**Fig. 1f**), whereas danuglipron and orforglipron were effective only in Glp1r^{S33W} mice (**Fig. 1g,h**). These results demonstrate that Glp1r^{S33W} mice retain responsiveness to peptide-based GLP1RAs while gaining sensitivity to human-specific small molecule GLP1RAs, establishing a valuable *in vivo* model system for investigating this next-generation class of drugs.

C3.2.2 Small-Molecule GLP1RAs Mirror Liraglutide Effects in Suppressing Feeding in Glp1r^{S33W} Mice

GLP1RAs induce significant weight loss through multiple mechanisms beyond their effects on insulin secretion and glucose control(*177*, *180*, *182*, *318*). To systematically characterize their impact on distinct feeding modalities, we employed parallel behavioral paradigms examining both homeostatic and hedonic feeding patterns. Homeostatic feeding was quantified through standard diet (SD) consumption during the active-phase (zeitgeber time (ZT)12-16), while

hedonic feeding was assessed via high-fat diet (HFD) intake during the inactive-phase (ZT2-6) when baseline SD consumption is minimal(*273*, *109*, *333*). In Glp1r^{S33W} mice, administration of liraglutide, danuglipron, and orforglipron significantly attenuated both active-phase SD (**Fig. 1j,l,n**) and inactive-phase HFD (**Fig. 1p,r,t**) consumption compared to vehicle controls. As predicted by the species specific receptor activation profile, WT mice exhibited reduced SD (**Fig. 1i,k,m**) and HFD (**Fig. 1o,q,s**) intake exclusively following liraglutide administration. Notably, both liraglutide and orforglipron demonstrated sustained 24-hour inhibition of food intake (**Extended Data Fig. 2a-c**), consistent with their extended pharmacokinetic profiles relative to danuglipron (**Fig. 1a**). To validate the clinical relevance of these orally bioavailable small-molecule GLP1RAs, we confirmed that oral danuglipron significantly reduced blood glucose levels (**Fig. 1u**) and acute HFD intake comparable to intraperitoneal injection effects (**Fig. 1v, w**). Similarly, oral orforglipron inhibited acute HFD intake (**Fig. 1x,y**) and its chronic daily administration in overweight Glp1r^{S33W} mice significantly reduced body weight compared to saline controls (**Fig. 1z**), establishing its efficacy in weight management(*318*) .

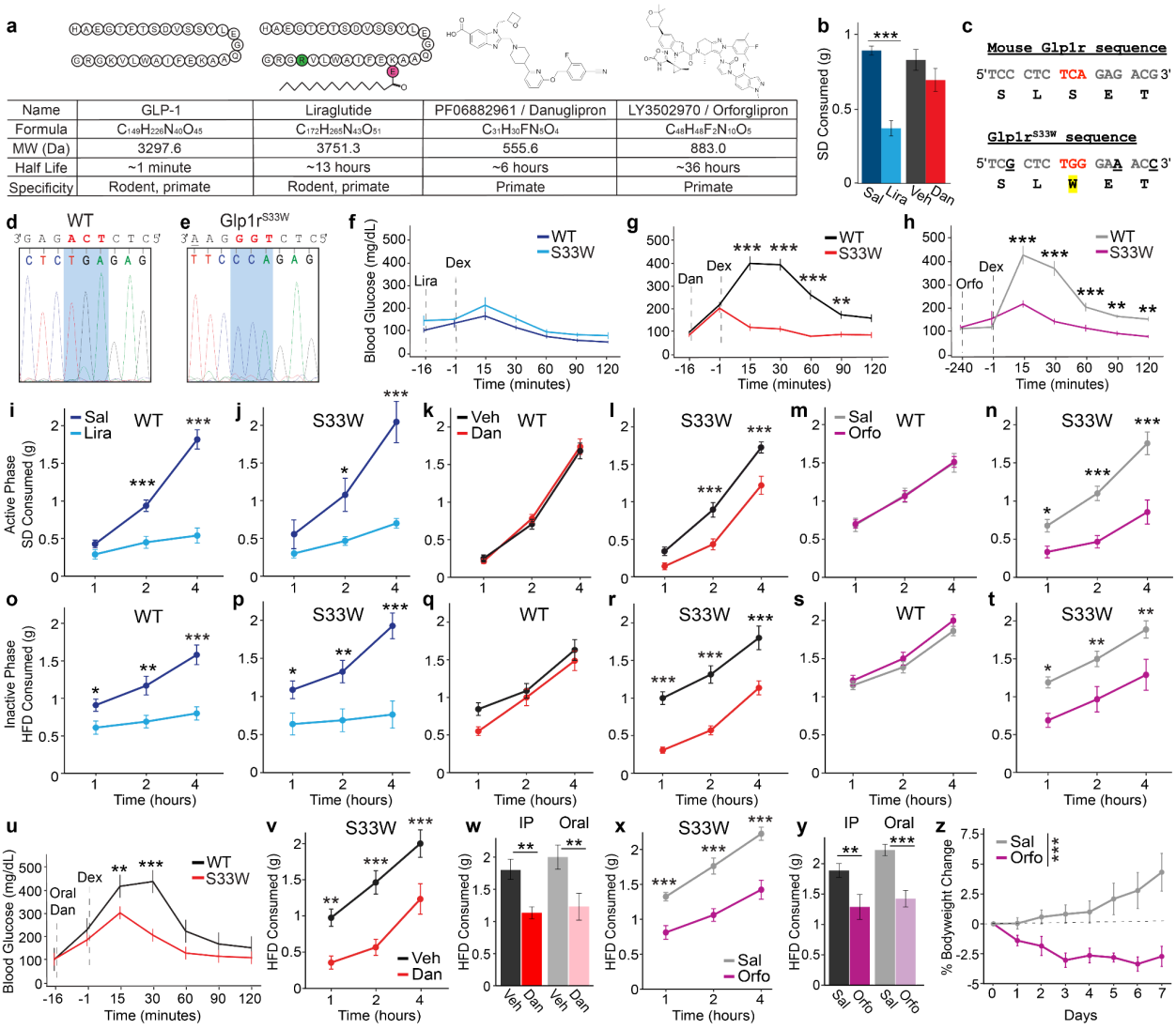

Figure 1: Generation and validation of a novel mouse model responsive to small molecule GLP1R agonists: a, **(Elizabeth Godschall)** Structure, naming convention, molecular formula, molecular weight (MW), half-life in humans, and species binding specificity of glucagon-like peptide-1 (GLP-1), liraglutide, danuglipron, and orforglipron. Amino acid sequences of liraglutide shown with its substitution and additions to GLP-1 highlighted in green and purple, respectively. **b**, **(Elizabeth Godschall)** Standard diet (SD) consumption over 2 hours post-administration of saline (Sal), liraglutide (Lira), vehicle (Veh), or danuglipron (Dan) (*n* = 11 per injection, one-way ANOVA with Bonferroni correction, ***P<0.001). **c**, **(Elizabeth Godschall)** Schematic of the serine (TCA or S) to tryptophan (TGG or W) CRISPR-mediated substitution in Glp1r^{S33W} (bottom) or in mouse Glp1r (top). **d,e**, **(Elizabeth Godschall, Austin Keeler, Tony Spano, Aleyna Buyukaksakal)** Sanger sequencing chromatograms of (**d**) WT mouse Glp1r and (**e**) Glp1r^{S33W} sequence, confirming the Glp1r S33W substitution in mice. **f-h**, **(Elizabeth Godschall)** Glucose tolerance test (GTT) on GLP1RAs. Comparison of blood glucose levels on (**f**) liraglutide (Lira), (**g**) danuglipron (Dan), (**h**) orforglipron (Orfo) followed by dextrose (Dex) in WT and Glp1r^{S33W} mice (*n* = 5-9 per injection, two-way ANOVA with Bonferroni

correction, **P<0.01; ***P<0.001). **i-n**, **(Elizabeth Godschall)** SD intake 1, 2, and 4 hours post-treatment of (**i, j**) Lira (n = 9-11), (**k, l**) Dan (n = 15-16), and (**m, n**) Orfo (n = 8-9) and vehicle controls in WT and Glp1r^{S33W} mice. **o-t**, **(Elizabeth Godschall)** High fat diet (HFD) intake 1, 2, and 4 hours post-treatment of (**o, p**) Lira (n = 8-10), (**q, r**) Dan (n = 14-16), and (**s, t**) Orfo (n = 8-9) and their vehicle controls in WT and Glp1r^{S33W} mice (two-way ANOVA with Bonferroni correction, *P<0.05; **P<0.01; ***P<0.001). **u**, **(Elizabeth Godschall)** GTT measuring blood glucose levels following oral administration of danuglipron (oDan) and dextrose in Glp1r^{S33W} and WT mice (n = 6 per genotype, two-way ANOVA with Bonferroni correction, **P<0.01; ***P<0.001). **v-y**, **(Elizabeth Godschall)** HFD intake 1, 2, and 4 hours after oral gavage of (**v**) danuglipron or vehicle and (**x**) orforglipron or saline (n = 8-9, two-way ANOVA with Bonferroni correction, **P<0.01; ***P<0.001). Comparison of the 4th hour between intraperitoneal (IP) and oral routes of administration with (**w**) danuglipron or (**y**) orforglipron (two-way ANOVA with Bonferroni correction, **P<0.01; ***P<0.001). **z**, **(Elizabeth Godschall)** 7-day weight changes of mice on chronic HFD treated with orforglipron or saline daily at ZT6 (n = 7 per injection, paired t-test, ***P<0.001). Data are represented as means ± SEM. *P<0.05; **P<0.01; ***P<0.001. See Supplementary Table 1 for statistical details for all figures and Extended Data figures.

C3.2.3 GLP1RAs Exhibit Distinct Neural Activation Patterns in Feeding Circuits

Because small-molecule GLP1RAs may have greater brain penetration than large peptide-based GLP1RAs—potentially leading to distinct neural activation patterns—we aimed to identify the brain regions involved in their inhibition of food consumption. First, we focused on nuclei previously reported to express Glp1r and activated by peptide-based GLP1RAs (**Fig. 2a-d**), specifically the dorsomedial hypothalamus (DMH), nucleus tractus solitarius (NTS), area postrema (AP), and central amygdala (CeA)(*305*, *308–310*, *334–337*). We used cFos expression as a surrogate for GLP1RA-dependent neuronal activation in WT and Glp1r^{S33W} mice receiving an intraperitoneal (IP) injection of danuglipron, orforglipron, or liraglutide (**Fig. 2a-d**). Danuglipron and orforglipron induced significant cFos expression in the NTS (**Fig. 2f**), AP (**Fig. 2g**), and CeA (**Fig. 2h**), but not in the DMH (**Fig. 2e**) of Glp1r^{S33W} mice compared to WT controls, mirroring previous studies using peptide-based GLP1RAs(*305*, *334*, *338*, *339*). As expected, liraglutide induced comparable cFos expression in both groups, matching the small-molecule responses in Glp1r^{S33W} mice across all regions, confirming its effective binding to and activation of the Glp1r^{S33W} variant (**Fig. 2e-h**).

Given that activation of the AP is known to induce nausea and malaise, while Glp1R activation in the NTS signals satiation(*309*, *340*), we aimed to determine whether the relative cFos activation between these two regions could reveal potential mechanisms underlying the differential effects of GLP1RAs observed in clinical trials(*177*, *318*, *341*, *342*). By comparing the ratio of cFos activation in the NTS to that in the AP, we observed significant differences among the drugs tested (**Fig. 2i**). Specifically, orforglipron exhibited greater activation in the NTS and less activation in the AP compared to both danuglipron and liraglutide. To determine whether oral administration of danuglipron replicates the NTS-favored activation pattern observed with orforglipron, we compared intraperitoneal (IP) and oral administration of danuglipron in $Glp1r^{S33W}$ and WT mice (**Fig. 2j,k and Extended Data Fig. 3a-c**). $Glp1r^{S33W}$ NTS cFos activation was comparable between both routes, but oral delivery significantly reduced AP cFos activation (**Fig. 2l**). These findings indicate that oral danuglipron, its designed route of administration, replicates the NTS-favored activation pattern while minimizing AP activation. This preferential activation is advantageous because it may reduce negative side effects associated with AP activation, such as nausea and malaise, while preserving therapeutic effects mediated by the NTS. Therefore, orally delivered small-molecule GLP1RAs represent a promising advancement in weight loss therapies by enhancing both efficacy and tolerability (**Fig. 1u-y**).

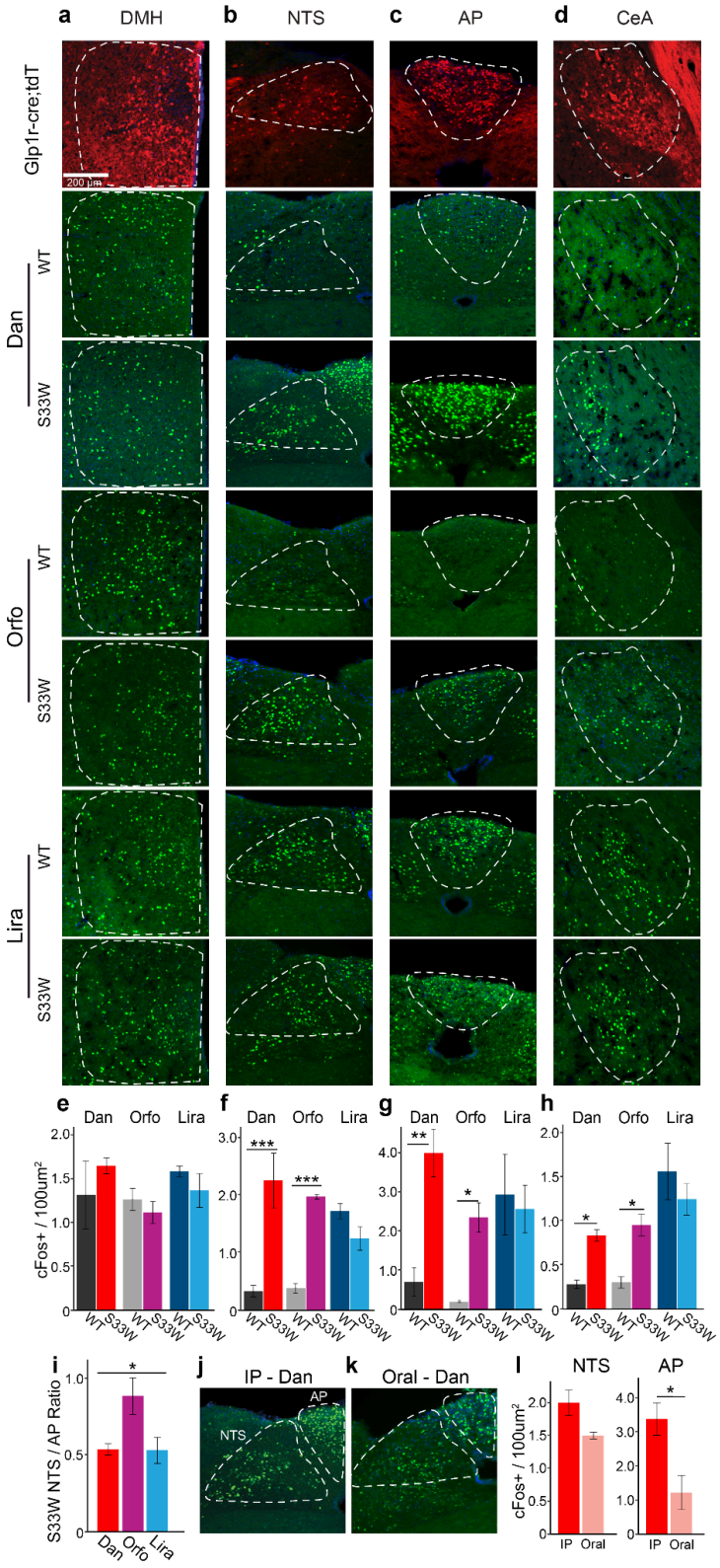
a DMH
b NTS
c AP
d CeA
Glp1r-cre;tdT
200 µm
Dan
Orfo
Lira
WT
S33W
e
f
g
h
Dan Orfo Lira
cFos+ / 100um²
WT S33W WT S33W WT S33W
i
S33W NTS / AP Ratio
Dan Orfo Lira
j IP - Dan
k Oral - Dan
NTS
AP
l
NTS
AP
cFos+ / 100um²
IP Oral
IP Oral

Figure 2: GLP1RA activation across targeted GLP1R-expressing brain regions. **a-d**, **(Elizabeth Godschall, YuChen Zhang)** GLP1R protein expression validated by a Glp1r-Cre;tdTomato mouse line and neuronal cFos activation 2 hours after danuglipron or liraglutide or 6 hours after orforglipron injection in WT and $Glp1r^{S33W}$ mice in the (**a**) DMH, (**b**) NTS, (**c**) AP, or (**d**) CeA. Scale bars = 200 μm. **e-h**, **(Elizabeth Godschall)** Quantification of cFos in the (**e**) DMH, (**f**) NTS, (**g**) AP and (**h**) CeA (*n* = 3-4 per genotype, two-way ANOVA with Bonferroni correction, **P*<0.05; ***P*<0.01; ****P*<0.001). **i**, Ratio of NTS/AP cFos activation in $Glp1r^{S33W}$ mice after danuglipron, orforglipron, and liraglutide (*n* = 3-4 per injection, Kruskal-Wallis test, **P*<0.05). **j,k**, **(Elizabeth Godschall)** Neuronal cFos activation in the NTS and AP 2 hours after danuglipron was administered to $Glp1r^{S33W}$ mice via (**j**) IP injection or (**k**) oral gavage. **l**, **(Elizabeth Godschall)** Quantification of cFos expression in the NTS (left) or AP (right) following danuglipron IP or oral delivery in $Glp1r^{S33W}$ mice (*n* = 3 per delivery route, Welch's t-test, **P*<0.05). Data are represented as means ± SEM. **P*<0.05; ***P*<0.01; ****P*<0.001.

C3.2.4 Danuglipron Suppress Food-Motivated Behaviors During Homeostatic and Hedonic Feeding

Building on our observation that peptide-based and small-molecule GLP1RAs produce distinct neuronal activation patterns, we next examined how these differences manifest in the behavior of $Glp1r^{S33W}$ mice. We focused on liraglutide and danuglipron, which share similar pharmacokinetic properties, and monitored mice in a home-cage environment using infrared video over two hours following GLP1RA or vehicle/saline administration in their active phase (ZT12-14) (**Fig. 3a and Extended Data Fig. 4**). By integrating pose estimation (SLEAP(*343*)) with a probabilistic model for behavior classification (Keypoint-MoSeq(*344*)), we identified 23 discrete behaviors corroborated by sensor data (**Fig. 3b-d and Extended Data Fig. 5 & 6**). These behaviors were grouped into five principal categories— food-motivated, drinking, resting, moving, and grooming. Principal component analysis (PCA) revealed that both liraglutide and danuglipron induced significant, overall behavioral shifts from control conditions (**Fig. 3e,f and Extended Data Fig. 7a-d**). Specifically, both treatments similarly reduced feeding and drinking while increasing resting-related activity, suggesting a conserved effect on satiety-related

behaviors (**Fig. 3g-k**). Linear discriminant analysis further supported these findings, clustering the drug-treated groups together and distinctly apart from vehicle and saline controls (**Fig. 3l**).

To determine the influence of danuglipron on hedonic feeding, we examined behavioral patterns in SD and HFD-fed mice during the inactive phase (ZT 3-5). Vehicle-treated HFD-fed mice exhibited a behavioral profile distinct from SD-fed mice, with more food-motivated behaviors and drinking, and less resting (**Fig. 3m and Extended Data Fig. 7g-k**), indicating a diet-induced behavioral shift. In contrast, danuglipron-treated HFD-fed mice closely resembled their SD-fed counterparts, showing similar levels of food-motivated activity, drinking, movement, and resting (**Fig. 3m and Extended Data Fig. 7g-k**)). Danuglipron-treated mice on either diet displayed less grooming compared to vehicle-treated counterparts, likely due to reduced food intake naturally shortening the behavioral satiety sequence, which includes a grooming phase following feeding(*345*). Together, these findings demonstrate that GLP1RA treatments can realign the behavior of HFD-fed animals toward SD-fed norms (**Fig. 3n and Supplementary Video 1**), effectively neutralizing the behavioral hallmarks of hedonic feeding and reinforcing the notion that distinct neuronal activation patterns translate into meaningful, diet-dependent behavioral outcomes.

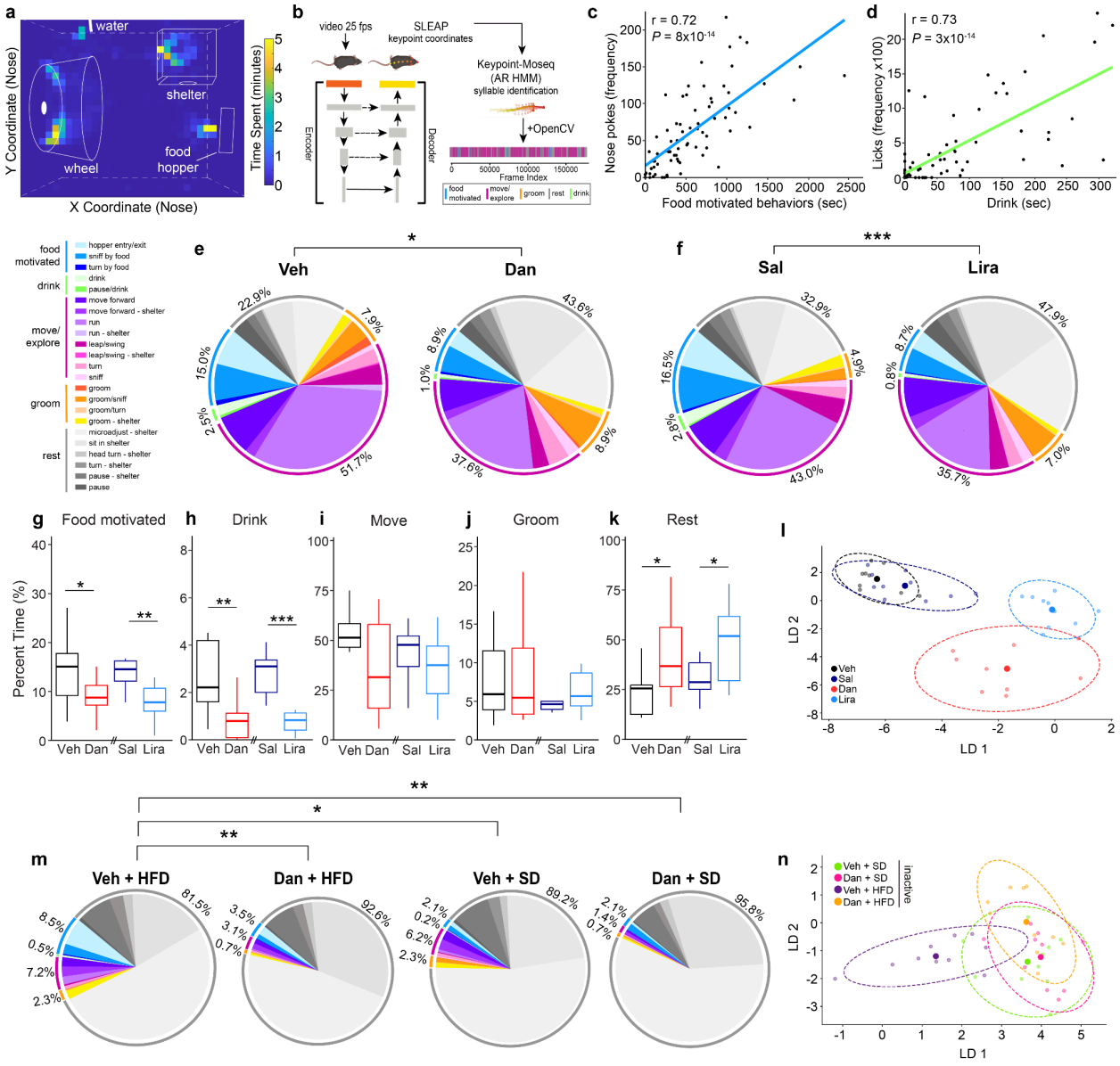

Figure 3: Machine-learning assisted behavior profiling reveals distinct phenotypes associated with GLP1RA and diet. a, **(Elizabeth Godschall, Isabelle Sajonia, Kaleigh West)** Representative heatmap of Glp1r^{S33W} mouse nose location and home cage setup. Color indicates time spent in minutes over 2 hours. **b, (Isabelle Sajonia)** Simplified pipeline for machine learning analysis of behavior(*343*, *344*). Analysis parameters: SLEAP tracking with 9 keypoints at 25 fps, Keypoint-MoSeq fit an autoregressive hidden Markov model (AR-HMM) to PCA-reduced keypoints. A full model was then trained, producing 91 behavioral syllables with a minimum frequency threshold of ≥0.01%. Trained raters manually named behaviors, incorporating locational context via OpenCV. **c,d**, **(Isabelle Sajonia)** Correlation between sensor data and video analysis across all conditions tested for (**c**) food hopper nose pokes and food motivated behaviors and (**d**) water bottle spout licks and drinking (*n* = 78, Pearson regression, ***P<0.0001). **e,f**, **(Isabelle Sajonia)** Proportion of time spent performing each of

the 23 behaviors identified using Keypoint-MoSeq and averaged across all mice per condition, binned into 5 behavior categories. A MANOVA was run on the PCA of the proportion of time spent performing each behavioral category. PCA was ran for (**e**) Veh and Dan and (**f**) Saline and Lira (*n* = 9 Veh/Dan, *n* = 10 Sal/ Lira, RM MANOVA with resampling MATS, **P*<0.05, ****P*<0.001). **g-k**, **(Isabelle Sajonia)** Percentage of time spent (**g**) food seeking, (**h**) drinking, (**i**) moving/exploring, (**j**) grooming, and (**k**) resting. (*n* = 9 Veh/Dan, *n* = 10 Sal/Lira, generalized linear mixed-effects model with beta regression, **P*<0.05, ***P*<0.01, ****P*<0.001). **l, (Isabelle Sajonia)** Linear discriminant analysis (LDA) plot of the similarity between mean behavioral summaries of mice per condition. Opaque centroid circles represent the mean behavioral summaries per condition, small circles indicate the specific embedding locations of individual mice within each condition, and ellipses denote two standard deviations from the mean for each group. **m, (Isabelle Sajonia)** Proportion of time spent performing each of the 23 behaviors, and 5 larger behavioral categories in SD- and HFD-fed mice during the light cycle after vehicle or danuglipron. MANOVA was run on PCA of the 23 behavior durations (*n* = 10, RM MANOVA with resampling MATS and holm correction, **P*<0.05, ***P*<0.01). **n, (Isabelle Sajonia)** LDA plot of the similarity between mean behavioral summaries of mice per condition. Data are represented as medians ± Q1-Q3. **P*<0.05; ***P*<0.01; ****P*<0.001.

C3.2.5 Danuglipron Activates Hypothalamic and Hindbrain GLP1R Circuits

To distinguish direct from indirect effects of small-molecule GLP1RAs in specific brain regions, we developed a Cre-dependent adeno-associated virus (AAV) vector expressing full-length human GLP1R (AAV-hSyn-DIO-hGLP1R) (**Fig. 4a**). When applied in Glp1r-IRES-Cre mice, this approach enables selective expression of hGLP1R in Glp1r-positive cells, allowing us to isolate direct activation effects from secondary circuit responses. In Glp1r-Cre mice conditionally expressing hGLP1R in their basomedial hypothalamus (BMH-hGLP1R) (**Extended Data Fig. 8a,b**), danuglipron significantly decreased active-phase SD intake without affecting inactive-phase HFD consumption (**Fig. 4c,h**) while control mice expressing mCherry in the same region showed no changes in consumption (**Fig. 4b,g**). When targeting the DMH, a BMH subnucleus recently implicated in encoding satiation(*310*, *335*, *346*), we found similar selective effects on SD intake (**Fig. 4d,i and Extended Data Fig. 8c,d**). Targeting the hindbrain NTS/AP

complex resulted in decreased consumption of both SD and HFD (**Fig. 4e,j and Extended Data Fig. 8e,f**), aligning with recent findings on hindbrain Glp1R circuits in aversion and satiety(*309*).

C3.2.6 Danuglipron Directly Activates CeA^{Glp1r} Neurons to Regulate Hedonic Feeding

Recognizing the limited understanding of the CeA's role in GLP1RA responses(*337*), we focused our investigation on Glp1r-positive neurons in this region (CeA^{Glp1r}). First, we confirmed CeA^{Glp1r} neurons that conditionally express hGLP1R directly respond to small-molecule GLP1RAs by co-injecting AAV-hSyn-DIO-hGLP1R and AAV-DIO-eYFP into the CeA of Glp1r-Cre mice and performing whole-cell patch-clamp recordings (**Extended Data Fig. 9c-f**). We measured the resting membrane potential of hGLP1R-expressing neurons before and after infusion of 10 μM danuglipron (**Extended Data Fig. 9a**). Consistent with activation of the G_s/cAMP pathway via hGLP1R(*347*, *348*), danuglipron elicited significant membrane depolarization, confirming functional expression (**Extended Data Fig. 9b**). Next, to determine whether this responsiveness translates into changes in feeding behavior, we assessed Glp1r-Cre mice conditionally expressing hGLP1R in the CeA (CeA-hGLP1R) under both SD and HFD conditions. Remarkably, CeA-hGLP1R mice showed a selective reduction in inactive-phase HFD consumption after Danuglipron injection without any effect on active-phase SD intake (**Fig. 4f,k and Extended Data Fig. 8g,h**). We corroborated these findings with an alternative virus expressing the small molecule-sensitive mouse SNP, Glp1r^{S33W} and its wildtype control (AAV-DIO-mGlp1r^{S33W} and AAV-DIO-mGlp1r) (**Extended Data Fig. 10a,d**). These results demonstrate that CeA^{Glp1R} neurons selectively modulate hedonic feeding in response to small-molecule GLP1RAs (**Extended Data Fig. 10b,c**), revealing a previously uncharacterized neural substrate for GLP1RA-mediated regulation of feeding behavior.

The relatively small molecular mass of danuglipron (555.6 Da) and its robust effects in CeA-hGLP1R mice suggest this compound can access brain structures beyond the circumventricular organs (CVOs). Although the extent of brain penetration by different GLP1RAs remains an open question(*305*, *334*, *349*, *350*), definitively establishing their direct engagement of deep nuclear structures is critical for understanding their mechanisms of action. To test whether danuglipron can directly induce neuronal activity in the CeA, we expressed GCaMP7s along with either hGLP1R or mGlp1r in the CeA of Glp1r-Cre mice and recorded calcium transients via fiber photometry *in vivo* (**Fig. 4l and Extended Data Fig. 11a-d**). Since previous work showed peptide-based GLP1RAs induce cFos expression in the CeA of wildtype mice(*305*)[,(334),(338, 339)]—though whether through direct or indirect pathways remains unclear—we first used liraglutide as a positive control and confirmed it elicited significant calcium transients in CeA-hGLP1R mice (**Extended Data Fig. 11e,f**). Importantly, danuglipron treatment also elicited robust increases in calcium transients in CeA-hGLP1R mice, a response that was absent in mGlp1r-expressing negative controls (**Fig. 4m–p**). These findings provide direct evidence that danuglipron penetrates beyond the CVOs to functionally engage CeA neurons expressing human GLP1R.

Next, we sought to establish the physiological role of CeA^{Glp1R} neurons in hedonic feeding by optogenetically stimulating them independently of any pharmacological agonists and observed reduced HFD consumption (**Fig. 4q-r**), mirroring the inhibitory feeding effects observed in response to danuglipron in CeA-hGLP1R mice (**Fig. 4k and Extended Data Fig. 10b,c**). To determine whether the CeA is essential for the inhibitory effects of GLP1RAs on feeding, we selectively knocked out Glp1r in the CeA by bilaterally injecting AAV-Cre or AAV-GFP into the CeA of $Glp1r^{flox/flox}$ mice (**Fig. 4s**). Although the loss of CeA Glp1R signaling had no impact on SD intake, it significantly increased HFD consumption following liraglutide injection (**Fig. 4t**). These results pinpoint CeA^{Glp1R} neurons as a critical node in the GLP1RA-responsive circuitry

specifically regulating reward-driven feeding behaviors. To further clarify the physiological relevance of this circuit, we asked whether CeA^{Glp1R} neurons receive endogenous GLP-1 input. By expressing synaptophysin in NTS Gcg-Cre neurons, we detected Gcg-positive fibers and synaptic terminals in the CeA (**Fig. 4u**). This demonstrates that CeA^{Glp1R} neurons not only respond to exogenous agonists, but also can receive endogenous GLP-1 signals from the NTS. Together, these findings underscore the CeA as a key integrative hub where GLP-1 signaling—both pharmacologically induced and naturally occurring—converges to curb hedonic feeding(*351*).

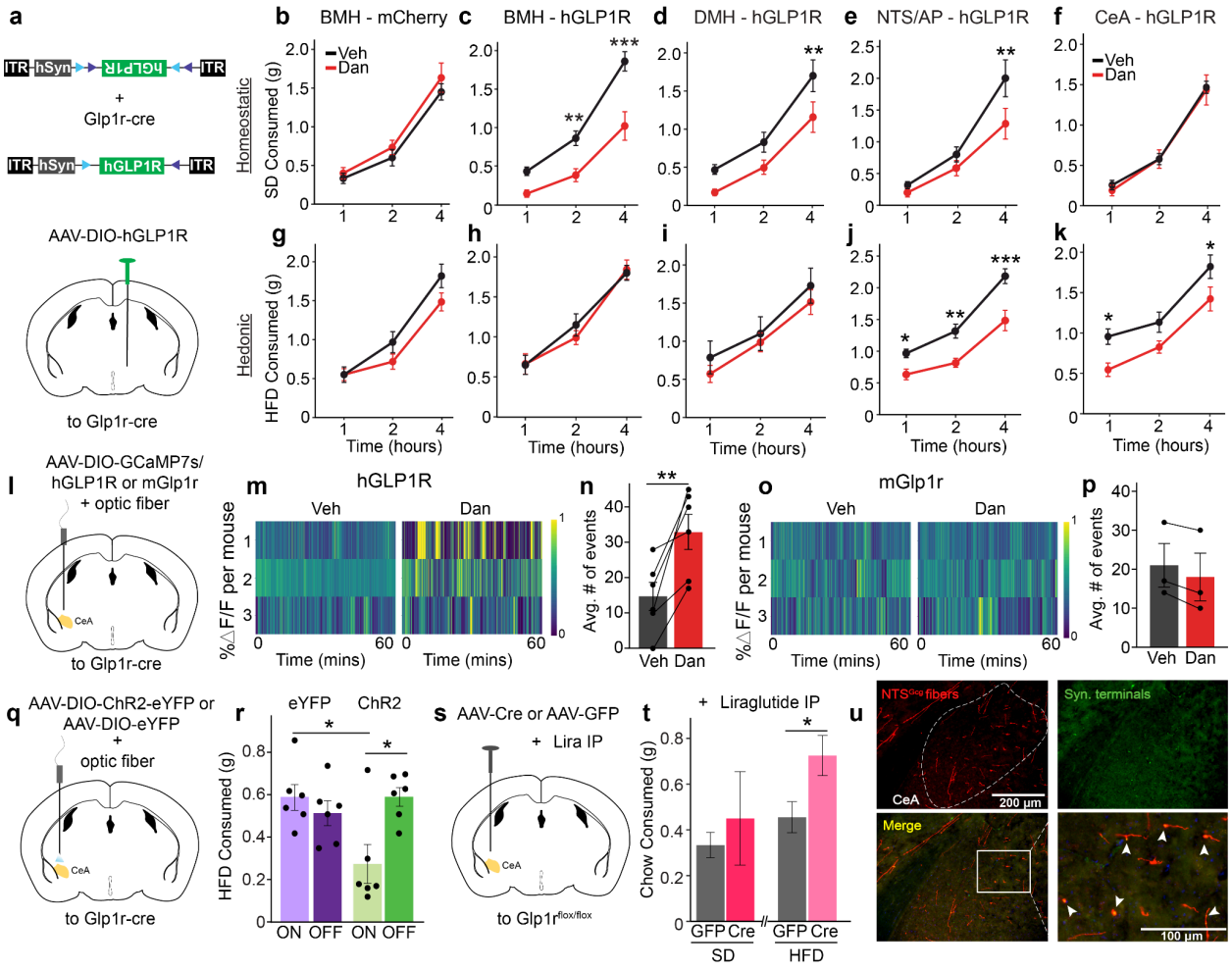

Figure 4: Central amygdala GLP1R activation inhibits hedonic food intake via direct activation by danuglipron. a, (Tony Spano, Elizabeth Godschall) Representative schematic

of AAV-DIO-hGLP1R viral construct and injection into the basomedial hypothalamus (BMH). **b-k**, 1, 2, and 4-hour SD or HFD consumption after vehicle (Veh) or danuglipron (Dan) in Glp1r-Cre mice expressing (**b,g**) **(Elizabeth Godschall)** AAV-DIO-mCherry (BMH-mCherry, *n* = 6) or (**c,h**) **(Elizabeth Godschall, Addison Webster)** AAV-DIO-hGLP1R (BMH-hGLP1R, *n* = 10) in the BMH, (**d,i**) **(Elizabeth Godschall, Bugra Gungul)** DMH (*n* = 7), (**e,j**) **(Elizabeth Godschall, Nicholas Conley)** NTS/AP (*n* = 6), or (**f,k**) **(Elizabeth Godschall, Bugra Gungul)** CeA (*n* = 9) (two-way ANOVA with Bonferroni correction, **P*<0.05; ***P*<0.01; ****P*<0.001). **l, (Elizabeth Godschall)** Schematic of AAV-DIO-GCaMP7s + AAV-DIO-hGLP1R or mGLP1R injection with a fiber optic implant to the CeA of Glp1r-Cre mice. **m-p, (Bugra Gungul, Isabelle Sajonia)** Representative heatmaps of %ΔF/F neuronal calcium signal per mouse during 1-hour of fiber photometry recording after vehicle or danuglipron injection in (**m**) hGLP1R or (**o**) mGLP1R expressing mice. Number of significant calcium events averaged per mouse during 1-hour recording session following vehicle or danuglipron in (**n**) hGLP1R or (**p**) mGLP1R expressing mice (*n* = 3-6 per injection, paired t-test, ***P*<0.01 and Wilcoxon signed-rank test). **q, (Elizabeth Godschall)** Schematic of AAV-DIO-eYFP or AAV-DIO-ChR2-eYFP injection with a fiber optic implant to the CeA of Glp1r-Cre mice. **r, (Bugra Gungul)** 30-minute HFD consumption in ChR2 and eYFP expressing controls after 20 Hz blue light stimulation (ON) or no stimulation (OFF) (*n* = 6 per group, two-way ANOVA with Tukey's HSD correction, **P*<0.05). **s**, **(Elizabeth Godschall)** Schematic of AAV-Cre to conditionally knockout Glp1r, or AAV-GFP control injection to the CeA of $Glp1r^{flox/flox}$ mice. **t**, **(Elizabeth Godschall)** SD (left) and HFD (right) consumption 4 hours after injection of liraglutide in AAV-Cre or AAV-GFP expressing mice. (*n* = 6, Welch's t-test, **P*<0.05). **u**, **(Elizabeth Godschall, Bugra Gungul)** Representative images of the CeA from Gcg-Cre mice injected with AAV-DIO-mGFP-2A-Synaptophysin-mRuby in the NTS; scale bar = 200 μm. NTS^{GCG} fibers (red; pseudo-colored mGFP; top left), synaptic terminals (green; pseudo-colored mRuby; top right) are shown, with a magnified view (bottom right; scale bar = 100 μm). Data are represented as means ± SEM. **P*<0.05; ***P*<0.01; ****P*<0.001.

C3.2.7 Small-Molecule GLP1RAs Engage CeA to Modulate Mesolimbic Dopamine Release in Response to HFD

Given the selective role of CeA^{Glp1R} neurons in hedonic feeding regulation, we investigated their connectivity to mesolimbic reward circuitry. Anatomical tracing in Glp1r-Cre mice, using AAV-DIO-Synaptophysin or AAV-DIO-eYFP, revealed pronounced projections from CeA-GLP1R neurons to the ventral tegmental area (VTA) (**Fig. 5a and Extended Data Fig. 12a-e**). These findings support a model in which NTS^{Gcg} neurons drive CeA^{Glp1R} activity, which in turn influences VTA neurons and ultimately the nucleus accumbens (NAc) (**Fig. 5b**). Based on our observations that CeA^{Glp1R} activation suppresses hedonic feeding while receptor ablation

negates this effect, we hypothesized that these neurons modulate VTA dopaminergic output to reduce NAc dopamine signaling during reward-driven feeding.

To test this hypothesis, we first examined whether GLP1RAs broadly affect dopamine responses in the NAc. By expressing AAV-dLight1.3b in Glp1r^{S33W} mice, we monitored dopamine responses to HFD following peptide (liraglutide) or small-molecule (danuglipron, orforglipron) GLP1RA administration (**Fig. 5c**). Strikingly, all three compounds significantly diminished both the peak and consumption-associated dopamine response (**Fig. 5d–i and Extended Data Fig. 13a-c**), indicating that despite their pharmacological differences, these agents converge on a common central mechanism to reduce dopamine-mediated reward.

To establish a causal link between CeA^{Glp1R} neuron activity and mesolimbic dopamine output, we selectively expressed hGLP1R in the CeA of Glp1r-Cre mice and monitored NAc dopamine dynamics during HFD consumption following danuglipron or orforglipron administration (**Fig. 5j and Extended Data Fig. 12f-h**). Remarkably, both treatments substantially blunted the peak and consumption-associated dopamine responses (**Fig. 5k–p**). This finding demonstrates that activation of GABAergic CeA^{Glp1R} neurons(*337*) inhibits reward-driven dopamine signaling. By establishing that the CeA-VTA-NAc axis operates in parallel with previously characterized hindbrain to midbrain Glp1R circuits(*352*–*354*), our findings reveal a distributed network of Glp1R-expressing neurons orchestrating the suppression of food consumption(*309*, *310*, *355*, *356*, *357*–*359*).

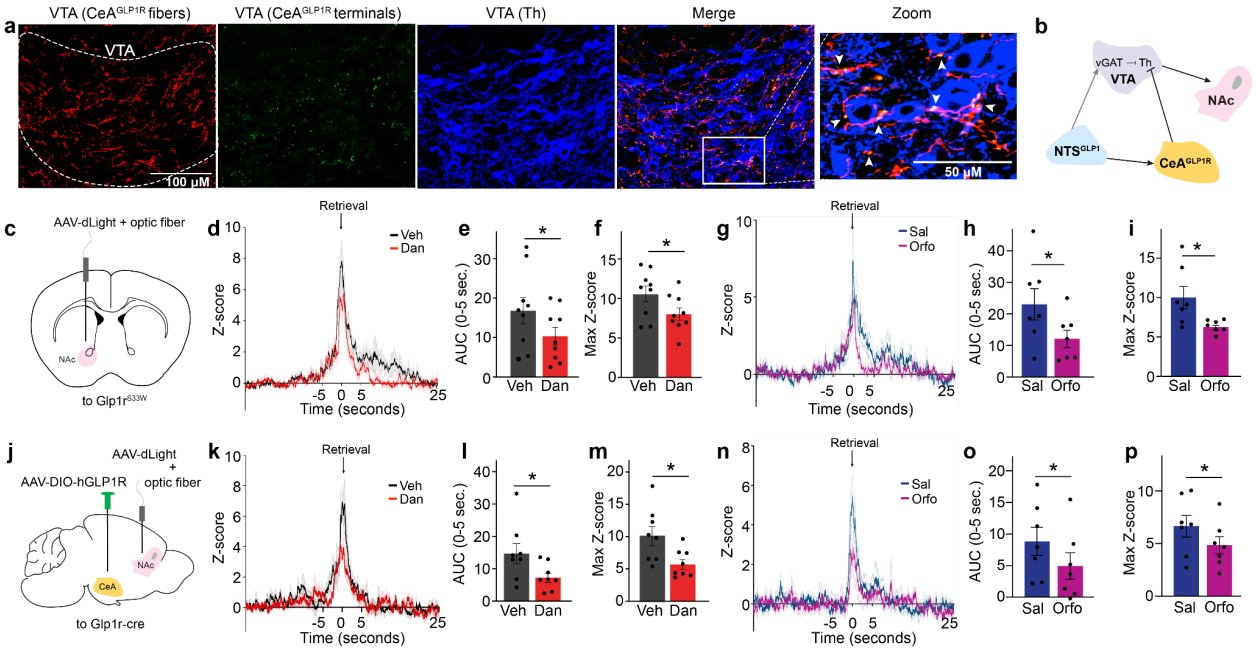

Figure 5: CeA^{GLP1R} neurons project to the VTA to modulate dopamine output to the NAc in response to HFD. a, **(Elizabeth Godschall, Bugra Gungul)** Representative image of the VTA from Glp1r-Cre mice injected with AAV-DIO- mGFP-2A-Synaptophysin-mRuby in the CeA; scale bar = 100 µm. CeA^{GLP1R} fibers (red; pseudo-colored mGFP), synaptic terminals (green; pseudo-colored mRuby), and tyrosine hydroxylase-positive neurons (Th; blue, marking dopaminergic neurons) are shown, with a magnified view (right; scale bar = 50 µm). **b**, **(Elizabeth Godschall)** Schematic of proposed neural circuit from NTS → CeA → VTA → NAc. Arrows indicate neuron activation, blunted ends indicate neuron inhibition. Gray arrow from NTS → VTA indicates a known connection from NTS^{GLP-1} to VTA^{vGAT} neurons(*354*). **c**, **(Elizabeth Godschall)** Schematic of genetically-encoded dopamine sensor, AAV-dLight1.3b, injection and fiber optic implant in the NAc of Glp1r^{S33W} mice. **d,g**, **(Bugra Gungul)** Averaged Z-score traces showing dopamine release in the NAc in response to HFD following administration of (**d**) vehicle or danuglipron and (**g**) saline or orforglipron in Glp1r^{S33W} mice. Traces are aligned to food retrieval time (t = 0) and averaged across five food trials per mouse. **e-i**, **(Bugra Gungul, Sophia Ogilvie, Elizabeth Godschall)** Quantified (**e,h**) area under the curve (AUC) for Z-scores and (**f,i**) maximum fluorescence Z-scores within the food retrieval window (*n* = 9 for danuglipron, *n* = 7 for orforglipron, paired t-test, **P*<0.05). **j**, **(Elizabeth Godschall)** Schematic of AAV-dLight1.3b injection and fiber optic implant into the NAc and AAV-DIO-hGLP1R injection into the CeA of Glp1r-Cre mice. **k,n**, **(Bugra Gungul)** Averaged Z-score traces showing dopamine release in the NAc in response to HFD following administration of (**k**) vehicle or danuglipron and (**n**) saline or orforglipron in CeA-hGLP1R mice. Traces are aligned to food retrieval time (t = 0) and averaged across five food trials per mouse. **l-p**, **(Bugra Gungul, Sophia Ogilvie)** Quantification of (**l,o**) AUC for Z-scores and (**m,p**) maximum fluorescence Z-scores within the food retrieval window (*n* = 8 for danuglipron, *n* = 7 for orforglipron, paired t-test, **P*<0.05). Data are represented as means ± SEM. **P*<0.05; ***P*<0.01; ****P*<0.001.

C3.3 Discussion

Our findings identify a previously unrecognized amygdalar circuit through which next-generation GLP1RAs modulate reward-driven feeding. In particular, our data indicate that CeA^{Glp1R} neurons receive GLP-1 input from the NTS and influence VTA activity, thereby providing a framework for integrating metabolic signals into dopamine-dependent reward circuits(*299*, *352*, *357*–*359*). This insight aligns with an expanding body of evidence that GLP1RAs influence motivational and reward-related processes, raising the possibility of their therapeutic potential for disorders characterized by dysregulated reward, such as substance use(*301*, *302*, *303*, *332*, *360*, *361*). Looking ahead, our findings raise critical questions about the broader impact of chronic GLP1RA treatment on reward processing. With small-molecule GLP1RAs like orforglipron—described as 'a product for the masses' (*317*)—gaining traction as accessible, scalable therapies, understanding their long-term effects on brain function becomes essential.

C3.4 Methods

Mouse lines

All experiments were carried out in compliance with the Association for Assessment of Laboratory Animal Care policies and approved by the University of Virginia Animal Care and Use Committee. Mice were housed on a 12:12-hour light/dark (LD) cycle with food (PicoLab Rodent Diet 5053) and water *ad libitum* unless otherwise indicated. For experiments, we used 8-week or older male and female C57BL6/J mice, Glp1r-IRES-Cre mice with IRES-Cre inserted in-frame 3 base pairs downstream of Glp1r stop codon (Glp1rtm1.1(cre)Lbrl/RcngJ, strain #029283, RRID:IMSR_JAX:029283), Glp1r-IRES-Cre mice crossed to Ai14 tdTomato reporter line (B6.Cg-Gt(ROSA)26Sortm14(CAG-tdTomato)Hze/J, strain #007914, RRID: IMSR_JAX:007914), $Glp1r^{flox/flox}$ mice (B6(SJL)-Glp1rtm1.1Stof/J, strain #035238, RRID: IMSR_JAX:035238), Gcg-Cre mice (C57BL/6J-Tg(Gcg-cre)-1Mmsc/Mmmh, stock #051056-MU,

RRID:MMRRC_051056-MU) and Glp1r^{S33W} mice (described below). Gcg-Cre mice were rederived by *in vitro* fertilization from frozen sperm (MMRRC, stock no. 051056-MU).

Generation of Glp1r^{S33W} mouse

The Glp1r^{S33W} mouse line was created with CRISPR-Cas9 homologous repair at the University of Virginia Genetically Engineered Murine Model Core. Briefly, Cas-9 (Alt-R™ S.p. Cas9 Nuclease V3, 100 µg, catalog no. 1081058), Alt-R™ HDR Donor Oligo repair template (below), tracrRNA (Alt-R® CRISPR-Cas9 tracrRNA, 5 nmol, catalog no. 1072532), and CRISPR-Cas9 crRNA XT (ATTTCTGCACCGTCTCTGAG) were microinjected into a fertilized B6SJL zygote and were implanted into a pseudopregnant female. Founder pups were genotyped as described below and backcrossed to C57BL6/J mice for at least 4 generations before experimentation.

Repair Template

aagagggtgggagtccagtgggaccagaggggctgctggagccacggggcttctgcttttatttctgctttcccttgtagGGTACCA CGGTG**TCGCTCTGGGAAACCGTCCAAAAGTGG**AGAGAATACCGGCGGCAGTGCCAGCGT TTCCTCACGGAAGCGCCACTCCTGGCCACAGgtgcgtccagatgaggcctcacg

Validating Glp1r^{S33W} mice

Tail snips were obtained from pups at 3 weeks of age. DNA was extracted with an extraction buffer (Sigma, catalog no. E7526) and tissue prep solution (Sigma, catalog no. T3073), heated for 10 and 3 minutes at 55°C and 100°C, respectively, then neutralized with a neutralization solution (Sigma, catalog no. N3910). PrimeSTAR High Fidelity PCR (Takara, catalog no. R050A) was performed with 1uL of cDNA and 10uM of 5′-3′ F (GATCCCCAAAGTGGCAGTCA) and 5′-3′ R (AGCTATGGACTGGGGATCGT) primers. After amplification, the PCR product was run on a 1.2% agarose gel and bands were cut out at 330 bp. DNA was gel extracted and purified (Qiagen, catalog no. 28704), mixed with 5uM right primer, H_2O, and subsequently sent to be

analyzed via Sanger sequencing (Azenta). Chromatogram results were analyzed to assign wild type, heterozygous, or homozygous genotypes for each mouse.

Generation of GLP1R viruses

The full length human *Glp1r* gene was obtained by PCR, amplifying the human fragment from GLP1R-tango (plasmid from Addgene, #66295, RRID:Addgene_66295), including the leader sequence present in the GLP1R-tango. The primers used were: 5′-3′ F (AAAGCT-AGCGCCACCATGAAGACGATCATCGCCCTGAGC) and 5′-3′ R (TTTGGCGCGCCCTAA-GAGCAGGACGCCTGACAAGT), ligating the product into pAAV-hSyn-DIO-EGFP (plasmid from Addgene, #50457, RRID:Addgene_50457) in place of the EGFP in NheI and AscI sites to produce the human GLP1R virus construct (AAV-hSyn-DIO-hGLP1R). The full length mouse *Glp1r* wild type gene was synthesized by Twist Biosciences (USA), generating a NheI and AscI fragment. This construct included the same leader sequence present in the human construct, as well as an HA-tag encoded at the C-terminus of the full length mouse protein coding region. The fragment was inserted into pAAV-hSyn-DIO-EGFP (plasmid from Addgene, #50457, RRID:Addgene_50457) in place of EGFP to produce the plasmid construct (AAV-hSyn-DIO-mGLP1R-HA). The full length mouse *Glp1r* gene bearing a Ser to Trp mutation at position 33 (S33W) was made by inserting a synthetic NheI and StuI fragment prepared by Twist Biosciences, containing the single mutation within this fragment. This was cloned into the sites present in the wild type construct to produce the S33W mouse mutant, followed by an HA-tag encoded at the C-terminus (AAV-hSyn-DIO-mGLP1R^{S33W}-HA). Viral plasmid constructs were confirmed by Sanger sequencing. Virus plasmid constructs were prepared and sent to the University of North Carolina Viral Core (Chapel Hill, NC) for preparation of the AAV (serotype 8).

Stereotactic surgery

Mice were anesthetized with isoflurane (5% induction and 2 to 2.5% maintenance; Isothesia) and placed in a stereotaxic apparatus (AWD). A heating pad was used for the duration of the surgery to maintain body temperature, and ocular lubricant was applied to the eyes to prevent desiccation. A total of 200-400 nL was microinjected per side of [rAAV8/AAV2-hSyn-DIO-hGLP1R, plasmid from Addgene, virus packed at UNC GTC Vector Core, Lot #AV9862 (100 μL at titer ≥ 1.5 $\times 10^{13}$ vg/mL); AAV8-hSyn-DIO-mGLP1R^{S33W}-HA, synthesized by Twist Biosciences, virus packed at UNC GTC Vector Core, Lot #AV10104 (100 μL at titer ≥ 8.2×10^{12} vg/mL); AAV8-hSyn-DIO-mGLP1R-HA, synthesized by Twist Biosciences, virus packed at UNC GTC Vector Core, Lot #AV10103 (100 μL at titer ≥ 4.5×10^{12} vg/mL); pAAV9-syn-dLight1.3b, plasmid from Addgene, #135762, RRID:Addgene_135762, virus packed at UNC GTC Vector Core (100 μL at titer ≥ 1.5×10^{13} vg/mL); pAAV1-EF1a-DIO-hChR2(H134R)-EYFP-WPRE-HGHpA, plasmid from Addgene, #20298, RRID:Addgene_20298, virus packed at UNC GTC Vector Core (100 μL at titer ≥ 7×10^{12} vg/mL); pGP-AAV1-syn-DIO-jGCaMP7s-WPRE, plasmid from Addgene, #104491, RRID: Addgene_104491, virus packed at UNC GTC Vector Core (100 μL at titer ≥ 1×10^{13} vg/mL); pAAV1-Ef1a-DIO-EYFP, plasmid from Addgene, #27056, RRID:Addgene_27056, virus packed at UNC GTC Vector Core (100 μL at titer ≥ 1×10^{13} vg/mL); AAV8-hSyn-DIO-mCherry, plasmid from Addgene #50459, RRID:Addgene_50459, and virus packed at UNC Vector Core (100 μL at titer ≥ 7×10^{12} vg/mL); pAAV-hSyn-FLEx-mGFP-2A-Synaptophysin-mRuby, plasmid from Addgene, #71760, RRID:Addgene_71760, and virus packed at UNC Vector Core; pENN.AAV.hSyn.HI.eGFP-Cre.WPRE.SV40, plasmid from Addgene, #105540-AAV8, RRID:Addgene_105540-AAV8, and virus packed at UNC Vector Core (100 μL at titer ≥ 1×10^{13} vg/mL); pAAV-hSyn-EGFP, plasmid from Addgene, #50465-AAV8, RRID:Addgene_50465-AAV8, and virus packed at UNC Vector Core (100 μL at titer ≥ 7×10^{12} vg/mL)], plasmid was delivered using a glass pipette at a flow rate of 50 nl/min driven by a microsyringe pump controller (World

Precision Instruments, model Micro 4). The syringe needle was left in place for 10 min and was completely withdrawn 17 min after viral delivery. For *in vivo* calcium and dopamine imaging and optogenetics, a unilateral fiber optic cannula (RWD, Ceramic Ferrule, Ø400-μm, 0.5 numerical aperture) was implanted 0.2-mm dorsal to the viral injection coordinates following viral delivery and stabilized on the skull with dental cement (C&B METABOND, Parkell). Two weeks minimum were allowed for recovery and transgene expression after surgery. Stereotaxic coordinates relative to Bregma (George Paxinos and Keith B. J. Franklin): basomedial hypothalamus, mediolateral (ML): ±0.3 mm, anterior posterior (AP): −1.4 mm, dorsoventral (DV): −5.9 mm; DMH, ML: ±0.3 mm, AP: −1.8 mm, DV: −5.4 mm; CeA, ML: ±2.7 mm, AP: −1.3 mm, DV: −4.6 mm; VTA, ML: ±0.5 mm, AP: −3.6 mm, DV: −4.5 mm; NAc, ML: ±1.25 mm, AP: +1.0 mm, DV: −4.7 mm from Bregma; and NTS/AP, ML: ± 0.15 mm, AP: −0.3 mm, DV: −0.1, −0.4 mm from the Zero point of the calamus scriptorius. All surgical procedures were performed under sterile conditions and in accordance with University of Virginia Institutional Animal Care and Use Committee guidelines. Histological analysis was performed to validate the success of intracranial surgeries. Mice with unsuccessful viral/implant targeting were excluded.

GLP1R agonists

Liraglutide powder (Selleck, catalog no. S8256) was dissolved in 0.9% NaCl sterile saline, lightly sonicated, and further diluted in 0.9% NaCl sterile saline to 0.03mg/mL. Danuglipron powder (Selleck, catalog no. S9851) was dissolved to 30 mg/mL in 100% ethanol with gentle sonication, then diluted to 3mg/mL (food intake) or 0.3mg/mL (GTT) in vehicle [1N NaOH, 2% Tween 80, 5% polyethylene glycol (PEG) 400, 5% dextrose](*321*). Orforglipron powder (MedChemExpress, catalog no. HY-112185) was dissolved to 10mg/mL in Dimethyl sulfoxide (DMSO) and further diluted in 0.9% NaCl sterile saline to 0.1mg/mL.

Histological analysis and imaging

For fixed tissue collection, mice were deeply anesthetized (ketamine:xylazine, 280:80 mg/kg, intraperitoneally) and perfused intracardially with ice-cold 0.01M phosphate buffer solution (PBS), followed by fixative solution [4% paraformaldehyde (PFA) in PBS at a pH of 7.4]. For testing brain region cFos activation (Fig. 3), danuglipron (30 mg/kg), orforglipron (1 mg/kg), or liraglutide (0.3 mg/kg) was delivered via intraperitoneal injection or oral gavage 2 hours (or 6 hours for orforglipron) before perfusion and brain harvesting. After perfusion, brains were harvested and postfixed overnight at 4°C in PFA. Fixed brains were then transferred into 30% sucrose in PBS for 24 hours and then frozen on dry ice. Frozen brains were sectioned immediately or stored in −80°C for future processing. Coronal sections (30 μm) were collected with a cryostat (Microm HM 505 E). Sections were permeabilized with 0.3% Triton X-100 in PBS (PBS-T) and blocked with 3% normal donkey serum (Jackson ImmunoResearch, RRID:AB_2337258) in PBS-T (PBS-T DS) for 30 min at room temperature. Sections were then incubated overnight at room temperature in primary antibodies diluted in PBS-T DS. For visualization, sections were washed with PBS-T and incubated with appropriate secondary antibodies diluted in the PBS-T DS for 2 hours at room temperature. Sections were washed three times with PBS and mounted using DAPI Fluoromount-G (Southern Biotech, catalog no. 0100-20). Images were captured on a Zeiss Axioplan 2 Imaging microscope equipped with an AxioCam MRm camera using AxioVision 4.6 software (Zeiss) or confocal microscope imaging was performed on a Zeiss LSM 800 microscope (Carl Zeiss). The following primary antibodies were used for fluorescent labeling: anti-c-Fos (rabbit, 1:1000; Synaptic Systems, #226003, RRID:AB_2231974), anti-DsRed (rabbit, 1:1000; Takara Bio, catalog no. 632496, RRID:AB_10013483), anti-TdTomato (goat, 1:1000; Arigobio, catalog no. ARG55724), anti-hGLP1R (rabbit, 1:200; Invitrogen, catalog no. PA5-97789, RRID: AB_2812404), anti-HA (rabbit, 1:1000, Cell Signaling, catalog no. 3724), anti-Th (rabbit, 1:500; Chemicon, catalog no. AB152), and anti-GFP (goat, 1:500; Rockland, catalog no. 600-101-215). The secondary

antibodies (Jackson ImmunoResearch) used were Cy2-conjugated donkey anti-rabbit (1:250; catalog no. 711-225-152, RRID:AB_2340612), Cy3-conjugated donkey anti-rabbit (1:250; catalog no. 711-165-152, RRID:AB_2307443), Cy5-conjugated donkey anti-rabbit (1:250; catalog no. 711-175-152, RRID:AB_2340607), Cy3-conjugated donkey anti-goat (1:250; catalog no. 705-165-147, RRID:AB_2307351), and Alexa-Fluor® 488 donkey anti-goat (1:250; catalog no. 705-545-003, RRID:AB_2340428).

Antigen retrieval for hGLP1R staining

Antigen retrieval was performed before immunohistochemistry staining of human GLP1R, by incubating the sections in the following solutions sequentially in room temperature: 1% NaOH + 0.3% H_2O_2 in PBS for 20 min, 0.3% glycine in PBS for 10 min, and 0.03% sodium dodecyl sulfate (SDS) in PBS for 10 min. Then, antigen retrieval–treated sections were stained following the immunohistochemistry staining procedures described.

Fos analysis pipeline

Fos images were uploaded to ImageJ (FIJI) and cropped based on brain regions outlined in the Allen Brain Atlas. The area of the cropped regions were measured and recorded. Image thresholds were set per image and particles were analyzed within the size restriction of 50-500 pixels. cFos particles were analyzed per image, and total particles of each image were divided by total area of the image. At least three cFos images per region for each mouse was quantified and averaged per mouse and per genotype (WT or $Glp1r^{S33W}$). Ratios of NTS/AP Fos activation in $Glp1r^{S33W}$ mice were calculated by dividing Fos/area of NTS over AP for each mouse and averaged per injection.

Behavioral Assays

Metabolic analysis in comprehensive lab animal monitoring system

Indirect calorimetry in the comprehensive lab animal monitoring system (CLAMS, Columbus Instruments) was used to evaluate metabolic parameters of WT and Glp1r^{S33W} mice. All WT and Glp1r^{S33W} mice were single housed and maintained on a 12:12-hour LD cycle with *ad libitum* access to food (PicoLab Rodent Diet 5053) and water. Metabolic measures of respiratory exchange ratio and energy expenditure were averaged over 3 days per mouse and per genotype. (*n* = 10/11 mice per genotype). Averaged LD cycle and total 24 hour respiratory exchange ratio and energy expenditure was analyzed per genotype and per sex.

Glucose tolerance tests

WT or Glp1r^{S33W} mice were overnight fasted for 16 hours prior to experiment start (zeitgeber time [ZT] 10 - ZT2). Mice received a tail snip and blood glucose measure using a Glucometer (OneTouch Ultra Test Strips for Diabetes), along with injection or oral gavage of danuglipron (3mg/kg) or liraglutide (0.3mg/kg) 15 minutes prior to dextrose (D-glucose) injection, or orforglipron (1mg/kg) 240 minutes prior to dextrose. At time point 0, mice received a blood glucose measure and injection of dextrose (1g/kg). At 15, 30, 60, 90, and 120 minutes after injection, blood glucose levels were measured.

Homeostatic food intake

Home cages were changed and food was removed from the home cage 1 hour prior to experiment start. Mice were injected with vehicle/saline or drug (danuglipron 30mg/kg, liraglutide 0.3mg/kg, orforglipron 1mg/kg) at ZT11.5 (ZT8 for orforglipron) and two pellets of standard diet (PicoLab Rodent Diet 5053) were placed on the home cage floor at ZT12. Food intake measurements were taken at 1, 2, and 4 hours after ZT12 using infrared night vision goggles (Nightfox Swift Night Vision Goggles).

Hedonic food intake

Mice were habituated to high fat diet (HFD; Open Source, D12451; 4.73 kcal/gram; 45% fat, 20% protein, 35% carbohydrates; 17% sucrose) for 1 hour over two days before testing days. Standard diet was removed from the home cage 1 hour prior to experiment start. Mice were injected with vehicle/saline or drug (danuglipron 30mg/kg, liraglutide 0.3mg/kg, orforglipron 1mg/kg) at ZT1.5 and one pellet of HFD was placed on the home cage floor at ZT2 (ZT5.5 for orforglipron). Food intake measurements were taken at 1, 2, and 4 hours after HFD delivery. The same parameters were used in oral gavage experiments with danuglipron and orforglipron

Optogenetic Food Intake Analysis

Mice were single-housed for at least five days and habituated to a fiber optic cable and high fat diet for one hour over two days. On the test day, home cages were changed and food was removed 1 hour prior to the start of the experiment. During the test day, a pre-measured pellet of high-fat diet (HFD) was provided to each mouse. The test paradigm was 30 minutes of laser stimulation followed by 30 minutes without laser stimulation. Food intake during each 30-minute interval was measured. The laser stimulation protocol was 20 Hz, 473 nm blue light with a 2-second on and 3-second off pattern. The light power exiting the fiber optic cable, measured using an optical power meter (Thorlabs), was maintained at 7-8 mW across all experiments. Experiment performed during the light phase, between ZT3-ZT4. Mice with missed virus injection or off-target fiber placement were excluded from analysis.

Weight loss experiment

Male $Glp1r^{S33W}$ mice >8 weeks old were placed on a high fat diet (Open Source, D12451; 4.73 kcal/gram; 45% fat, 20% protein, 35% carbohydrates; 17% sucrose) for at least 8 weeks prior to experiment start. Mice that did not gain at least 20% of their baseline body weight were excluded from testing. Mice were randomly assigned to saline or orforglipron (1mg/kg) injection

groups and retested with the opposite treatment after a week of rest. Glp1r^{S33W} mice were injected daily at ZT6 and food and body weight were measured.

Home cage monitoring of Glp1r^{S33W} mice

Mice were singly housed and acclimated to home cage PhenoTyper boxes (Noldus, Netherlands) for 5 days prior to testing. The cages were maintained on a 12:12-hour light-dark (LD) cycle. During the acclimation period, mice had *ad libitum* access to standard diet (SD) provided in a food hopper, along with water bottles, running wheels, shelters, and bedding. Mice that failed to meet a baseline threshold of food hopper activity (<50 nose pokes from ZT 12-14) after habituation were excluded from the study to ensure sufficient engagement with the feeding setup. Of the 38 mice tested, 9 did not meet this criterion and were excluded. For the light cycle experiment, mice were additionally habituated to high-fat diet (HFD) for 2 days prior to testing. For testing, danuglipron (30 mg/kg) or vehicle was administered at ZT 11.5, with the injection order counterbalanced. Liraglutide (0.3 mg/kg) or saline was administered at ZT 10. Behavior was monitored for 4 hours starting at ZT 12. In the light cycle experiment, Danuglipron (30 mg/kg) or vehicle was administered at ZT 2.5, and behavior was recorded for 4 hours starting at ZT 3. During the 4-hour testing window, mice had *ad libitum* access to either SD or HFD, depending on the test condition. On HFD test days, HFD was replaced with SD immediately after the recording period. Danuglipron was not administered on consecutive days. Sensors in the PhenoTyper cages recorded the following metrics: food hopper head entries, water bottle spout licks, and full running wheel rotations. Behavioral sessions were recorded with top-down infrared cameras (Noldus) at a resolution of 960 x 540 pixels at 25 frames per second, in grayscale. Videos were cropped to 2-hour segments using Adobe Premiere Pro and re-encoded with H.264 compression via FFmpeg to ensure smooth playback and frame-seeking.

Machine-learning assisted pipeline

Animal pose estimation was performed on home cage monitoring videos of singly housed, free roaming mice with Social LEAP Estimates Animal Poses (SLEAP, v1.3.3)(*343*, *344*). The following 9 keypoints were tracked: nose, left ear, right ear, center 1-5, and tail base. We labeled 10,770 frames from 18 videos under conditions similar to the experimental ones, splitting them into 9,693 training and 1,077 validation frames (90% split). We used a U-Net based neural network with a max stride of 32, 16 filters, and a rotation angle of ± 180. All other hyperparameters were default using the single animal pipeline. The trained model's average distance (ground truth vs prediction) was: 1.59 pixels, mean object keypoint similarity (OKS): 0.85, mean average precision (mAP): 0.81, and mean average recall (mAR): 0.84. Inferences were made on the first two hours of videos (ZT 12-14), as this period was significant in the sensor data. Flow tracking and default hyperparameters were used for inference. Representative heatmaps of the mouse nose keypoint were generated in Python by cropping to remove the walls of the cage and creating 62 by 27 pixel bins.

Keypoint Motion Sequencing (Keypoint-MoSeq)(*343*, *344*) was then used to identify behavioral syllables using a probabilistic model from the input keypoint coordinates of 80 hours of home cage videos. Four latent dimensions accounted for 90% of the variance in aligned and centered keypoint coordinates. A kappa of 10^5 was chosen to maintain the desired syllable time-scale. Using this parameter, an autoregressive hidden Markov model (AR-HMM) was first fit to the data, followed by the full model fit. Keypoint-MoSeq identified 91 behavioral syllables; 46 accounted for ≥ 0.5% of instances, while those with frequencies < 0.5% but ≥ 0.01% were included, and < 0.01% were excluded.

To provide biologically meaningful interpretations, the syllables were grouped into broader behavioral categories (Fig. S6) by two trained raters. Some syllables represented a combination

of behaviors or closely related actions that could not be distinguished due to the camera angle (e.g., "groom/sniff"). Poor-quality syllables (~1% of the dataset), likely from keypoint tracking issues under the wheel, were excluded from analysis.

To incorporate location context, the pixel coordinates of the food hopper, shelter, and water bottle spout were defined in videos using the Python OpenCV package (OpenCV, 2024). Regions of interest (ROIs) were established around these coordinates. SLEAP coordinates identified when the mouse entered a specific ROI, with the nose keypoint for the food hopper and water bottle spout, and center 3 for the shelter. Behaviors were categorized based on location, such as distinguishing "sniff by food" from "sniff" outside the food hopper ROI.

This categorization resulted in 23 unique behaviors, which were further grouped into five general categories: “move/explore,” “rest,” “groom,” “food-motivated behaviors,” and “drink.” On average, these behaviors accounted for 98.3% of the total time in the two-hour video recordings for each video (mouse × condition). For each video, we calculated the total time spent performing each of the 23 behaviors. Additionally, the proportion of time each mouse spent on the five general behavior categories was calculated relative to their total behavioral time.

Proportional differences were assessed using a beta-distributed generalized linear mixed-effects model with mouse as a random effect. For the inactive phase, the model included main effects of drug and diet and their interaction. Behavioral collinearity was addressed with PCA, and the top three principal components (PC 1–3) were analyzed via repeated measures MANOVA.

To reveal global differences in behavior by condition, linear discriminant analysis (LDA) with three components was applied to the behavior duration dataset. LDA identified the linear combinations of behavioral features that best separated conditions. Separate plots were generated for dark and light cycle conditions, using the same LDA model fit across all tested conditions. Groups were also visualized in PC space (PC 1 and PC 2) as used in the MANOVA

analysis. LDA was performed using the scikit-learn package(*362*, *363*). All Python code for these analyses is available on GitHub.

Electrophysiology recordings

Brain slice preparation

Preparation of acute brain slices for patch-clamp electrophysiology experiments was modified from standard protocols previously described(*364*)[,(365),(366)]. Mice were anesthetized with isoflurane and decapitated. The brains were rapidly removed and kept in chilled artificial cerebrospinal fluid (ACSF) (0°C) containing (in mM): 125 NaCl, 2.5 KCl, 1.25 NaH_2PO_4, 2 $CaCl_2$, 1 $MgCl_2$, 0.5 L-ascorbic acid, 10 glucose, 25 $NaHCO_3$, and 2 Na-pyruvate (osmolarity 310 mOsm). Slices were continuously oxygenated with 95% O2 and 5% CO2 throughout the preparation. Coronal brain sections, 300 µm, were prepared using a Leica Microsystems VT1200 vibratome. Slices were collected and placed in ACSF warmed to 37°C for 30 minutes and then kept at room temperature for up to 5 hours.

Recordings

Brain slices were placed in a chamber superfused (~2 mL/min) with continuously oxygenated ACSF solution warmed to 32 ± 1°C. hGLP1R-expressing Central amygdala neurons were identified by video microscopy based on the expression of eYFP marker. Whole-cell electrophysiology recordings were performed using a Multiclamp 700B amplifier with signals digitized by a Digidata 1550B digitizer. Currents were amplified, lowpass-filtered at 2 kHz, and sampled at 35 kHz. Borosilicate electrodes were fabricated using a Brown-Flaming puller (model P1000, Sutter Instruments) to have pipette resistances between 2.5 and 4.5 mΩ. Current-clamp recordings of membrane potentials were collected in ACSF solution identical to that used for preparation of brain slices. The internal solution contained the following (in mM): 120 K-gluconate, 10 NaCl, 2 $MgCl_2$, 0.5 K_2EGTA, 10 HEPES, 4 Na_2ATP, and 0.3 NaGTP, pH 7.2 (osmolarity 290 mOsm). Resting membrane potential was recorded as previously described

(1,2). After 5 mins of baseline membrane potential recordings 10 μm of danuglipron was perfused for 5 mins followed by washout.

Statistics

Electrophysiology recordings were analyzed using ClampFit 11.2. All statistical comparisons were made using the appropriate test in GraphPad Prism 9.5.0. For membrane, AP properties, and amplitude underwent descriptive statistics followed by normality and lognormality test using gaussian distribution. Data were assessed for normality using the D'Agostino-Pearson omnibus normality test, Anderson-Darling test, Shapiro-Wilk test, and Kolmogorov-Smirnov test with Dallal-Wilkinson-Lillie for P-values. Data were tested for outliers using the ROUT method, and statistical outliers were not included in data analysis. Followed by Tukey's test with no gaussian distribution creating a nonparametric t-test using Wilcoxon matched-pairs signed rank test to compare responses caused by the drug. Data are presented as individual data points and/or mean ± SEM.

Fiber Photometry Recordings

***In vivo* calcium recording (GCaMP)**

Mice underwent 20-minute daily habituation sessions over two consecutive days to acclimate to the fiber-optic cable (Doric Lenses, Ø400-μm core, 0.57 numerical aperture). On the test day, mice were injected with either vehicle, saline, danuglipron (30 mg/kg) or liraglutide (0.3 mg/kg) two hours prior to recording. The order of injections was randomized to avoid order effects. Following the two-hour post-injection period, mice were connected to patch cables which were interfaced with rotary joints to enable free movement. Recordings were conducted for one hour. Fiber photometry data were recorded using fluorescent signals from both calcium-dependent (465 nm) and calcium-independent isosbestic (405 nm) excitation wavelengths (Doric). The isosbestic (405 nm) signal served to control for artifacts. The light power of the fiber optic cable

was measured before each experiment and maintained at approximately 20-30 µW for both the calcium-independent isosbestic (405 nm) and calcium-dependent (465 nm) signals.

In vivo calcium analysis (GCaMP)

The isosbestic signal (405 nm) was fitted to the calcium-dependent (465 nm) signal using a linear least squares method implemented in a custom MATLAB script. Then ΔF/F was calculated as (465 nm – fitted 405 nm) / fitted 405 nm. For significant calcium event detection analysis, we used a combination of methodologies previously described(*367*). Events were detected using a threshold defined as the median plus two standard deviations of the entire recording, with events required to be 1.5 seconds or longer. The number of events detected per trial was then extracted and reported alongside heatmaps as %ΔF/F of entire recordings. Heatmaps were generated in Python using Min-Max normalization, scaled to a range of 0–1. For each mouse, the normalization range was determined based on the Vehicle condition: the average of the lowest 360 data points was set as the minimum, and the average of the highest 360 data points was set as the maximum. This normalization range, derived from the Vehicle condition, was then applied to the corresponding paired Danuglipron data for the same mouse. A moving average with a window and bin size of 10 smoothed the data, which was then plotted as a heatmap. Mice with missed virus injection or off-target fiber placement were excluded from analysis.

In vivo dopamine recording (dLight1.3b)

Mice were single-housed and habituated to the fiber optic cable and high-fat diet (HFD) for one hour over two consecutive days. On the test day, mice received an injection of either a drug (liraglutide [0.3 mg/kg], danuglipron [30 mg/kg], or orforglipron [1mg/kg]) or vehicle/saline, with the order of drug versus vehicle/saline injections randomized. Liraglutide and danuglipron were administered two hours before recording, while orforglipron was given four hours prior. Fiber

photometry data were recorded as described above. Fluorescent signals were collected from both dopamine-dependent (465 nm) and dopamine-independent isosbestic (405 nm) excitation wavelengths. During the testing sessions, small pellets of HFD (~10 mg) were dropped into a cup at two-minute intervals after the mice retrieved the pellet. 5 to 6 trials were conducted per mouse. The recording session was video recorded to timestamp food retrieval time. Dopamine recordings were conducted during the light phase, between ZT3 and ZT6.

***In vivo* dopamine analysis (dLight1.3b)**

The isosbestic signal (405 nm) was fitted to the dopamine-dependent (465 nm) signal using a linear least squares method implemented in a custom MATLAB script. Then ΔF/F was calculated as (465 nm – fitted 405 nm) / fitted 405 nm. To account for inter-animal differences in signal intensities, Z-scores were calculated for the ΔF/F signals. The baseline period for each food trial was defined as the 30-second interval prior to food retrieval. The mean and standard deviation of the baseline period were used to compute the Z-scores, with the formula: Z score = (F-Fμ(baseline))/std(baseline), where F is the 405 nm corrected 465 nm signal (ΔF/F), μ(baseline) is the mean, and std is the standard deviation of the baseline period. Video frames were analyzed to determine the exact timestamp when the mouse retrieved the pellet, which was defined as time 0 for each retrieval. The 30-second window centered around the food retrieval time was extracted. The area under the curve (AUC) and maximum fluorescence Z-scored within the food retrieval window was further extracted and analyzed for quantification of dopaminergic activity. 5 food trials were averaged per mouse. Mice with missed virus injections or off-target fiber placements were excluded from the analysis.

Statistical analyses

All data are presented as mean ±SEM unless otherwise noted. Statistical tests including paired or unpaired two-tailed t-tests, Kruskal-Wallis tests, Wilcoxon signed-rank tests, Pearson

regression, one-way ANOVA, two-way/repeated-measures ANOVA (with Bonferroni correction or Tukey's HSD post hoc tests), MANOVA (with MATS resampling), linear mixed effect models with beta regression (with Tukey's post hoc test) were performed using RStudio (v4.3.0), Python (v3.11.5), JupyterLab (v3.6.3), MATLAB (R2023a), or GraphPad Prism (v10.4.0). Brief descriptions of all experiments in each figure panel, sample sizes, mean ±SEM, statistical test, test statistics, and *P*-values are presented in Supplementary Table 1. **P* <0.05; ***P* <0.01; ****P* <0.001.

C3.5 Data availability

All data will be available on Dryad upon publication and select code will also be available on Github at https://github.com/UVACircMetNeuLab.

C3.6 Acknowledgements

We thank the members of the Güler, Deppmann, Campbell, and Provencio laboratories (University of Virginia) for comments and suggestions on the preparation of the manuscript. We are thankful for technical help from Stefani A. Mancuso and technical advice from Amrita Pathak, along with Anthony Spano (University of Virginia) who developed the three viral constructs. We thank Talmo Pereira (Salk Institute for Biological Studies) and Caleb Weinreb (Harvard Medical School) for their technical advice. We thank the Genetically Engineered Murine Model (GEMM) Core (University of Virginia) for aiding in the CRISPR-Cas9 development of our mouse model.

Funding: We used AI-assisted technologies (OpenAI, Anthropic) as an aid for drafting and grammar proofing the manuscript. This work was supported by NIH R35GM140854 (ADG), NIH R01NS111220 (CDD), NIH R01HL153916 and American Diabetes Association Pathway to Stop

Diabetes Award 1-18-INI-14 (JNC), NIH R01 NS122834 (MKP), NIH R01 NS120702 (MKP), University of Virginia BRAIN Institute Seed Funding 2023 & 2024 (ADG, CDD) and 2024 & 2025 (ADG, JNC), University of Virginia BRAIN Institute Presidential Fellowship in Collaborative Neuroscience (ENG), University of Virginia National Science Foundation, EXPAND Traineeship (ENG), and the GEMM core partially supported by the funding of NIH-NCI CCSG P30 CA044579.

C3.7 Author contributions

Conceptualization: ENG, TBG, IRS, ABK, JNC, CDD, ADG

Data curation: ENG, TBG, IRS, TCJD, SO, YZ

Formal analysis: ENG, TBG, IRS, TCJD, ADG

Funding acquisition: ENG, MKP, JNC, CDD, ADG

Investigation: ENG, TBG, IRS, YZ, YS, NJC, ANW, OYC, SO, AA, KM, KIW, AK, GG

Methodology: ENG, TBG, IRS, ABK, AKB

Project administration: ADG

Resources: MKP, JNC, CDD, ADG

Supervision: ENG, TBG, IRS, MKP, JNC, CDD, ADG

Validation: ENG, TBG, IRS, AKB, CDD, ADG

Visualization: ENG, TBG, IRS

Writing – original draft: ENG, TBG, IRS, CDD, ADG

Writing – review & editing: ENG, TBG, IRS, JNC, CDD, ADG

Competing interests: The authors declare that they have no competing interest.

C3.8 Extended Data

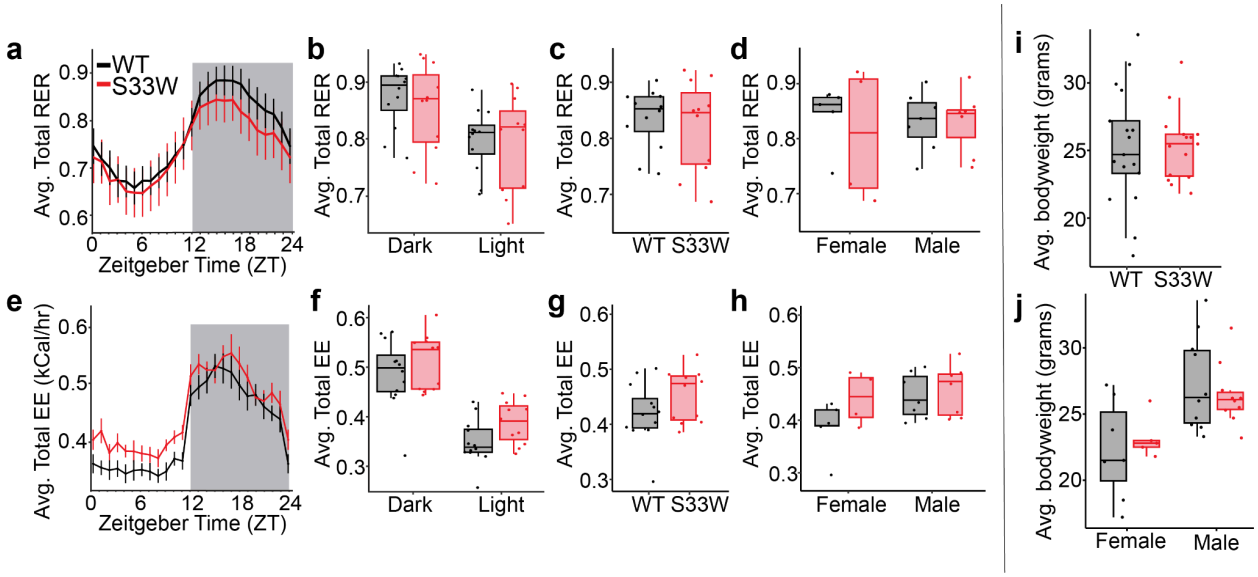

Extended Data Fig. 1. Metabolic profiling of WT and Glp1r^{S33W} mice. a,e, (Elizabeth Godschall, Isabelle Sajonia) Diurnal rhythms averaged over 3 days of (**a**) respiratory exchange ratio (RER) and (**e**) energy expenditure (EE) in WT and Glp1r^{S33W} mice. **b-g, (Elizabeth Godschall, Isabelle Sajonia)** Average dark/light phase and total 24 hour (**b,c**) RER and (**f,g**) EE between WT and Glp1r^{S33W} mice (*n* = 11-12 per genotype, two-way ANOVA with Bonferroni correction or Welch's t-test). **d,h, (Elizabeth Godschall, Isabelle Sajonia)** Total 24 hour (**d**) RER and (**h**) EE averaged by sex (*n* = 4-5 females, *n* = 7 males per genotype, two-way ANOVA with Bonferroni correction). **i, (Elizabeth Godschall)** Average baseline body weight of WT and Glp1r^{S33W} mice 10 to 20 weeks old (*n* = 18-19 per genotype, Welch's t-test). **j, (Elizabeth Godschall)** Average baseline body weight of WT and Glp1r^{S33W} male and female mice (*n* = 8-9 females, *n* = 10 males per group, two-way ANOVA with Bonferroni correction). Data are represented as medians ± Q1-Q3. **P*<0.05; ***P*<0.01; ****P*<0.001.

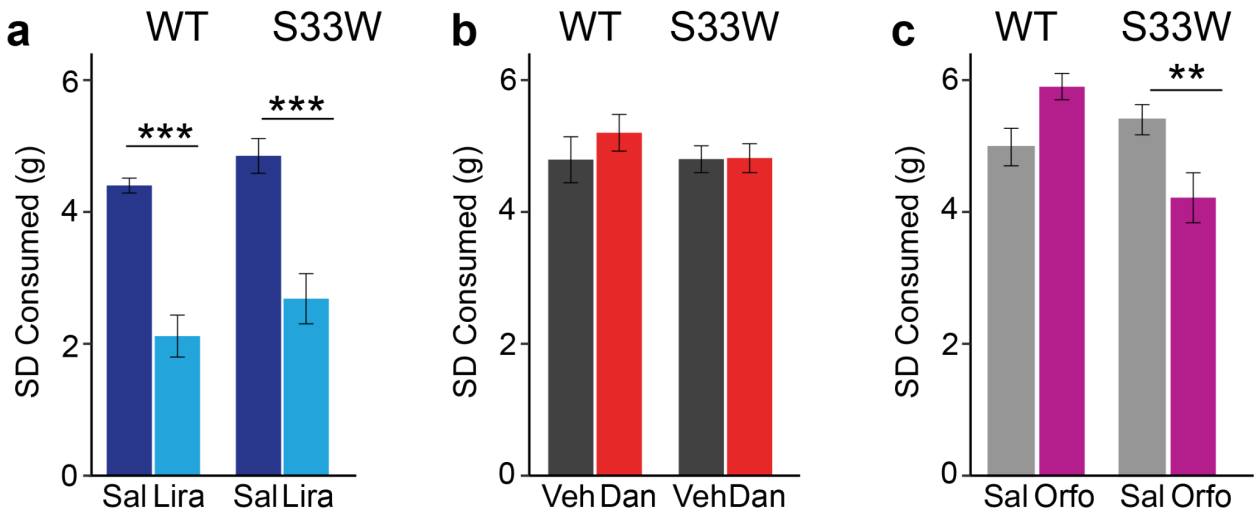

Extended Data Fig. 2. 24-hour effects of GLP1RAs on standard diet consumption. a-c, (Elizabeth Godschall) Standard diet (SD) consumption 24 hours after (**a**) liraglutide, (**b**) danuglipron, and (**c**) orforglipron injection in WT and $Glp1r^{S33W}$ mice. (*n* = 6 per injection, two-way ANOVA with Bonferroni correction, ***P*<0.01; ****P*<0.001). Data are represented as means ± SEM.

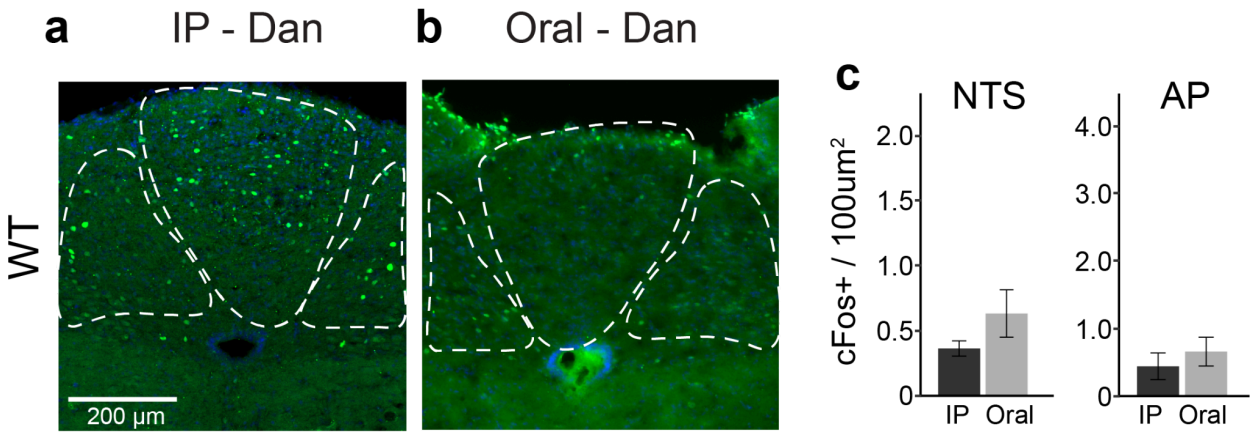

Extended Data Fig. 3. cFos activation in NTS and AP of WT mice administered oral or IP danuglipron. a,b, (Elizabeth Godschall) Neuronal cFos activation in the NTS and AP 2-hours after danuglipron was administered to WT mice via (**a**) IP injection or (**b**) oral gavage. **c**, Quantification of cFos expression in the NTS (left) or AP (right) following danuglipron IP or oral delivery in WT mice (*n* = 3-4 per delivery route, Welch's t-test). Data are represented as means ± SEM. **P*<0.05; ***P*<0.01; ****P*<0.001.

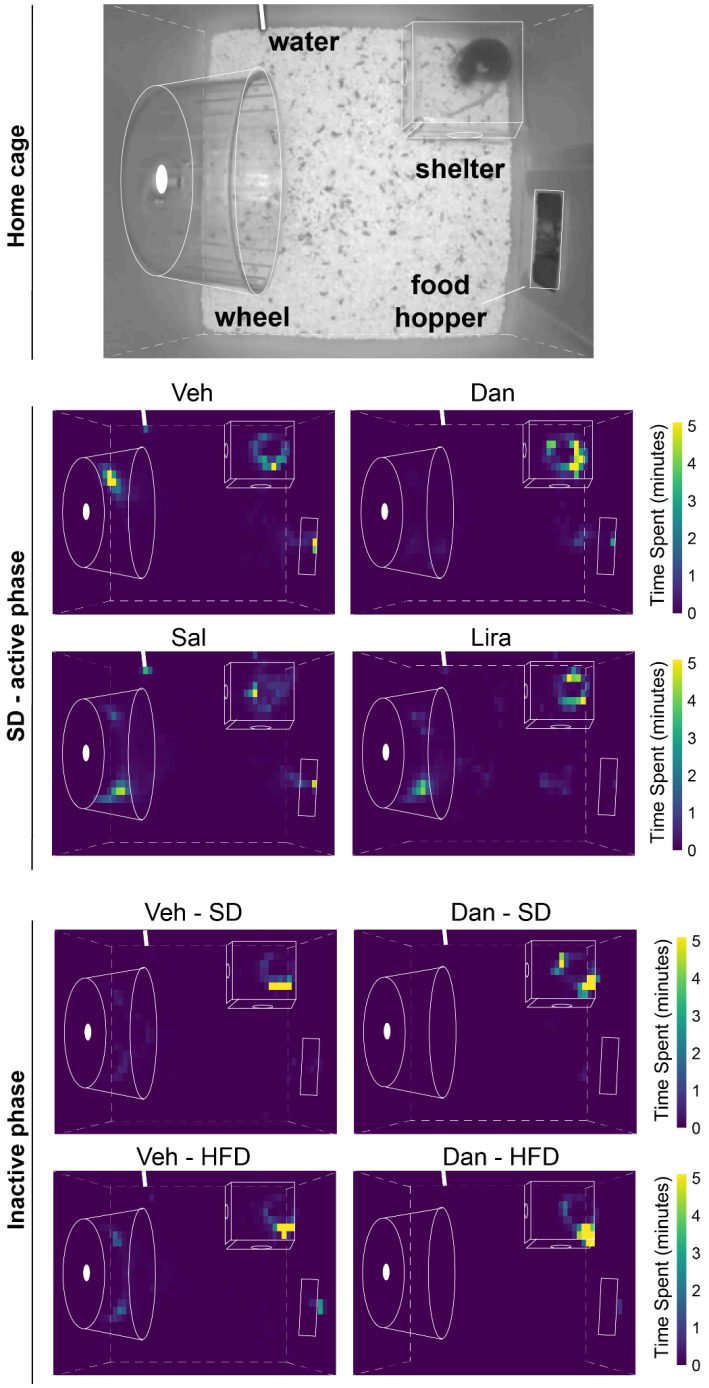

Extended Data Fig. 4. Home cage monitoring heatmaps of Glp1r^{S33W} mice (Isabelle Sajonia). Representative image of home cage set-up (dimensions: 30 x 30 x 43.5 cm) with calibrated positions of wheel, IR translucent shelter (10.5 x 10.5 x 6 cm), food hopper (5.5 cm from floor), and water bottle spout (5 cm from floor) identified in white outline (top). Coordinate-based heatmaps of nose keypoint trajectories recorded at 25 fps over 2-hour sessions for each treatment group during active (ZT 12-14) or inactive (ZT 3-5) phase. Color scale represents dwelling time in seconds.

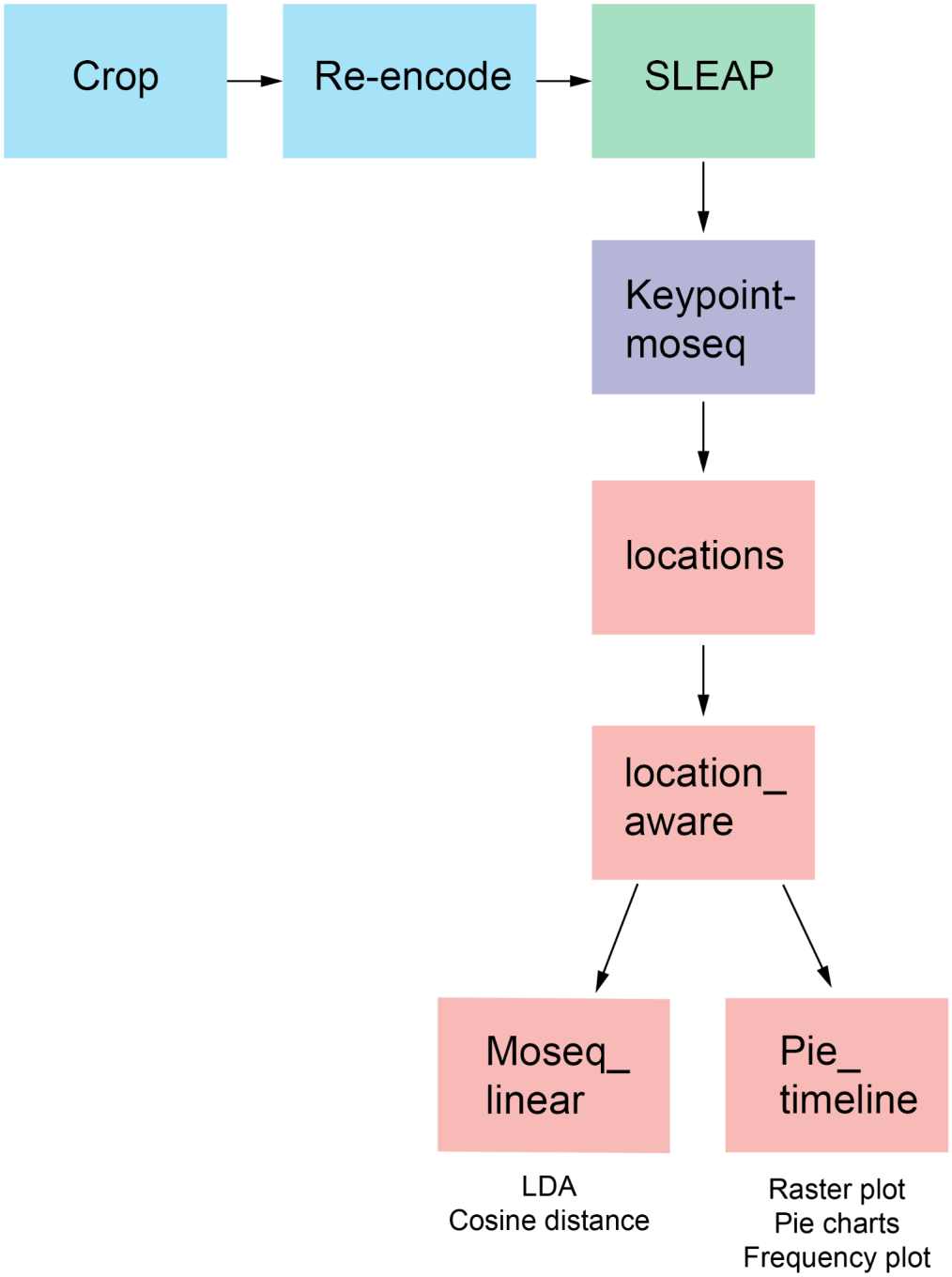

Extended Data Fig. 5. Machine-learning assisted pipeline for home cage behavioral analysis (Isabelle Sajonia) . Blue squares represent video pre-processing steps. Social LEAP Estimates Animal Poses (SLEAP) was used to extract nine keypoint coordinates for each mouse in the videos (Fig. 3, A to B; fig. S4). Keypoint Motion Sequencing (Keypoint-MoSeq) identified behavioral syllables from these coordinates (fig. S6). Red squares represent Python scripts used for the analysis of Keypoint-MoSeq syllable results: locations (identify regions of interest), location_aware (**Fig. 3c-n**), lda_cosine (**Fig. 3l,n**), and pie_timeline (**Fig. 3b,e,f,m**).

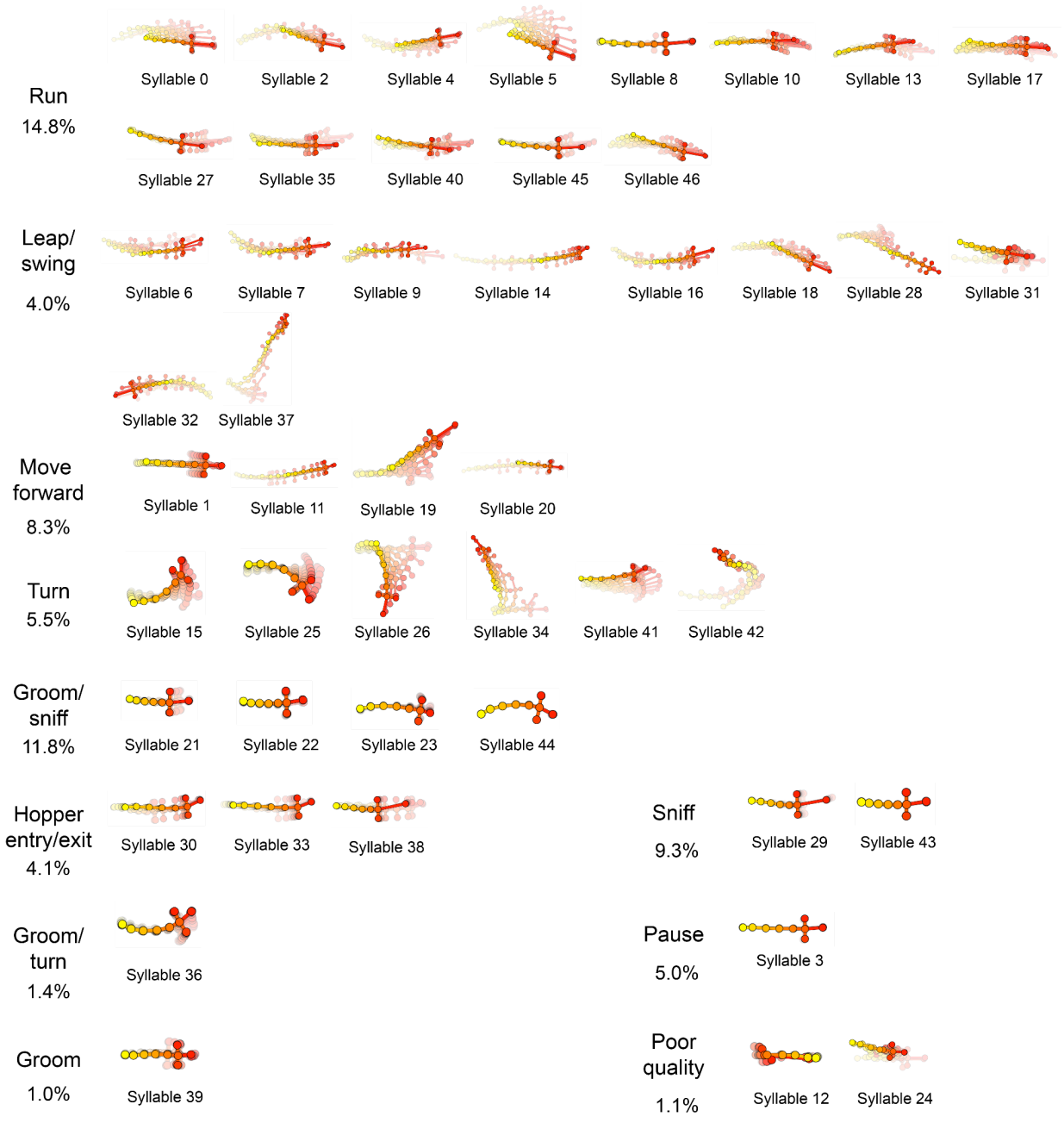

Extended Data Fig. 6. Trajectory plots of main behavioral syllables identified by Keypoint-MoSeq (Isabelle Sajonia). Syllables identified from keypoint coordinates by Keypoint-MoSeq were sorted into 11 categories by trained raters using grid movies generated for each syllable. The proportion of each syllable category is presented as a percentage. Rare syllables (minimum frequency < 0.5% but ≥ 0.01%) are not visually depicted but were included in the analysis.

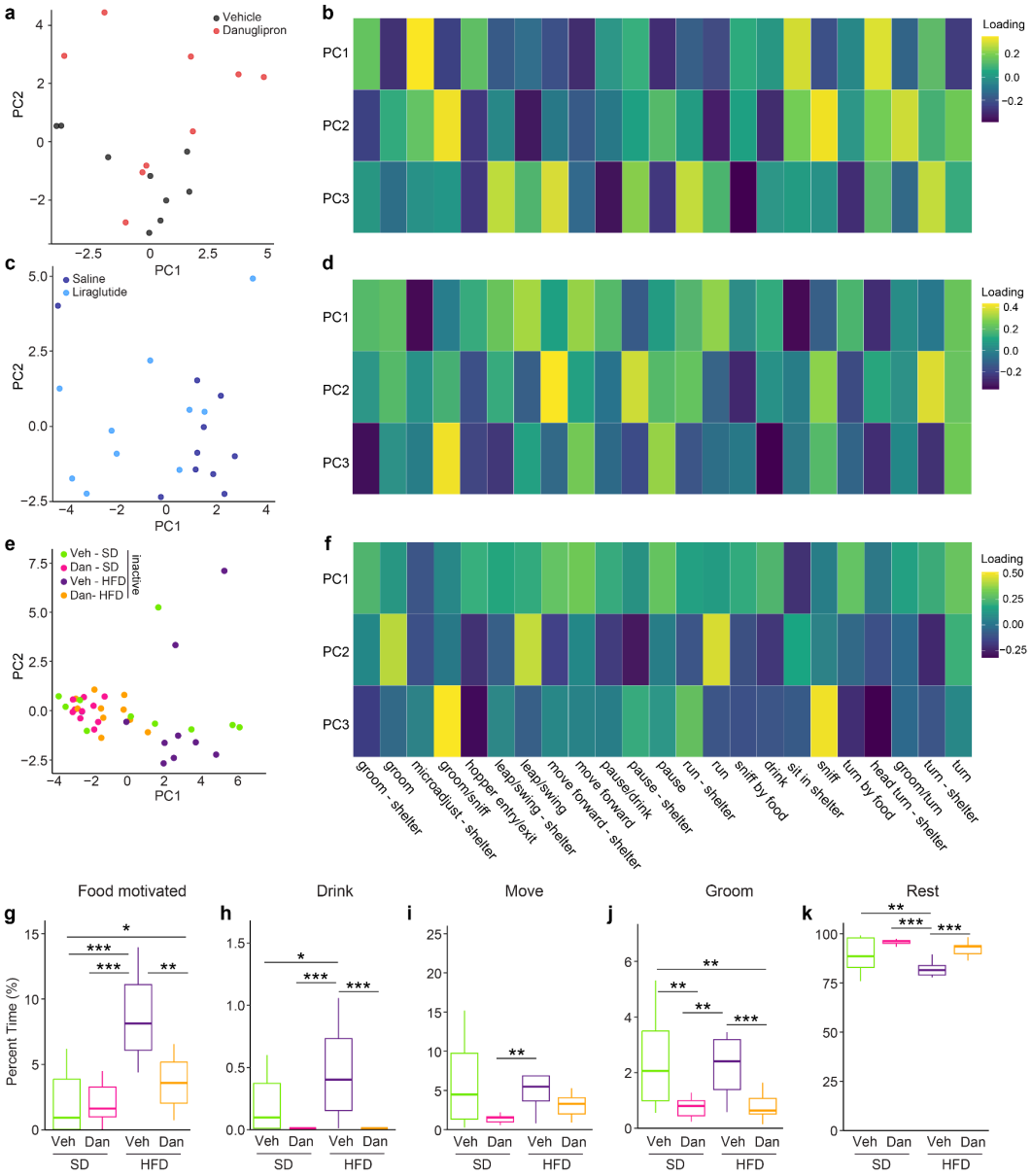

Extended Data Fig. 7. Principal component analysis and inactive phase behaviors. a–f, (Isabelle Sajonia) Principal Component Analysis (PCA) of 23 behavioral durations recorded during 2-hour home cage video sessions. PCA score plots for: (**a**) Vehicle and danuglipron-treated mice, (**c**) saline and liraglutide-treated mice, and (**e**) inactive-phase SD- and HFD-fed mice treated with vehicle or danuglipron. Corresponding PCA loading plots illustrating: (**b**) vehicle and danuglipron, (**d**) saline and liraglutide, and (**f**) inactive-phase SD- and HFD-fed mice treated with vehicle or danuglipron. **g–k, (Isabelle Sajonia)** Proportion of time allocated to five behavioral categories during the inactive phase for SD- and HFD-fed mice on vehicle or danuglipron: (**g**) food-motivated behaviors, (**h**) drinking, (**i**) movement/exploration, (**j**) grooming, and (**k**) resting behaviors (n = 10 per injection, (n = 10, generalized linear mixed-effects model (beta distribution) with main effects of drug and diet, as well as their interaction, followed by Tukey's post-hoc test, *P<0.05; **P<0.01; ***P<0.001). Data are represented as medians ± Q1-Q3. *P<0.05; **P<0.01; ***P<0.001.

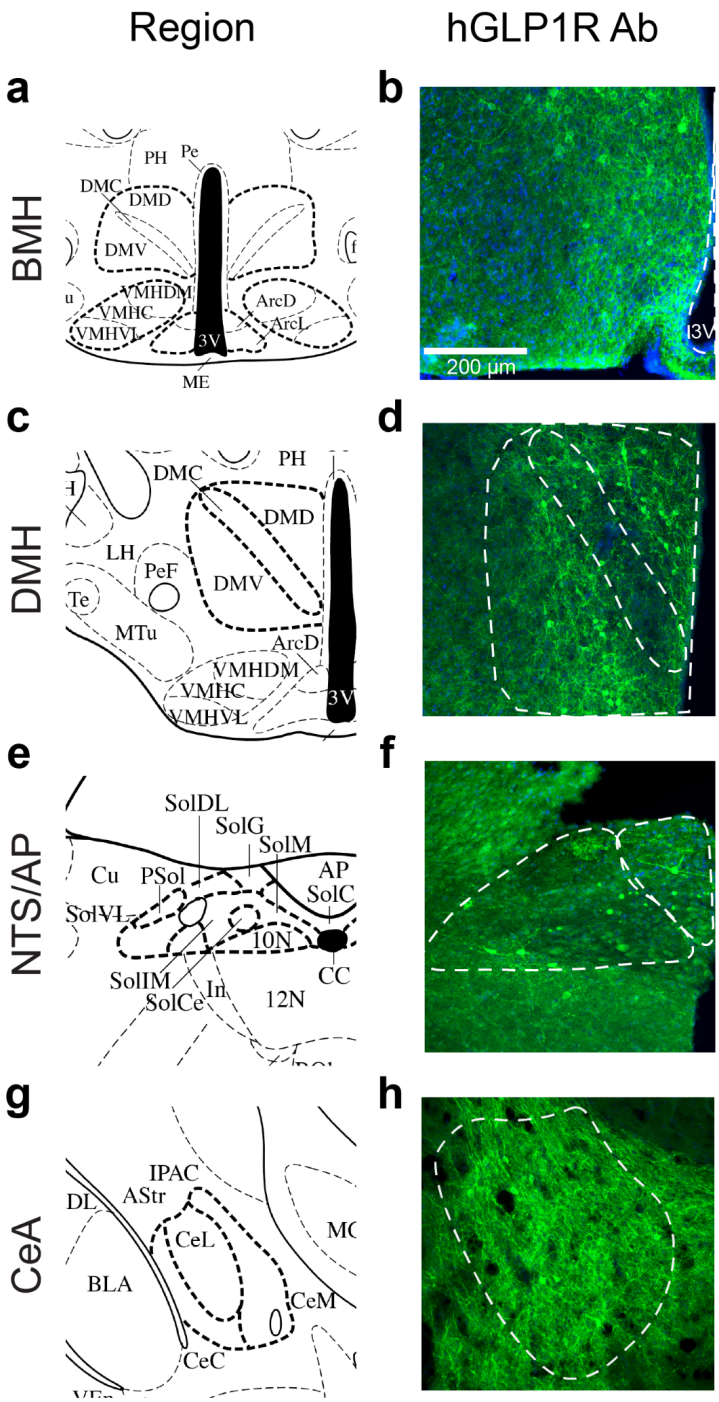

Extended Data Fig. 8. Validation of AAV-hSyn-DIO-hGLP1R virus. a-h, (Elizabeth Godschall) Fluorescent microscopy images of the brain regions stereotaxically injected with AAV-DIO-hGLP1R. Images from Allen Brain Atlas, with regions of interest in bold and hGLP1R antibody staining (green) in the (**a,b**) basomedial hypothalamus (BMH), (**c,d**) DMH, (**e,f**) NTS/AP, or (**g,h**) CeA. Scale bars = 200 µm.

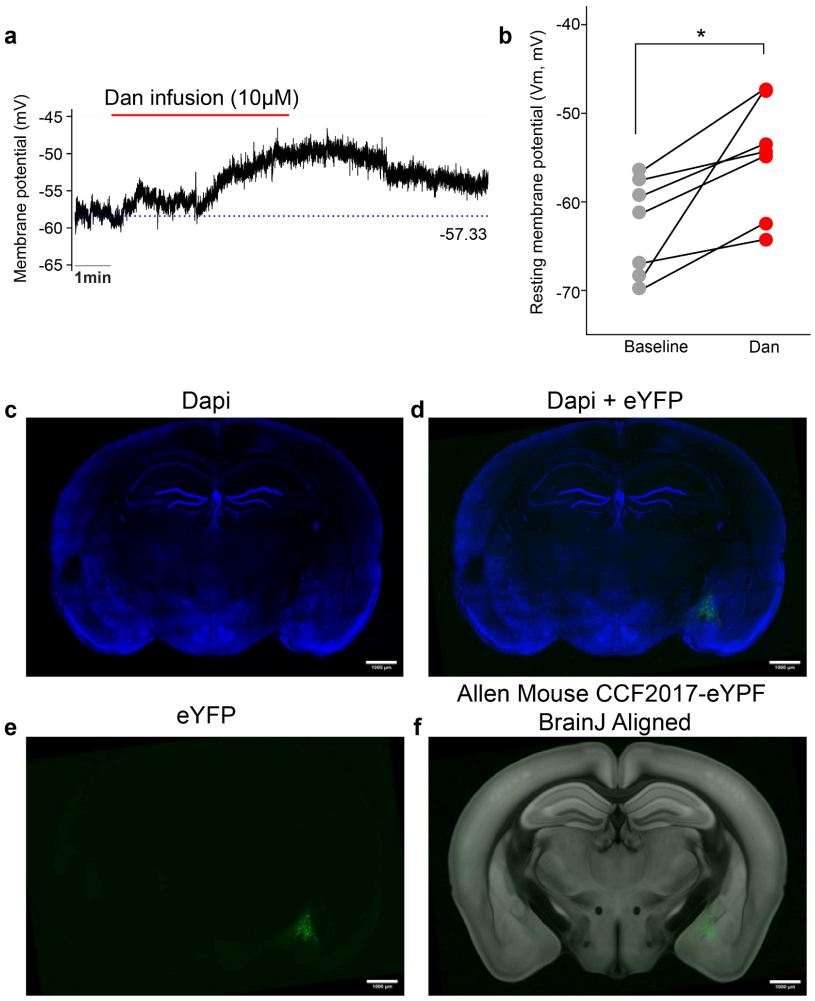

Extended Data Fig. 9. Danuglipron depolarizes the resting membrane potential in hGLP1R-expressing CeA neurons. a, (Tyler Deutsch, Manoj Patel) Representative trace showing the effect of 5 minutes of danuglipron perfusion (10 μM) on the resting membrane potential of CeA neurons. **b, (Tyler Deutsch, Manoj Patel)** Average depolarization induced by danuglipron compared to baseline recording. Baseline: −62.72 ± 2.08 mV; danuglipron: −54.87 ± 2.49 mV; average change: 7.8 mV (*n* = 7 cells, Wilcoxon signed-rank test, **P*<0.05). **c–f, (Tyler Deutsch, Bugra Gungul)** Localization of eYFP-labeled hGLP1R-expressing neurons in the central amygdala (CeA). BrainJ software(*368*) analysis indicates prominent eYFP labeling in the capsular part of the CeA, with additional labeling in the lateral part. Scale bars = 1000 μm.

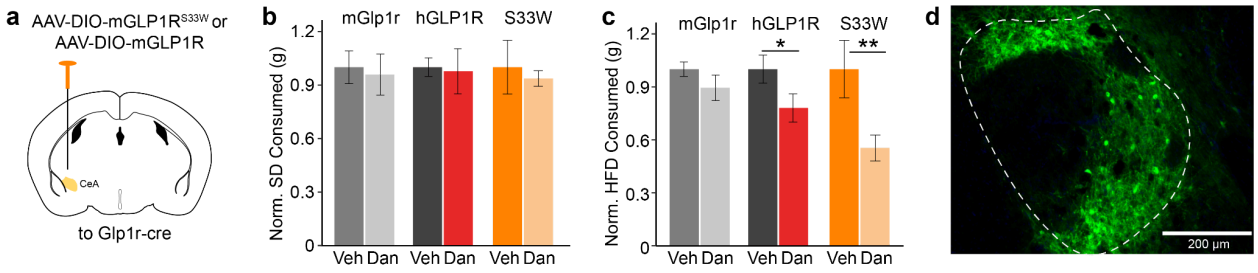

Extended Data Fig. 10. AAV-DIO-mGLP1R^{S33W}-HA targeted to the CeA of Glp1r-Cre mice recapitulates effects of AAV-DIO-hGLP1R. a, **(Elizabeth Godschall, Tony Spano)** Schematic of Glp1r-Cre mice injected with a Cre-dependent AAV carrying full length mouse Glp1r (mGlp1r) or AAV carrying full length mouse GLP1R with the S33W mutation at position 33 (mGLP1R^{S33W}) in the CeA. **b,c**, **(Elizabeth Godschall)** Normalized 4-hour (**b**) SD and (**c**) HFD consumption post-injection of vehicle or danuglipron in mGlp1r, full length human GLP1R (hGLP1R) or mGlp1r-S33W (S33W) expressing mice (*n* = 4-9 per group, two-way ANOVA with Bonferroni correction, **P*<0.05; ***P*<0.01). **d**, **(Elizabeth Godschall)** Representative image of AAV-DIO-mGLP1R^{S33W}-HA expression in the CeA (green). Scale bars = 200 µm. Data are represented as means ± SEM. **P*<0.05; ***P*<0.01; ****P*<0.001.

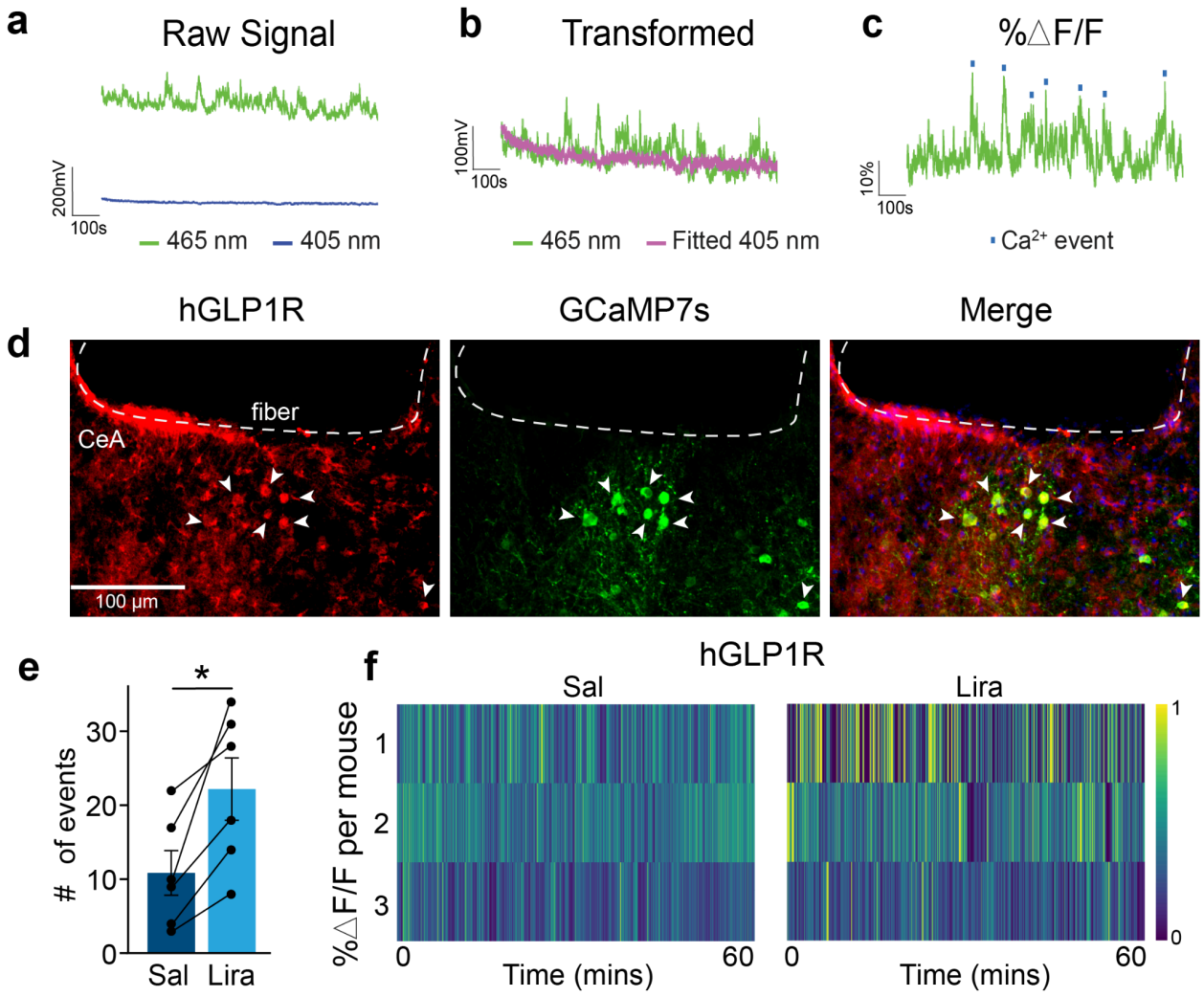

Extended Data Fig. 11. Fiber photometry recordings and validation of CeA^{GLP1R} neurons. **a**, **(Bugra Gungul)** Representative traces of fiber photometry recordings showing calcium-dependent fluorescence (465nm) and calcium-independent, isosbestic fluorescence (405nm) signals. **b**, **(Bugra Gungul)** Fitted 405nm signal (pink) transformed for ΔF/F calculation. **c, (Bugra Gungul)** Representative trace of %ΔF/F used for analysis. Blue dots indicate detected calcium events, identified using a threshold set at 2 standard deviations plus the median of the entire 1-hour recording session, with an event required to be longer than 1.5 seconds. **d**, **(Bugra Gungul, Elizabeth Godschall)** Representative images of AAV-DIO-GCaMP7s + hGLP1R targeted to the CeA. Validation with hGLP1R antibody (red; left), GCaMP7s (green; middle), and verification of colocalization (right). Scale bars = 100 µm. **e**, **(Bugra Gungul)** Number of significant calcium events averaged per mouse during 1-hour recording session following saline or liraglutide in CeA-hGLP1R expressing mice (*n* = 6 per injection, paired t-test, **P*<0.05). **f**, **(Bugra Gungul, Isabelle Sajonia)** Representative heatmaps of %ΔF/F neuronal calcium signal per mouse during 1-hour of fiber photometry recording after saline (left) or liraglutide (right) injection in CeA-hGLP1R expressing mice. Data are represented as means ± SEM. **P*<0.05; ***P*<0.01; ****P*<0.001.

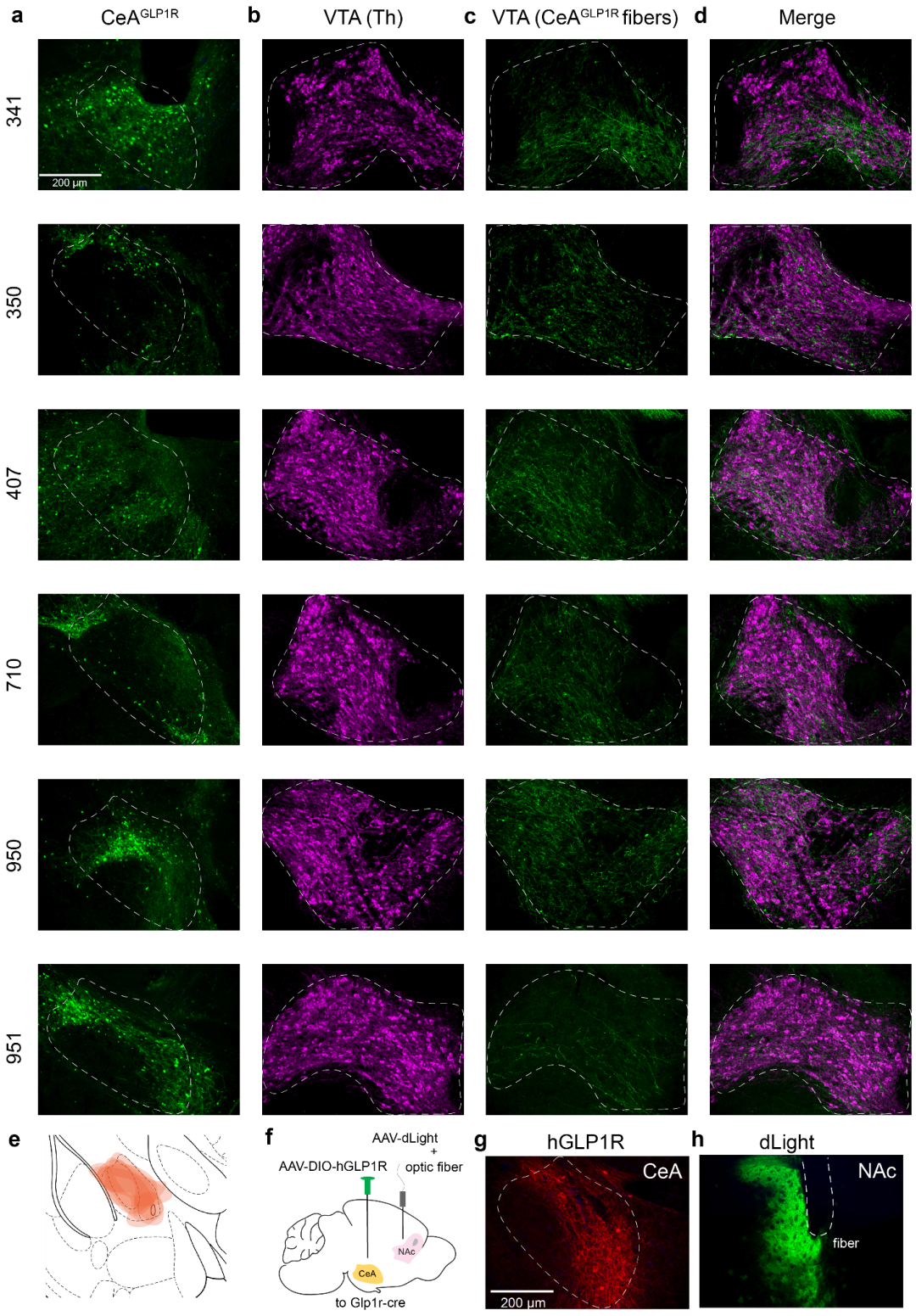

Extended Data Fig. 12. CeA^{GLP1R} neurons innervate the VTA and validation of AAVs targeting CeA and NAc. a, **(Bugra Gungul, Elizabeth Godschall)** Representative images of AAV-DIO-ChR2-eYFP expression targeted to the CeA of Glp1r-Cre mice (green; *n* = 6). **b**,

(Bugra Gungul, Elizabeth Godschall) Tyrosine hydroxylase (Th) expression in the VTA (magenta). **c**, **(Bugra Gungul, Elizabeth Godschall)** Axon fiber projections from CeA^{GLP1R} neurons into the VTA, and **d**, **(Bugra Gungul, Elizabeth Godschall)** colocalization of Th with CeA^{GLP1R} fibers in the VTA. **e**, **(Elizabeth Godschall)** Traces of superimposed AAV-DIO-ChR2-eYFP injection targeting per mouse, collapsed on the Allen Brain Atlas figure. **f**, **(Elizabeth Godschall)** Schematic showing AAV-dLight1.3b injection into the NAc and AAV-DIO-hGLP1R injection into the CeA of Glp1r-Cre mice, with fiber optic implants in the NAc. **g**, **(Bugra Gungul, Elizabeth Godschall)** Validation of AAV-DIO-hGLP1R targeting the CeA using hGLP1R antibody staining (red). **h**, **(Bugra Gungul, Elizabeth Godschall)** Representative AAV-dLight expression in the NAc and fiber optic implant placement (green). Scale bars = 200 μm.

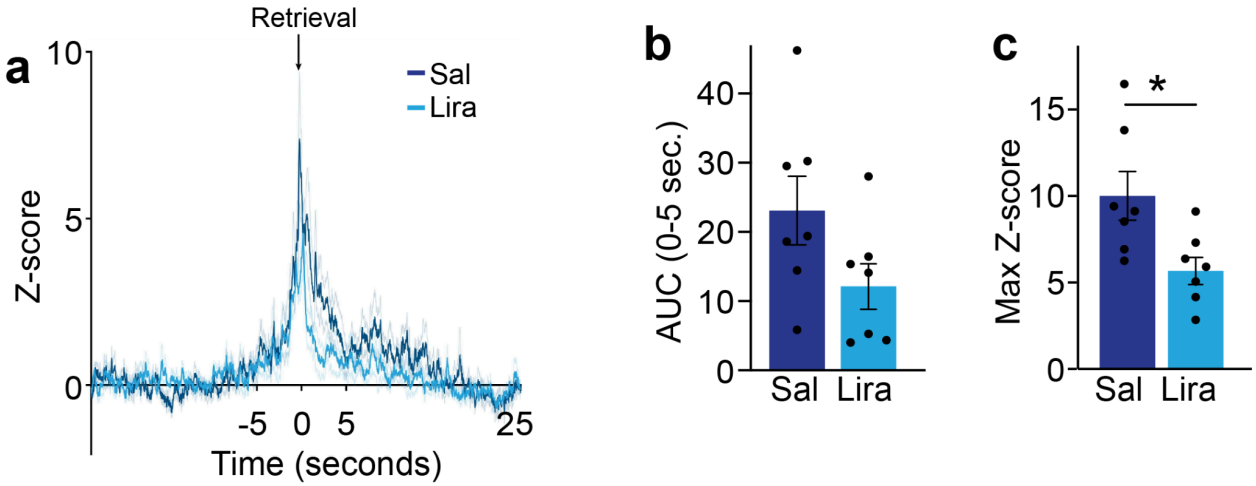

Extended Data Fig. 13. Liraglutide reduces NAc dopamine release in response to HFD. a, (Bugra Gungul) Averaged Z-score traces showing dopamine release in the NAc in response to HFD following administration of saline or liraglutide in $Glp1r^{S33W}$ mice. Traces are aligned to food retrieval time (t = 0) and averaged across five food trials per mouse. **b,c**, **(Bugra Gungul)** Quantified (**b**) area under the curve (AUC) for Z-scores and (**c**) maximum fluorescence Z-scores within the food retrieval window (n = 7, paired t-test, *P<0.05). Data are represented as means ± SEM. *P<0.05; **P<0.01; ***P<0.001.

C3.9 Supplementary Materials

Supplementary Table 1 **(Elizabeth Godschall)**

Figure	Sample Type (mouse line)	Number of Sample (n/trial)	Behavior Test	Drug or Virus Injection	Description	Statistical Test	Degrees of Freedom (df)	Mean +/- SEM	Statistics	Adjusted p-v
Fig. 1b	C57BL6J	11 / injection	Food Intake	Liraglutide, Danuglipron, Saline, Vehicle	SD intake measured 2 hours after injection	One-way ANOVA w/ Bonferroni Correction	40	S: 0.9 +/- 0.03 L: 0.37 +/- 0.05 V: 0.84 +/-0.07 D: 0.7 +/- 0.08	F(3, 40) = 15.12 p = <0.0001	D-L: 0.0027 D-S: 0.1462 D-V: 0.711 L-S: <0.0001 L-V: <0.0001 S-V: 1.00
Fig. 1f	Glp1r S33W and WT	8 WT / 6 S33W	GTT	Liraglutide	Fasted glucose levels up to 2 hours (liraglutide, danuglipron) or 6 hours (orforglipron) after injection	Two-way ANOVA w/ Bonferroni Correction	84		F(13, 84) = 10.62 p = <0.0001	-15: 0.037 -1: 0.403 15: 0.021 30: 0.055 60: 0.318 90: 0.228 120: 0.164
Fig. 1g		9 WT / 6 S33W		Danuglipron			91		F(13, 91) = 37.32 p = <0.0001	-15: 0.885 -1: 0.415 15: <0.0001 30: <0.0001 60: <0.0001 90: 0.008 120: 0.026
Fig. 1h		5 WT / 5 S33W		Orforglipron			56		F(13, 56) = 35.86 p = <0.0001	-240: 0.833 -1: 0.1401 15: <0.0001 30: <0.0001 60: 0.0004 90: 0.0037 120: 0.0032
Fig. 1i		10-11 / injection	Food Intake	Liraglutide and Saline	SD intake measured up to 4 hours after injection for danuglipron and liraglutide or up to 8 hours after orforglipron		57	1S: 0.43+/-0.05 1L: 0.29+/-0.06 2S: 0.94+/-0.08 2L: 0.45+/-0.08 4S: 1.82+/-0.13 4L: 0.54+/-0.06	F(5, 57) = 43.81 p = <0.0001	1hr = 0.271 2hr = 0.0002 4hr = <0.0001
Fig. 1j		9 / injection					48	1S: 0.56+/-0.19 1L: 0.3+/-0.06 2S: 1.08+/-0.22 2L: 0.48+/-0.06 4S: 2.04+/-0.27 4L: 0.7+/-0.06	F(5, 48) = 14.33 p = <0.0001	1hr = 0.289 2hr = 0.014 4hr = <0.0001
Fig. 1k		16 / injection		Danuglipron and Vehicle			90	1V: 0.25+/-0.05 1D: 0.21+/-0.03 2V: 0.71+/-0.06 2D: 0.78+/-0.05 4V: 1.68+/-0.11 4D: 1.74+/-0.10	F(5, 90) = 84.77 p = <0.0001	1hr = 0.717 2hr = 0.469 4hr = 0.587
Fig. 1l		15 / injection					84	1V: 0.34+/-0.06 1D: 0.14+/-0.05 2V: 0.89+/-0.10 2D: 0.43+/-0.07 4V: 1.73+/-0.07 4D: 1.22+/-0.12	F(5, 84) = 54.7 p = <0.0001	1hr = 0.087 2hr = 0.0001 4hr = <0.0001
Fig. 1m		8 / injection		Orforglipron and Saline			42	1S: 0.67+/-0.09 1O: 0.7+/-0.05 2S: 1.08+/-0.09 2O: 1.06+/-0.07 4S: 1.5+/-0.12 4O: 1.51+/-0.07	F(5, 42) = 18.14 p = <0.0001	1hr = 0.9181 2hr = 0.9181 4hr = 0.9181
Fig. 1n		9 / injection					48	1S: 0.68+/-0.08 1O: 0.33+/-0.08 2S: 1.1+/-0.09 2O: 0.47+/-0.08 4S: 1.76+/-0.15 4O: 0.86+/-0.16	F(5, 48) = 21.43 p = < 0.0001	1hr = 0.0334 2hr = 0.0002 4hr = <0.0001

Fig. 1o	Glp1r S33W and WT	10 / injection	Food Intake	Liraglutide and Saline	HFD intake measured up to 4 hours after injection for danuglipron and liraglutide or up to 8 hours after orforglipron	Two-way ANOVA w/ Bonferroni Correction	54	1S: 0.91+/-0.08 1L: 0.61+/-0.09 2S: 1.17+/-0.13 2L: 0.69+/-0.08 4S: 1.58+/-0.13 4L: 0.8+/-0.09	F(5, 54) = 12.7 p = <0.0001	1hr = 0.041 2hr = 0.002 4hr = <0.0001
Fig. 1p		8 / injection					42	1S: 1.09+/-0.12 1L: 0.64+/-0.14 2S: 1.32+/-0.15 2L: 0.69+/-0.15 4S: 1.92+/-0.17 4L: 0.76+/-0.19	F(5, 42) = 10.65 p = <0.0001	1hr = 0.042 2hr = 0.005 4hr = <0.0001
Fig. 1q		16 / injection		Danuglipron and Vehicle			90	1V: 0.84+/-0.08 1D: 0.55+/-0.06 2V: 1.09+/-0.10 2D: 1.0+/-0.11 4V: 1.63+/-0.14 4D: 1.49+/-0.13	F(5, 90) = 14.3 p = <0.0001	1hr = 0.054 2hr = 0.563 4hr = 0.342
Fig. 1r		14 / injection					78	1V: 1.0+/-0.08 1D: 0.31+/-0.04 2V: 1.31+/-0.12 2D: 0.57+/-0.06 4V: 1.8+/-0.16 4D: 1.14+/-0.09	F(5, 78) = 28.87 p = <0.0001	1hr = <0.0001 2hr = <0.0001 4hr = <0.0001
Fig. 1s		8 / injection		Orforglipron and Saline			42	1S: 1.15+/-0.06 1O: 1.21+/-0.7 2S: 1.39+/-0.07 2O: 1.5+/-0.08 4S: 1.86+/-0.06 4O: 2.0+/-0.08	F(5, 42) = 23.94 p = <0.0001	1hr = 0.535 2hr = 0.267 4hr = 0.176
Fig. 1t		9 / injection					48	1S: 1.19+/-0.07 1O: 0.69+/-0.09 2S:1.5+/-0.10 2O: 0.97+/-0.17 4S: 1.89+/-0.11 4O: 1.29+/-0.20	F(5, 48) = 9.728 p = <0.0001	1hr = 0.0111 2hr = 0.007 4hr = 0.0027
Fig. 1u		6 WT / 6 S33W	Oral GTT	Danuglipron	Fasted glucose levels up to 2 hours after danuglipron oral gavage		70		F(13, 70) = 15.95 p = <0.0001	-15: 0.971 -1: 0.265 15: 0.005 30: <0.0001 60: 0.019 90: 0.177 120: 0.278
Fig. 1v	Glp1r S33W	8-9 / injection	Food Intake	Danuglipron and Vehicle	Oral administration of Dan or Orfo + HFD Food Intake	Two-way ANOVA w/ Bonferroni Correction	45	1V: 0.98+/-0.12 1D: 0.36+/-0.09 2V: 1.46+/-0.16 2D: 0.57+/-0.11 4V: 2.0+/-0.19 4D: 1.23+/-0.21	F(4, 45) = 15.55 p <0.0001	1hr = 0.0062 2hr = 0.0001 4hr = 0.0009
Fig. 1w							41	IP-V: 1.8+/-0.16 IP-D: 1.14+/-0.1 O-V: 2.0+/-0.19 O-D: 1.2+/-0.63	F(3, 41) = 6.97 p = 0.0007	IP = 0.0017 Oral = 0.005
Fig. 1x		8 / injection		Orforglipron and Saline			42	1S: 1.33+/-0.06 1O: 0.81+/-0.10 2S: 1.76+/-0.12 2O: 1.06+/-0.09 4S: 2.22+/-0.09 4O: 1.42+/-0.14	F(5, 42) = 24.72 p <0.0001	1hr = 0.0009 2hr = <0.0001 4hr = <0.0001
Fig. 1y							30	IP-S: 1.89+/-0.11 IP-O: 1.29+/-0.2 O-S: 2.22+/-0.09 O-O: 1.42+/-0.14	F(3, 30) = 8.508 p = 0.00031	IP = 0.0056 Oral = 0.0008
Fig. 1z		7 / injection	Weight Loss	Orforglipron and Saline	Chronic orfo or saline injections to overweight mice on HFD for > 8 week	Paired t-test	80	O: -1.99+/-0.23 S: 1.29+/-0.35	t(80) = -6.154 p <0.0001	

Fig. 2e	Glp1r S33W and WT	3-4 / injection	Image Analysis	Danuglipron, Orforglipron, Liraglutide	Quantified cFos+ neurons divided by area in brain regions of interest: (e) DMH, (f) NTS, (g) AP, and (h) CEA	Two-way ANOVA w/ Bonferroni Correction	18	D-W: 1.32+/-0.39 D-S: 1.65+/-0.09 O-W: 1.3+/-0.13 O-S: 1.12+/-0.12 L-W: 1.59+/-0.06 L-S: 1.37+/-0.19	F(5, 18) = 1.046 p = 0.4215	Dan = 0.2441 Orfo = 0.5984 Lira = 0.4414
Fig. 2f							17	D-W: 0.34+/-0.10 D-S: 2.23+/-0.47 O-W: 0.39+/-0.1 O-S: 1.96+/-0.04 L-W: 1.71+/-0.13 L-S: 1.24+/-0.2	F(5, 17) = 18.57 p <0.0001	Dan = <0.0001 Orfo = <0.0001 Lira = 0.0819
Fig. 2g							17	D-W: 0.71+/-0.36 D-S: 4.02+/-0.61 O-W: 0.17+/-0.03 O-S: 2.4+/-0.38 L-W: 2.95+/-1.0 L-S: 2.58+/-0.62	F(5, 17) = 5.591 p = 0.00317	Dan = 0.0017 Orfo = 0.0161 Lira = 0.6562
Fig. 2h							18	D-W: 0.28+/-0.05 D-S: 0.84+/-0.07 O-W: 0.3+/-0.07 O-S: 0.95+/-0.12 L-W: 1.56+/-0.32 L-S: 1.25+/-0.18	F(5, 18) = 9.671 p = 0.00013	Dan = 0.0279 Orfo = 0.0116 Lira = 0.1907
Fig. 2i	Glp1r S33W				Ratio of NTS / AP cFos+ cells in Glp1r S33W mice compared among injections	Kruskal-Wallis test	2	D: 0.54+/-0.04 O: 0.88+/-0.12 L: 0.53+/-0.09	Chi-squared = 6.167 p = 0.045	
Fig. 2l				Danuglipron	Comparison between cFos activation via IP and oral delivery of danuglipron in the AP and NTS	Welch's t-test	NTS: 2 AP: 3	NTS IP: 2.2+/-0.47 O: 1.5+/-0.05 AP IP: 4.2+/-0.7 O: 1.23+/-0.5	NTS: t(2) = 1.56 p = 0.2562 AP: t(3) = 3.27 p = 0.0373	
Fig. 3c	Glp1r S33W	78	Home Cage Behavior	Danuglipron, Liraglutide, Saline, Vehicle	Correlation between infared beam breaks into food hopper and machine learning food-motivated predicted behaviors	Pearsons's correlation			r = 0.72 p <0.0001	
Fig. 3d		78			Correlation between number of licks on water bottle and machine learning drinking predicted behaviors				r = 0.73 p <0.0001	
Fig. 3e		9 / injection			Proportion of time spent doing each of the 23 behaviors after Veh or Dan (e) and Lira or Sal (f) on SD in the active phase	Repeated measures MANOVA with modified ANOVA-type statistic (MATS) resampling			MATS = 8.71 p = 0.024	
Fig. 3f		10 / injection							MATS = 18.96 p <0.001	

Fig. 3g	Glp1r S33W	9-10 / injection	Home Cage Behavior	Danuglipron, Liraglutide, Saline, Vehicle	Percent changes in food motivated (g), drinking (h), moving (i), grooming (j), and resting (k) behaviors determined by machine learning pipeline between danuglipron or vehicle and liraglutide or saline during the active phase	linear mixed effect model with beta regression		D: 9.0+/-4.0 V: 15+/-7.0 L: 8.7+/-4.8 S: 16.5+/-8.2	Dan/Veh B = -2.28 p <0.0001 Lira/Sal B = -2.34 p <0.0001	D-V: p = 0.0362 L-S: p = 0.0029
Fig. 3h								D: 1.0+/-1.0 V: 2.5+/-1.5 L: 0.7+/-0.5 S: 2.8+/-0.9	Dan/Veh B = -4.834 p <0.0001 Lira/Sal B = -4.49 p <0.0001	D-V: p = 0.0017 L-S: p <0.0001
Fig. 3i								D: 37.6+/-24 V: 51.7+/-16.5 L: 35.7+/-18 S: 43+/-14.7	Dan/Veh B = -0.574 p = 0.0334 Lira/Sal B = -0.626 p = 0.0034	D-V: p = 0.0945 L-S: p = 0.2557
Fig. 3j								D: 8.9+/-7.6 V: 7.9+/-5.6 L: 7.0+/-4.0 S: 4.9+/-1.3	Dan/Veh B = -2.36 p <0.0001 Lira/Sal B = -2.64 p <0.0001	D-V: p = 0.8592 L-S: p = 0.1835
Fig. 3k								D: 43.6+/-24.5 V: 22.9+/-11.7 L: 47.9+/-19.4 S: 32.9+/-14.4	Dan/Veh B = -0.253 p = 0.3009 Lira/Sal B = -0.09 p = 0.661	D-V: p = 0.0187 L-S: p = 0.0425
Fig. 3m		10 / injection		Danuglipron and Vehicle		Repeated measures MANOVA with modified ANOVA-type statistic (MATS) resampling			SD-V/HFD-V: p = 0.012 HFD-V/SD-D: p = 0.006 HFD-V/HFD-D: p = 0.006	
Fig. 4b	Glp1r-cre	6 / injection	Food Intake	Danuglipron and Vehicle AAV-DIO-mCherry or AAV-DIO-hGLP1R	mCherry (b) or hGLP1R (c) to basomedial hypothalamus + SD	Two-way ANOVA w/ Bonferroni Correction	30	1V: 0.33+/-0.07 1D: 0.4+/-0.07 2V: 0.6+/-0.11 2D: 0.73+/-0.09 4V: 1.45+/-0.11 4D: 1.63+/-0.19	F(5, 30) = 23.82 p = <0.0001	1hr = 0.679 2hr = 0.410 4hr = 0.26
Fig. 4c		10 / injeciton					54	1V: 0.43+/-0.06 1D: 0.14+/-0.05 2V: 0.86+/-0.10 2D: 0.38+/-0.08 4V: 1.86+/-0.13 4D: 1.02+/-0.19	F(5, 54) = 32.12 p = <0.0001	1hr = 0.066 2hr = 0.0031 4hr = <0.0001
Fig. 4g		6 / injection			mCherry (g) or hGLP1R (h) to basomedial hypothalamus + HFD		30	1V: 0.55+/-0.10 1D: 0.55+/-0.08 2V: 0.97+/-0.14 2D: 0.72+/-0.10 4V: 1.82+/-0.15 4D: 1.48+/-0.11	F(5, 30) = 20.89 p = <0.0001	1hr = 1.00 2hr = 0.135 4hr = 0.050
Fig. 4h		10 / injeciton					54	1V: 0.65+/-0.12 1D: 0.66+/-0.19 2V: 1.15+/-0.14 2D: 0.99+/-0.09 4V: 1.8+/-0.09 4D: 1.84+/-0.12	F(5, 54) = 20.93 p = <0.0001	1hr = 0.952 2hr = 0.334 4hr = 0.808
Fig. 4d		7 / injection			hGLP1R to DMH + SD (d) or + HFD (i)		36	1V: 0.47+/-0.06 1D: 0.17+/-0.04 2V: 0.83+/-0.13 2D: 0.5+/-0.09. 4V: 1.7+/-0.21 4D: 1.16+/-0.20	F(5, 36) = 16.01 p = <0.0001	1hr = 0.134 2hr = 0.102 4hr = 0.009
Fig. 4i							36	1V: 0.79+/-0.22 1D: 0.57+/-0.11 2V: 1.1+/-0.22 2D: 0.99+/-0.12 4V: 1.73+/-0.23 4D: 1.51+/-0.16	F(5,36) = 5.65 p = 0.0006	1hr = 0.416 2hr = 0.663 4hr = 0.416

Fig. 4e	Glp1r-cre	6 / injection	Food Intake	Danuglipron and Vehicle AAV-DIO-mCherry or AAV-DIO-hGLP1R	hGLP1R to NTS/AP + SD (e) or + HFD (j)	Two-way ANOVA w/ Bonferroni Correction	30	1V: 0.32+/-0.05 1D: 0.20+/-0.07 2V: 0.80+/-0.12 2D: 0.58+/-0.12 4V: 2.0+/-0.29 4D: 1.28+/-0.24	F(5, 30) = 15.36 p = <0.0001	1hr = 0.636 2hr = 0.382 4hr = 0.006
Fig. 4j							30	1V: 0.97+/-0.07 1D: 0.63+/-0.08 2V: 1.32+/-0.11 2D: 0.82+/-0.07 4V: 2.18+/-0.12 4D: 1.48+/-0.16	F(5, 30) = 27.82 p = <0.0001	1hr = 0.035 2hr = 0.002 4hr = 0.0001
Fig. 4f		9 / injection			hGLP1R to CeA + SD (f) or + HFD (k)		48	1V: 0.26+/-0.06 1D: 0.19+/-0.07 2V: 0.58+/-0.07 2D: 0.58+/-0.11 4V: 1.47+/-0.08 4D: 1.43+/-0.19	F(5, 48) = 29.26 p = <0.0001	1hr = 0.654 2hr = 1.00 4hr = 0.823
Fig. 4k							47	1V: 0.96+/-0.10 1D: 0.54+/-0.08 2V: 1.13+/-0.13 2D: 0.83+/-0.08 4V: 1.82+/-0.15 4D: 1.42+/-0.15	F(5, 47) = 15.22 p = <0.0001	1hr = 0.016 2hr = 0.074 4hr = 0.018
Fig. 4n	Glp1r-cre	3-6 / injection	in vivo calcium imaging	AAV-DIO-GCaMP7s+hGLP1R or mGlp1r to CeA	CeA GLP1R calcium dynamics after Veh or Dan in hGLP1R-expressing mice (n) or mGlp1r-expressing mice (p) in their CeA	Paired t-test	5	V: 14.7+/-4.0 D: 32.5+/-4.83	t(5) = 4.67 p = 0.0055	
Fig. 4p						Wilcoxon signed-rank test	2	V: 21+/-5.57 D: 18+/-6.11	W = 0 p = 0.25	
Fig. 4r		6 eYFP / 6 ChR2	Food Intake	AAV-DIO-eYFP or AAV-DIO-ChR2 to CeA	30-minute HFD intake measured with stim ON or OFF	Two-way ANOVA w/ Tukey HSD	20	eYFP OFF: 0.52+/-0.059 eYFP ON: 0.59+/-0.061 ChR2 OFF: 0.59+/-0.045 ChR2 ON: 0.28+/-0.092	F(3, 20) = 5.12 p = 0.0087	ChR2 ON/OFF = 0.014 ChR2 ON/ eYFP ON = 0.015
Fig. 4t	Glp1r flox/flox	6 GFP / 6 Cre		AAV-GFP or AAV-Cre to CeA	SD or HFD intake measurements 4 hours after injection of liraglutide	Welch's t-test	SD: 6 HFD: 9	SD GFP: 0.33+/-0.1 Cre: 0.45+/-0.2 HFD GFP: 0.45+/-0.1 Cre: 0.72+/-0.1	SD: t(5.7) = 0.55 p = 0.6028 HFD: t(9.4) = 2.4 p = 0.03738	
Fig. 5e	Glp1r S33W	7-9 / injection	in vivo dopamine imaging	AAV-dLight1.3b to NAc	Measure dopamine release AUC into NAc in reponse to HFD after Veh or Dan injection at retrieval (e) and max dopamine Z-score (f)	Paired t-test	8	V: 17.0+/-3.34 D: 10.6+/-2.24	t(8) = -2.49 p = 0.0373	
Fig. 5f								V: 10.7+/-1.0 D: 8.14+/-0.78	t(8) = -2.46 p = 0.0391	
Fig. 5h					Measure dopamine release AUC into NAc in reponse to HFD after Sal or Orfo injection at retrieval (h) and max dopamine Z-score (i)		6	S: 13.5+/-3.5 O: 4.38+/-0.97	t(6) = -2.92 p = 0.0266	
Fig. 5i								S: 10.4+/-1.29 O: 6.39+/-0.3	t(6) = -2.794 p = 0.0314	
Fig. 5l	Glp1r-cre	7-8 / injection		AAV-DIO-hGLP1R to CeA and AAV-dLight1.3b to Nac	Measure dopamine release AUC into NAc in reponse to HFD after Veh or Dan injection at retrieval (l) and max dopamine (m)		7	V: 14.9+/-3.15 D: 7.53+/-1.45	t(7) = -2.47 p = 0.0425	
Fig. 5m								V: 10.3+/-1.47 D: 5.87+/-0.76	t(7) = -2.61 p = 0.0351	
Fig. 5o					Measure dopamine release AUC into NAc in reponse to HFD after Sal or Orfo injection at retrieval (o) and max dopamine (p)		6	S: 8.82+/-2.23 O: 4.85+/-2.03	t(6) = -2.46 p = 0.0493	
Fig. 5p								S: 6.67+/-1.04 O: 4.48+/-0.82	t(6) = -3.4 p = 0.0145	

Extended Figures										
Fig. 1b	Glp1r S33W and WT	11 WT / 10 S33W	Metabolic Profiling	NA	Measure diurnal rhythms and sex differences between genotypes of respiratory exchange ratio (RER) and energy expenditure (EE) Meaure baseline bodyweight and sex difference between genotypes	Two-way ANOVA w/ Bonferroni Correction	42	WT Dark: 0.87+/-0.02 Light: 0.80+/-0.02 S33W Dark: 0.85+/-0.02 Light: 0.79+/-0.03	F(3, 42) = 3.84 p = 0.0162	Dark: 0.488 Light: 0.828
Fig. 1c						Welch's t-test	17.1	WT: 0.84+/-0.02 S33W:0.82+/-0.02	t(17) = -0.45 p = 0.656	
Fig. 1d		5 WT F / 4 S33W F 7 WT M / 7 WT S33W				Two-way ANOVA w/ Bonferroni Correction	19	WT Fem: 0.84+/-0.03 Male: 0.83+/-0.02 S33W Fem: 0.81+/-0.06 Male: 0.83+/-0.02	F(3, 19) = 0.171 p = 0.9149	Fem: 0.496 Male: 0.980
Fig. 1f		11 WT / 10 S33W					42	WT Dark: 0.49+/-0.02 Light: 0.36+/-0.01 S33W Dark: 0.51+/-0.02 Light: 0.39+/-0.01	F(3, 42) = 22.64 p = <0.0001	Dark: 0.326 Light: 0.093
Fig. 1g						Welch's t-test	20.9	WT: 0.42+/-0.02 S33W:0.45+/-0.01	t(21) = 1.41 p = 0.172	
Fig. 1h		5 WT F / 4 S33W F 7 WT M / 7 WT S33W				Two-way ANOVA w/ Bonferroni Correction	19	WT Fem: 0.39+/-0.02 Male: 0.45+/-0.02 S33W Fem: 0.44+/-0.03 Male: 0.46+/-0.02	F(3,19) = 2.36 p = 0.1037	Fem: 0.100 Male: 0.692
Fig. 1i		18 WT / 19 S33W				Welch's t-test	28.1	WT: 25.1+/-1.01 S33W: 24.9+/-0.61	t(28) = -0.21 p = 0.834	
Fig. 1j		8 WT F / 9 S33W F 10 WT M / 10 S33W M				Two-way ANOVA w/ Bonferroni Correction	33	WT Fem: 22.4+/-1.24 Male: 27.3+/-1.13 S33W Fem: 23.2+/-0.61 Male: 26.4+/-0.73	F(3, 33) = 6.35 p = 0.0016	Fem: 0.583 Male: 0.492
Fig. 2a	Glp1r S33W and WT	6 WT / 6 S33W	Food Intake	Liraglutide, Danuglipron, Orforglipron, Saline, Vehicle	24 hour SD intake after GLP1RA or vehicle/saline	Two-way ANOVA w/ Bonferroni Correction	20	WT S: 4.4+/-0.11 L: 2.1+/-0.32 S33W S: 4.9+/-0.26 L: 2.7+/-0.38	F(3, 20) = 21.21 p = <0.0001	WT: <0.0001 S33W: <0.0001
Fig. 2b								WT V:4.8+/-0.35 D: 5.2+/-0.28 S33W V: 4.8+/-0.20 D: 4.8+/-0.22	F(3, 20) = 0.557 p = 0.649	WT: 0.286 S33W: 0.965
Fig. 2c								WT S:4.98+/-0.29 O: 5.9+/-0.2 S33W S: 5.4+/-0.23 O: 4.2+/-0.38	F(3, 20) = 6.38 p = 0.0033	WT: 0.032 S33W: 0.008

Fig. 3c	WT	3-4 WT / Injection	Image Analysis	Danuglipron	Oral vs. IP danuglipron and cFos in the NTS and AP	Welch's t-test	NTS: 3.1 AP: 4.6	NTS IP: 0.34+/-0.1 Oral: 0.63+/-0.2 AP IP: 0.71+/-0.36 Oral: 0.67+/-0.2	NTS: t(3) = -1.42 p = 0.2468 AP: t(5) = 0.10 p = 0.9281	
Fig. 7g	Glp1r S33W	10 / injection	Home Cage Behavior	Danuglipron and Vehicle	Percent changes in food motivated (g), drinking (h), moving (i), grooming (j), and resting (k) behaviors determined by machine learning pipeline between danuglipron or vehicle paired with HFD or SD in the inactive (light) phase	linear mixed effect model with beta regression and Tukey posthoc test	34	SD-V: 2.2+/-2.5 SD-D: 2.1+/-1.5 HFD-V: 8.5+/-3.3 HFD-D: 3.5+/-1.9	B = -3.18 p <0.0001	HFD-D/HFD-V: p = 0.0077 HFD-D/SD-V: p = 0.0114 HFD-V/SD-D: p <0.0001 HFD-V/SD-V: p <0.0001
Fig. 7h							34	SD-V: 0.2+/-0.2 SD-D: 0.1+/-0 HFD-V: 0.5+/-0.4 HFD-D: 0.1+/-0	B = -6.69 p <0.0001	HFD-D/HFD-V: p = 0.0001 HFD-V/SD-D: p <0.0001 HFD-V/SD-V: p = 0.018
Fig. 7i							34	SD-V: 6.2+/-5.7 SD-D: 1.4+/-0.5 HFD-V: 7.2+/-6 HFD-D: 3.1+/-1.5	B = -3.26 p <0.0001	HFD-V/SD-D: p = 0.0051
Fig. 7j							34	SD-V: 2.3+/-1.6 SD-D: 0.7+/-0.4 HFD-V: 2.3+/-1 HFD-D: 0.7+/-0.5	B = -4.77 p <0.0001	HFD-D/HFD-V: p = 0.0009 HFD-D/SD-V: p = 0.0047 HFD-V/SD-D: p = 0.0014 SD-V/SD-D: p = 0.0069
Fig. 7k							34	SD-V: 89+/-8.8 SD-D: 96+/-1.3 HFD-V: 82+/-6.2 HFD-D: 93+/-3.6	B = 2.44 p <0.0001	HFD-D/HFD-V: p = 0.0005 HFD-V/SD-D: p <0.0001 HFD-V/SD-V: p = 0.0013

Fig. 9b	Glp1r-Cre	7 cells	Electrophysiology	Danuglipron and AAV-DIO-hGLP1R+eYFP	Measuring changes to resting membrane potential between baseline and danuglipron administration furing electrophysiology recording session	Wilcoxon signed-rank test	6	Base: -62.72 +/-2.08 Dan: -54.87 +/-2.49	W = 28 p = 0.0156	
Fig. 10b		4 Glp1r-S33W / 8 mGlp1r / 9 hGLP1R	Food Intake	Danuglipron and Vehicle AAV-DIO-mGLP1R or mGLP1R-S33W or AAV-DIO-hGLP1R	Normailzed food intake after 4 hours for SD (b) or HFD (c) with danuglipron or vehicle	Two-way ANOVA w/ Bonferroni Correction	36	hGlp1r: V: 1.0+/-0.05 D: 0.96+/-0.13 Glp1r-S33W: V: 1.0+/-0.15 D: 0.94+/-0.04 mGlp1r: V: 1.0+/-0.09 D: 0.96+/-0.12	F(5, 36) = 0.05 p = 0.998	hGlp1r: p = 0.865 Glp1r-S33W: p = 0.752 mGlp1r: p = 0.772
Fig. 10c							36	hGlp1r: V: 1.0+/-0.08 D: 0.78+/-0.08 Glp1r-S33W: V: 1.0+/-0.16 D: 0.55+/-0.07 mGlp1r: V: 1.0+/-0.04 D: 0.90+/-0.07	F(5, 36) = 3.47 p = 0.01167	hGlp1r: p = 0.0386 Glp1r-S33W: p = 0.0061 mGlp1r: p = 0.3381
Fig. 11e		6 / injection	in vivo calcium imaging	AAV-DIO-GCaMP7s+ hGLP1R to CeA	CeA GLP1R calcium dynamics after Lira or Sal injection	Paired t-test	5	S: 10.8+/-3.03 L: 22.2+/-4.23	t(5) = 4.0 p = 0.0105	
Fig. 13b	Glp1r S33W	7 / injection	in vivo dopamine imaging	AAV-dLight1.3b to NAc	Measure dopamine release AUC into NAc in reponse to HFD after Sal or Lira injection at retrieval (b) and max dopamine Z-score (c)	Paired t-test	6	S: 13.5+/-3.5 L: 5.2+/-1.6	t(6) = -2.297 p = 0.0614	
Fig. 13c							6	S: 10.4 +/- 1.29 L: 5.82+/-0.78	t(6) = -3.01 p = 0.0238	

Supplementary Video 1 **(Isabelle Sajonia)**

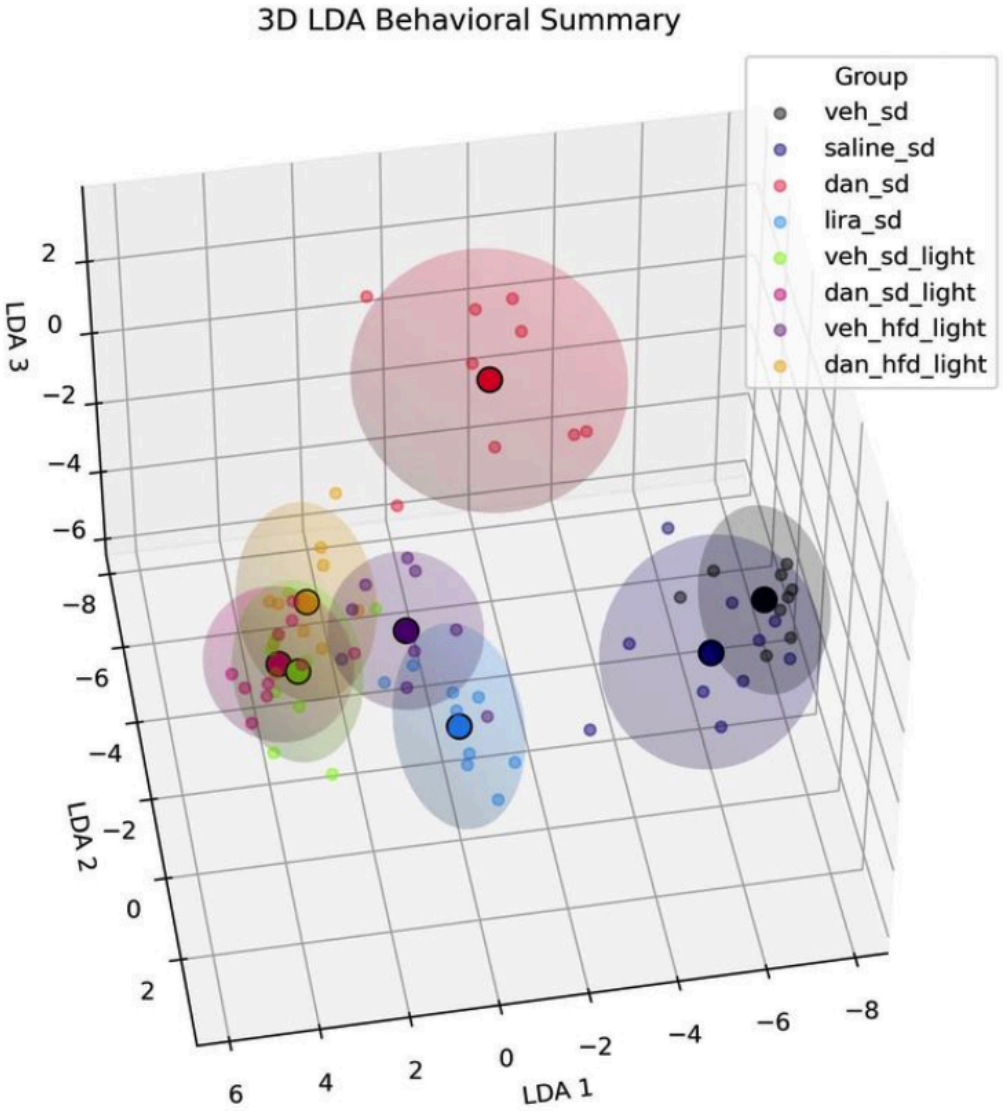

Chapter 4. Conclusions and Future Directions

C4.1 Next Generation Obesity Therapeutics

Semaglutide and tirzepatide are groundbreaking treatments for type II diabetes and obesity, paving the way for the current obesity therapeutic boom, which is projected to surpass $100 billion by 2030 (*369*). Currently, more than 50 GLP-1 receptor agonists (GLP1RAs) are in clinical trials, with that number expected to grow. Within GLP1RA treatments, multiple classes exist.

The peptide class includes liraglutide, semaglutide, tirzepatide, and CT-388, administered either daily or weekly. Notably, tirzepatide and CT-388 are dual agonists targeting both the GLP-1 receptor (GLP1R) and glucose-dependent insulinotropic polypeptide receptor (GIPR) (*370*, *371*). Survodutide (BI 456906) is the first major therapy to act as a dual glucagon and GLP-1 receptor agonist (*372*). Metsera's MET-097i is on track to become the first once-monthly injectable peptide GLP1RA. Meanwhile, antibody-based therapies like AMG 133 (MariTide) combine GLP1R agonism with GIPR antagonism (*373*), also utilizing a once-monthly injection schedule. Peptide-based therapies, however, come with challenges—they require cold storage, are costly to manufacture, and are typically limited to injectable formulations. Retatrutide, a triple agonist targeting GLP1R, GIPR, and the glucagon receptor, demonstrates up to 25% weight loss in trials and is formulated as a once-weekly injection (*374*), outperforming other agonists that typically yield ~20% weight loss.

Emerging as a promising alternative, small-molecule GLP1RAs include danuglipron, orforglipron, TERN-601, AZD5004, GSBR-1290, and GS-4571 (*318*, *321*, *322*, *375*). These molecules offer advantages such as simpler manufacturing, oral bioavailability, lower costs, and fewer food-drug interactions. While Rybelsus (oral semaglutide) is an option, it carries significant food-related restrictions. New developments include MET-224o, an oral peptide GLP1RA with

“ultra-long lasting” effects, and VRB-101, a once-weekly peptide GLP1RA pill. The fact that activating or inhibiting various incretin or glucagon pathways can produce similar weight loss results highlights the need for further mechanistic investigation.

Beyond GLP1RAs, weight loss drugs are being combined with androgen receptor modulators like enobosarm (Veru) and anti-myostatin therapeutics (Scholar Rock) to help preserve muscle mass, promoting fat loss while maintaining lean body mass (*376*). Additionally, GLP1R and amylin agonist combinations are showing promise for long-term weight loss with potentially fewer nausea-related side effects, a common drawback of obesity medications. Novo Nordisk’s semaglutide-cagrilintide combination (CagriSema) (*377*), AstraZeneca’s AZD6234, and Zealand Pharma’s petrelintide (ZP8396) (*378*) represent long-acting amylin receptor agonists in development. Metsera is also advancing a lineup of long-lasting amylin receptor agonists alongside its GLP1RA MET-097i. Meanwhile, VRB-103 is a once-weekly oral amylin receptor agonist, with additional combination oral and injectable options in development. Given their potential, amylin analogs could represent the next major class of obesity therapeutics, either as standalone treatments or in combination with incretin-based drugs.

Other innovative approaches to obesity treatment include Aardvark Therapeutics’ ARD-101 (*379*), which targets the gut bitter taste receptor (TAS2R) to stimulate the release of GLP-1, GLP-2, and CCK, promoting prolonged satiety. ARD-101 is also being investigated for monogenic obesity conditions like Prader-Willi Syndrome. Another novel strategy involves Antag’s GIPR peptide antagonist (AT-7867) (*380*), which may enhance the efficacy of traditional GLP1RAs. Preclinical studies in mice further suggest that combining GLP1R agonism with NMDA receptor antagonism (GLP-1–MK-801) can induce significant weight loss (*339*).

While GLP1R agonists remain the foundation of obesity therapy, researchers and companies

are continuously developing innovative treatment strategies. The pipeline of drug candidates is rapidly expanding, with the next generation of obesity medications likely to feature simpler oral formulations and potentially curative approaches such as targeted gene or cell therapies.

C4.2 GLP1RAs as a Panacea

Beyond their established role in type II diabetes and obesity, GLP-1 receptor agonists (GLP1RAs) are being increasingly explored for a range of other diseases, including metabolic disorders, cardiovascular conditions, neurodegenerative diseases, and even addiction treatment (*299*, *349*). These drugs are now being studied as potential treatments for metabolic dysfunction-associated steatohepatitis (MASH) and chronic kidney disease (CKD). MASH, characterized by fatty liver, inflammation, and fibrosis, can lead to severe health complications, including liver cancer, yet it currently lacks targeted treatments. GLP1RAs may offer a promising solution by reducing body fat, slowing fibrosis, lowering inflammation, and improving insulin sensitivity. Early clinical trials suggest semaglutide may resolve MASH in about 60% of cases, with further studies underway (*381*, *382*). Similarly, GLP1RAs show potential in protecting against CKD, a condition strongly linked to both type II diabetes and obesity. By improving blood glucose control, lowering blood pressure, and reducing disease progression, these drugs may help prevent or treat kidney damage. Preliminary trials indicate that liraglutide and semaglutide can prevent or reverse more than 20% of kidney damage (*383*). Additionally, because improving metabolic health and weight loss can alleviate related conditions, tirzepatide has been approved for treating obstructive sleep apnea (*384*).

GLP1RAs have also demonstrated significant cardiovascular benefits. Cardiovascular disease remains one of the leading causes of death worldwide, making effective treatment strategies crucial. These drugs help lower blood pressure, reduce the risk of heart attack and stroke, prevent plaque buildup, and improve heart failure with preserved ejection fraction (HFpEF).

Data suggests that GLP1RAs can reduce the incidence of major adverse cardiovascular events by approximately 20% in both obese and non-obese patients, positioning them as promising therapeutics for heart health (*385*–*387*).

Emerging research further suggests that GLP1RAs may offer neuroprotective, anti-inflammatory, and cognitive-enhancing effects, particularly for Alzheimer's disease (AD) and Parkinson's disease (PD). Because AD is linked to type II diabetes, improving insulin sensitivity in the brain with GLP1RAs could enhance cognitive function and slow disease progression. Early studies indicate semaglutide may mitigate neurodegeneration and AD risk in over 40% of patients who also had type II diabetes (*388*, *389*). Similarly, GLP1RAs may help slow dopaminergic neuronal loss in PD, potentially improving motor function and offering neuroprotective benefits (*390*, *391*). Although the exact mechanisms are not yet fully understood, these findings highlight the growing interest in using GLP1RAs to treat neurodegenerative diseases.

Beyond metabolic and neurodegenerative disorders, GLP1RAs are also being explored for addiction treatment (*360*, *392*, *393*). Research in both animals and humans suggests that these drugs may modulate the brain's mesolimbic dopamine system, which is responsible for motivation, reward, and addiction (*332*, *394*). By decreasing dopamine release in response to rewarding substances, GLP1RAs could help reduce cravings and improve impulse control for drugs, alcohol, and even food. While these preliminary findings are promising, more research and long-term studies are needed to fully understand their potential impact on addiction and broader brain health.

Despite their broad therapeutic potential, GLP1RAs are not without risks, and side effects can affect multiple organ systems. Gastrointestinal issues are among the most commonly reported

adverse effects, including nausea, vomiting, abdominal pain, gastroesophageal reflux disease (GERD), gastritis, and hemorrhoids (*395*). Although GLP1RAs may benefit kidney health, they have also been associated with risks such as interstitial nephritis, nephrolithiasis, and acute kidney injury. While these drugs generally have positive cardiovascular effects, they can sometimes cause hypotension (low blood pressure), which may be a concern for some patients. Gallbladder-related disorders, including cholelithiasis, cholecystitis, and biliary disease, have also been reported (*396*).

Additionally, there is concern that GLP1RAs could stimulate the growth of thyroid C cells, potentially increasing the risk of medullary thyroid cancer. Monitoring blood calcitonin levels may help mitigate this risk. Other potential complications include acute pancreatitis, which can be dangerous if left untreated, as well as bone and joint-related pain, with increased reports of arthralgia, osteoarthritis, tendonitis, and bone pain (*396*). Neurological side effects such as sleep disturbances and headaches have also been noted. Furthermore, little is known about the safety of GLP1RAs during pregnancy and breastfeeding, and as a precaution, women are advised to discontinue these medications when pregnant or nursing. Discontinuing GLP1RAs results in a significant increase in appetite, often leading to weight regain. Due to this, there remains a huge market for more curative treatments for obesity and metabolic disorders.

The potential applications of GLP1RAs continue to expand, with ongoing research uncovering new benefits across various disease areas. While these drugs have revolutionized metabolic and cardiovascular treatment, their emerging roles in neurodegeneration, addiction, and other conditions highlight their growing importance in medicine. However, as their use broadens, it remains critical to monitor their risks and long-term effects. The future of GLP1RA therapy will likely focus on optimizing targeted approaches and formulations for safety, efficacy, and accessibility while exploring novel applications beyond their current scope.

4.3 Contributions and Future Directions

Throughout this work, we have made significant contributions to the fields of circadian biology and the neurobiology of feeding and obesity treatments. While the debate over food entrainment and the anatomical location of the food-entrainable oscillator (FEO) has been ongoing, our findings confirm that the suprachiasmatic nucleus (SCN) is not heavily involved in the FEO network. Instead, we demonstrate that DMH^{Lepr} neurons play a crucial role in orchestrating food anticipatory activity and serve as a key node within the FEO network (Graphical Abstract 1). Additionally, we developed the first single-nucleus RNA sequencing atlas of the DMH, identifying transcriptional changes and pathways involved in fasting and scheduled feeding.

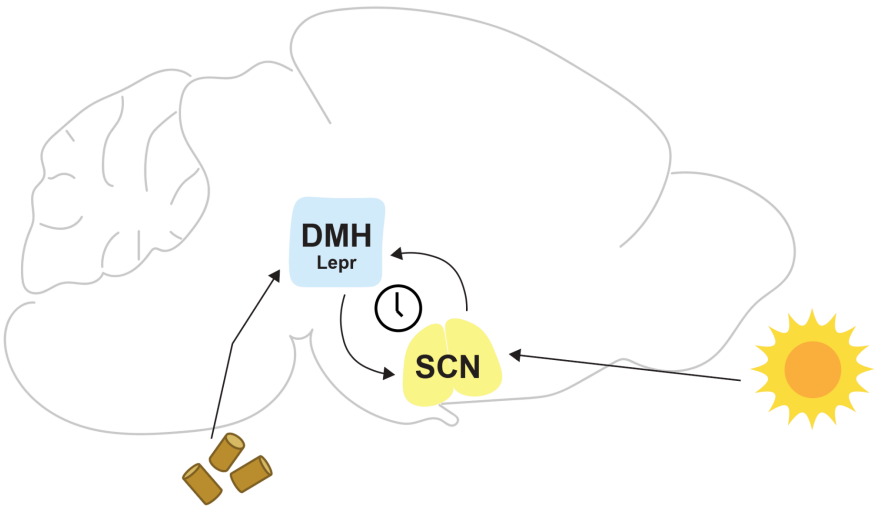

Graphical Abstract 1.

Building on this foundation, we generated a novel mouse model expressing humanized GLP1R (Glp1r^{S33W}), which will be instrumental in preclinical investigations of small-molecule GLP1R agonists. Our findings indicate that both small-molecule and peptide agonists produce comparable effects in glucose tolerance tests (GTT), feeding experiments, and behavioral patterns. To further explore the role of GLP1R in discrete neuronal populations, we engineered three new Cre-dependent AAVs encoding human GLP1R, Glp1r^{S33W}, and mGlp1r. Our results

suggest that GLP1R-expressing neurons in the hypothalamus, DMH, and hindbrain predominantly regulate homeostatic feeding, whereas GLP1R populations in the central amygdala (CeA) and hindbrain contribute to hedonic feeding (Graphical Abstract 2). Notably, we provide evidence that small-molecule GLP1R agonists can directly access brain regions traditionally considered impermeable to the blood-brain barrier, such as the CeA—an insight that could transform the way GLP1RAs are used to target and treat brain-related disorders.

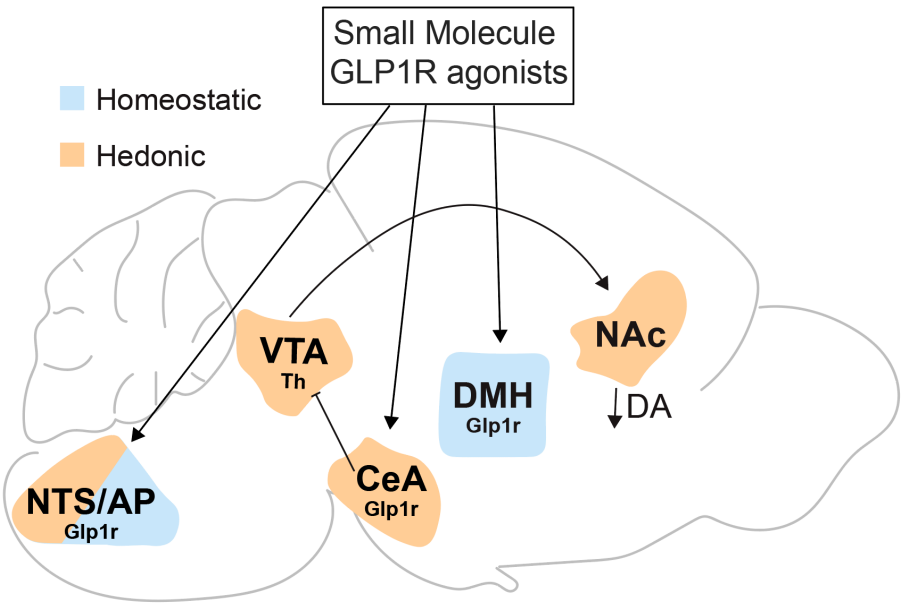

Graphical Abstract 2.

Furthermore, we identify CeA^{Glp1r} neurons as a critical component in modulating mesolimbic dopamine release in response to highly palatable foods. Our data show that both small-molecule and peptide GLP1R agonists reduce dopamine output in response to high-fat diet (HFD), an effect that is recapitulated when selectively activating CeA^{Glp1r} neurons. Collectively, this work represents a pivotal advancement in GLP1RA research, offering crucial insights into how these next-generation drugs influence physiology, behavior, and neuromodulatory networks.

There are several promising directions to build on this work. In the first project, it would be valuable to investigate how DMH^{Lepr} neurons interact with the SCN to dampen its effects. This could be explored both functionally and through snRNA-seq analysis. Additionally, understanding the broader network of circadian or locomotor-related brain regions that DMH-Lepr neurons project to could provide deeper insight into how food anticipatory activity and food entrainment are regulated in the brain.

For the second project, long-term studies are needed to assess the chronic effects of GLP1RAs, particularly in obese mice. Examining dopamine dynamics and behavioral responses to different GLP1RAs in the context of obesity could be highly informative, as obesity is both influenced by and a contributor to dysregulated dopaminergic signaling. Investigating how GLP1RAs restore “appropriate” dopamine function would provide key mechanistic insights. Additionally, monitoring VTA or CeA^{Glp1r} neuronal activity over time as animals become obese could reveal critical changes in brain function in response to caloric excess and diet-induced obesity.

This is an exciting time for metabolic disease research, with new treatments emerging each year. Expanding our fundamental understanding of how these therapies function across different organ systems is essential for optimizing their efficacy and uncovering novel therapeutic targets.

Addendum 1: Unpublished Results

Timing Effect of Liraglutide on Weight Loss and Food Consumption

Chronotherapy is an often overlooked but powerful strategy for optimizing treatment success by coordinating a person's circadian rhythm in conjunction with medical intervention (*397*). Circadian regulated pathways contribute greatly to energy metabolism in a time-of-day dependent manner. Westernized life schedules, high calorie diets, and constant access to food dysregulate circadian rhythms via interference with normal physiological processes. This circadian desynchrony, common in night-shift workers (*111–113*), is linked to obesity and metabolic disorders. Promising once-daily weight loss drugs liraglutide, danuglipron, and orforglipron are highly efficacious but GLP1RA interactions with central and peripheral circadian clock systems are unexplored. Emerging literature shows liraglutide can improve insulin secretory rhythms in pancreatic islets and increase sleep (*398*, *399*), suggesting potential diverse central and peripheral circadian effects of GLP1RAs. Understanding how GLP1RAs influence clock mechanisms to improve metabolic health could unlock improved drug targets and exciting avenues for future circadian-metabolic research.

It is well understood that mice consume a majority of their standard diet during their active phase in the dark cycle (**Fig. 1a**). If they are instead provided a highly caloric and fatty diet (HFD), they change their feeding behavior to eat almost evenly throughout their active and inactive phases and begin to gain weight (**Fig. 1b**). If HFD is restricted to the active phase, then mice do not get obese, indicating a strong circadian interaction with metabolic processes (*400*). Little is known about timing effects of GLP1RAs or if the timing of administration has an effect on efficacy or tolerability of these drugs. To test this, we first looked acutely at effects of liraglutide on hedonic feeding and bodyweight 12 to 24 hours after injection at either zeitgeber (ZT) 0 or ZT12. Though there was a similar inhibition in feeding and body weight regardless of

timing compared to saline both 12 and 24 hours after injection (**Fig 1c-f**), the ZT12 liraglutide-injected cohort lost significantly more weight than the ZT0 cohort (**Fig 1d,f**). We also found a shift toward more SD-like feeding patterns in ZT0 liraglutide-injected mice reflected by less inactive phase HFD consumption (**Fig 1g**).

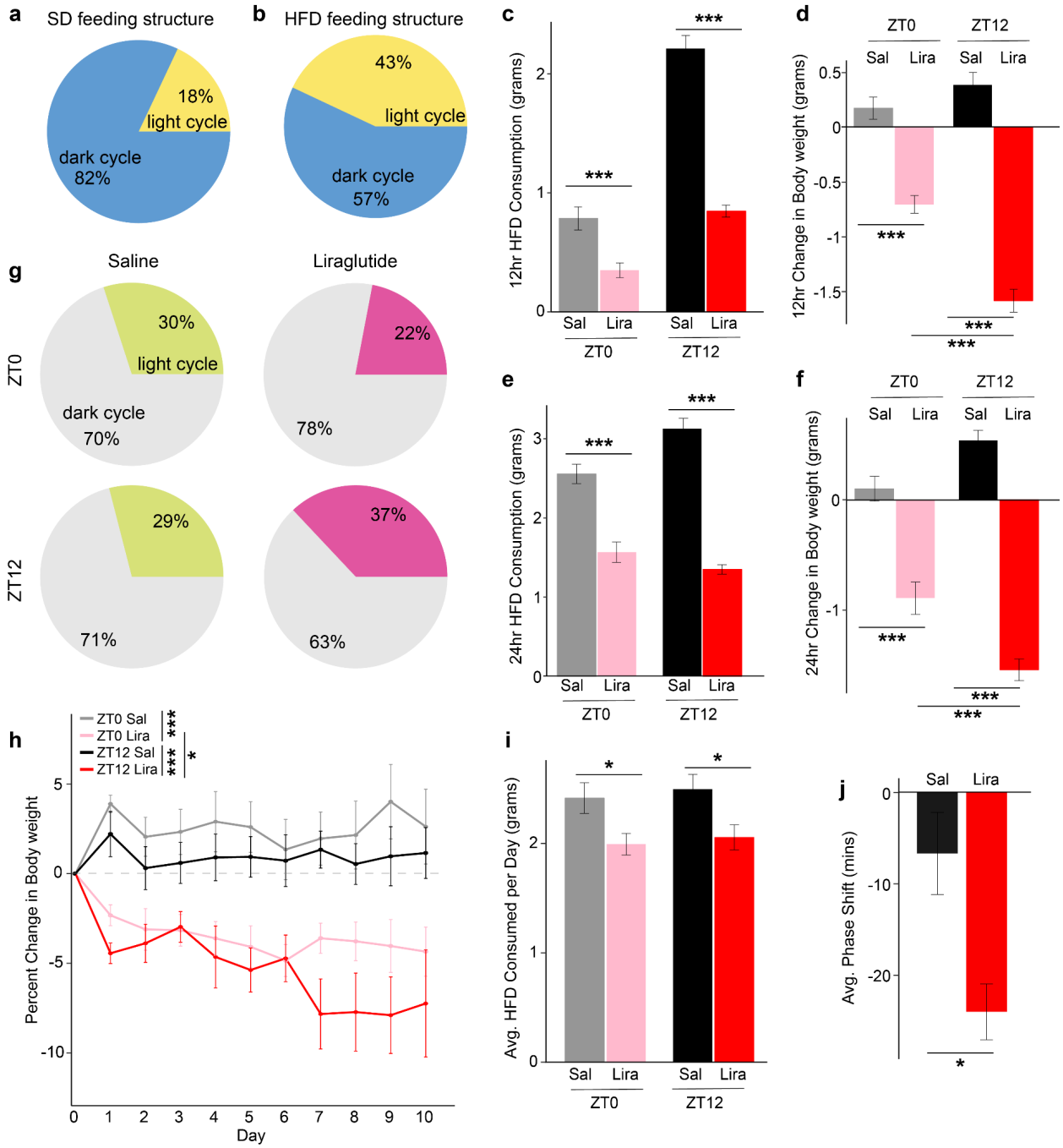

Figure 1. Acute and chronic effects of liraglutide chronotherapy on consumption and body weight. **a,b**. **(Elizabeth Godschall)** Percent of (**a**) standard diet (SD) or (**b**) high fat diet (HFD) consumed in the light or dark cycle across the 24 hour day. **c**. **(Elizabeth Godschall)** 12-hour HFD consumption after injection of liraglutide or saline at either ZT0 or ZT12 (*n* = 12 per group, Two-way ANOVA with Bonferroni Correction, ***P <0.001). **d**. **(Elizabeth Godschall)** 12-hour change in body weight after injection of liraglutide or saline at either ZT0 or ZT12 (*n* = 12 per group, Two-way ANOVA with Bonferroni Correction, ***P <0.001). **e**. **(Elizabeth Godschall)** 24-hour HFD consumption after injection of liraglutide or saline at either ZT0 or ZT12 (*n* = 12 per group, Two-way ANOVA with Bonferroni Correction, ***P <0.001). **f**.

(Elizabeth Godschall) 24-hour body weight change after injection of liraglutide or saline at either ZT0 or ZT12 (*n* = 12 per group, Two-way ANOVA with Bonferroni Correction, ***P <0.001). **g**. **(Elizabeth Godschall)** Changes in light-dark HFD feeding structure injection of liraglutide or saline at either ZT0 or ZT12. **h,i**. **(Elizabeth Godschall)** (**h**) Percent body weight change (*n* = 6 per group, Two-way ANOVA with Tukey's HSD Correction, *P <0.05; ***P <0.001) and (**i**) daily HFD intake (*n* = 6 per group, Two-way ANOVA with Bonferroni Correction, *P <0.05) of mice on chronic HFD administered liraglutide or saline at either ZT0 or ZT12 over 10 days. **j**. **(Elizabeth Godschall, Qijun Tang)** Average phase shift of mice free running in constant darkness administered saline or liraglutide at circadian time (CT) 14 (*n* = 3 per group, Welch's t-test, *P = 0.0395). Data are represented as means ± SEM.

Next, we were interested in the long term effects of liraglutide chronotherapy on weight loss and if these experiments recapitulated the acute liraglutide trends. Mice were put on a chronic HFD and treated with either saline or liraglutide at ZT0 or ZT12 for 10 days. Average HFD intake across the 10 days revealed significantly decreased consumption between liraglutide and saline groups at both ZT0 and ZT12 (**Fig. 1i**). Average body weight was significantly decreased in liraglutide ZT0 or ZT12-injected groups compared to saline cohorts (**Fig. 1h**). Interestingly, we found the most drastic weight loss effect in the ZT12 liraglutide-injected cohort (**Fig. 1h)**. These findings indicate liraglutide could be optimal for weight loss when administered at the onset of the active phase, supporting an interplay between circadian mechanisms and GLP1RA treatment to enhance metabolism and treatment outcome.

SCN Expresses GLP1R and is Activated by Liraglutide

While the effects of liraglutide on the circadian system are evident from our previous experiments, we next wanted to understand if liraglutide could alter the central circadian pacemaker, the suprachiasmatic nucleus (SCN). While some comprehensive studies have indicated the SCN as a liraglutide responsive region (*305*, *401*, *402*), the effects of liraglutide on the SCN have never been explored.

First, we asked if liraglutide can shift or alter the circadian clock through perturbations in the free

running period of mice. Preliminary experiments suggest that liraglutide injection to mice in constant darkness (DD) at circadian time (CT) 14 induces a significant phase delay (**Fig. 1j**). These findings highlight a potential role for liraglutide in modulating the central circadian pacemaker. Next, we looked to the SCN to understand if this interaction could be direct or indirect. In order for liraglutide to exert direct effects on the SCN, it is first essential to know if the SCN expresses GLP1R. Using single nuclei RNA-sequencing we identified Glp1r mRNA transcripts in the SCN (**Fig. 2a-c**), validated by RNA *in situ* hybridization along with a Glp1r-Cre;tdTomato reporter mouse line to verify protein expression (**Fig. 2d,e**). We find that SCN^{Glp1r} cells appear in both the shell and core of the SCN and do not highly coexpress with other known SCN subtypes (**Fig. 2e**). This SCN^{Glp1r} population provides an interesting research avenue into the intersection of feeding, metabolism, and circadian research, warranting further investigation.

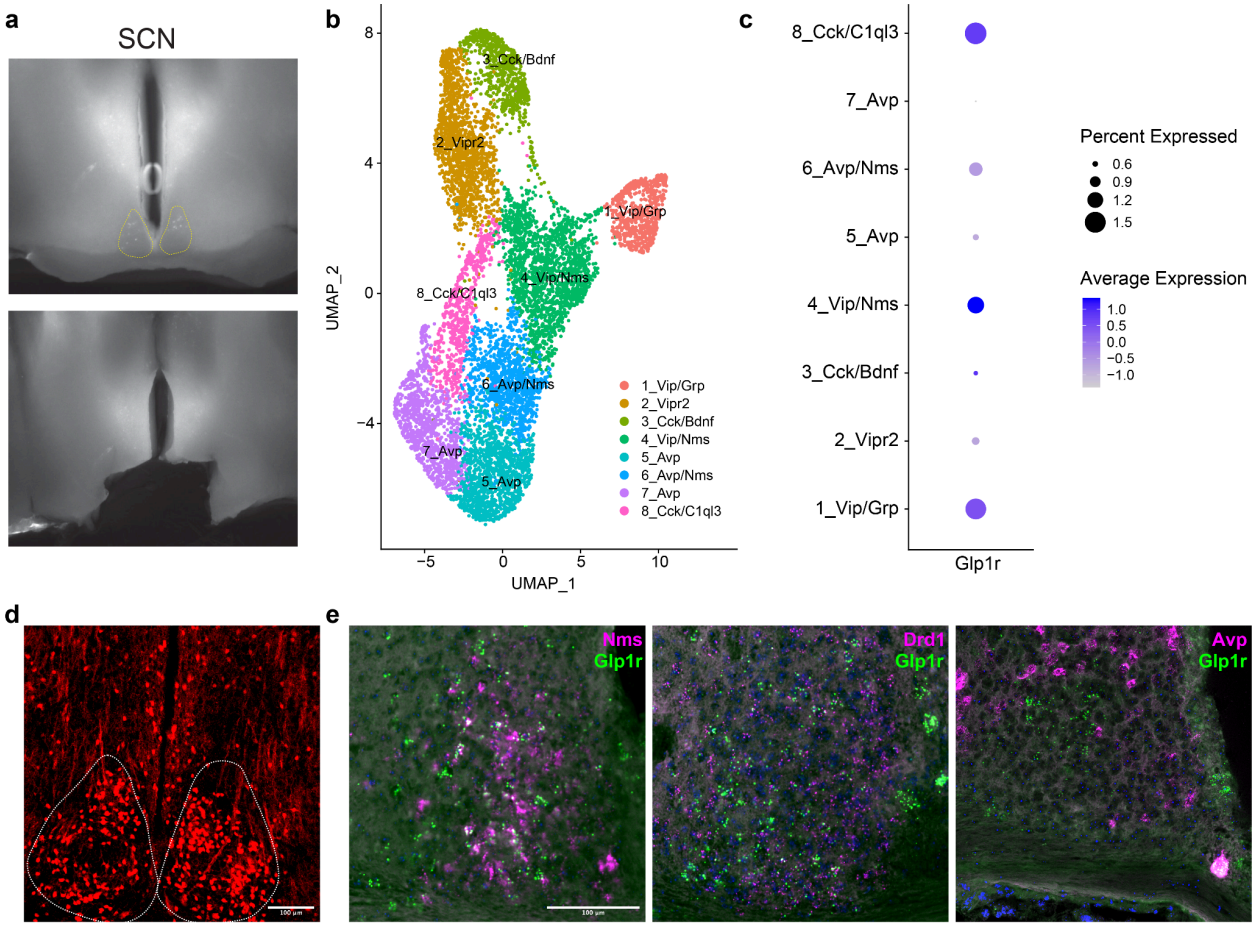

Figure 2. Glp1r is expressed in the SCN and is a distinctive subtype. a. **(Elizabeth Godschall)** Representative microdissection of tissue extracted from the SCN for single nuclei RNA-sequencing. **b**. **(Elizabeth Godschall)** Uniform Manifold Approximation and Projection (UMAP) of the SCN and its 8 neuronal clusters. **c**. **(Elizabeth Godschall)** Dot plot showing which SCN clusters Glp1r mRNA is colocalized with. Dot size indicates percent expression and dot color indicates average Glp1r expression. **d**. **(Elizabeth Godschall)** Glp1r-Cre;tdTomato expression in the SCN shown in red. Scale bar = 100 µm. **e**. **(Elizabeth Godschall)** RNA *in situ* hybridization of Glp1r (green) with either Nms (magenta; left), Drd1 (magenta; middle), or Avp (magenta; right) in the SCN. Scale bar = 100 µm.

References

1. M. Michel, Editorial: comparative studies of energy homeostasis in vertebrates. *Front Endocrinol (Lausanne)*. **9**, 291 (2018).
2. R. Covian, L. Edwards, Y. He, G. Kim, C. Houghton, R. L. Levine, R. S. Balaban, Energy homeostasis is a conserved process: Evidence from Paracoccus denitrificans' response to acute changes in energy demand. *PLoS ONE*. **16**, e0259636 (2021).
3. V. J. Clemente-Suárez, A. I. Beltrán-Velasco, L. Redondo-Flórez, A. Martín-Rodríguez, J. F. Tornero-Aguilera, Global impacts of western diet and its effects on metabolism and health: A narrative review. *Nutrients*. **15** (2023), doi:10.3390/nu15122749.
4. M. Askari, J. Heshmati, H. Shahinfar, N. Tripathi, E. Daneshzad, Ultra-processed food and the risk of overweight and obesity: a systematic review and meta-analysis of observational studies. *Int J Obes (Lond)*. **44**, 2080–2091 (2020).
5. K. D. Hall, A. Ayuketah, R. Brychta, H. Cai, T. Cassimatis, K. Y. Chen, S. T. Chung, E. Costa, A. Courville, V. Darcey, L. A. Fletcher, C. G. Forde, A. M. Gharib, J. Guo, R. Howard, P. V. Joseph, S. McGehee, R. Ouwerkerk, K. Raisinger, I. Rozga, M. Zhou, Ultra-Processed Diets Cause Excess Calorie Intake and Weight Gain: An Inpatient Randomized Controlled Trial of Ad Libitum Food Intake. *Cell Metab.* **30**, 67-77.e3 (2019).
6. Adult Obesity Facts | Obesity | CDC, (available at https://www.cdc.gov/obesity/adult-obesity-facts/index.html).
7. N. R. Lenard, H.-R. Berthoud, Central and peripheral regulation of food intake and physical activity: pathways and genes. *Obesity (Silver Spring)*. **16 Suppl 3**, S11-22 (2008).
8. M. Camilleri, Peripheral mechanisms in appetite regulation. *Gastroenterology*. **148**, 1219–1233 (2015).
9. A. Abizaid, T. L. Horvath, Ghrelin and the central regulation of feeding and energy balance. *Indian J. Endocrinol. Metab.* **16**, S617-26 (2012).
10. E. Deloose, W. Verbeure, I. Depoortere, J. Tack, Motilin: from gastric motility stimulation to hunger signalling. *Nat. Rev. Endocrinol.* **15**, 238–250 (2019).
11. D. A. Sandoval, D. A. D'Alessio, Physiology of proglucagon peptides: role of glucagon and GLP-1 in health and disease. *Physiol. Rev.* **95**, 513–548 (2015).
12. L. L. Baggio, D. J. Drucker, Biology of incretins: GLP-1 and GIP. *Gastroenterology*. **132**, 2131–2157 (2007).
13. R. A. Lafferty, F. P. M. O'Harte, N. Irwin, V. A. Gault, P. R. Flatt, Proglucagon-Derived Peptides as Therapeutics. *Front Endocrinol (Lausanne)*. **12**, 689678 (2021).
14. T. Forst, C. De Block, S. Del Prato, S. Armani, J. Frias, A. Lautenbach, B. Ludvik, M. Marinez, C. Mathieu, T. D. Müller, O. Schnell, The role of incretin receptor agonists in the treatment of obesity. *Diabetes Obes. Metab.* **26**, 4178–4196 (2024).

15. D. J. Drucker, The GLP-1 journey: from discovery science to therapeutic impact. *The Journal of Clinical Investigation* (2024).

16. K. Simpson, J. Parker, J. Plumer, S. Bloom, CCK, PYY and PP: the control of energy balance. *Handb. Exp. Pharmacol.*, 209–230 (2012).

17. J. M. Yabut, J. D. Crane, A. E. Green, D. J. Keating, W. I. Khan, G. R. Steinberg, Emerging roles for serotonin in regulating metabolism: new implications for an ancient molecule. *Endocr. Rev.* **40**, 1092–1107 (2019).

18. P. V. Röder, B. Wu, Y. Liu, W. Han, Pancreatic regulation of glucose homeostasis. *Exp. Mol. Med.* **48**, e219 (2016).

19. G. Katsuura, A. Asakawa, A. Inui, Roles of pancreatic polypeptide in regulation of food intake. *Peptides*. **23**, 323–329 (2002).

20. J. M. Friedman, Leptin and the endocrine control of energy balance. *Nat. Metab.* **1**, 754–764 (2019).

21. J. Friedman, 20 years of leptin: leptin at 20: an overview. *J. Endocrinol.* **223**, T1-8 (2014).

22. H. L. Tan, L. Yin, Y. Tan, J. Ivanov, K. Plucinska, A. Ilanges, B. R. Herb, P. Wang, C. Kosse, P. Cohen, D. Lin, J. M. Friedman, Leptin-activated hypothalamic BNC2 neurons acutely suppress food intake. *Nature*. **636**, 198–205 (2024).

23. A. Sahu, Leptin signaling in the hypothalamus: emphasis on energy homeostasis and leptin resistance. *Front. Neuroendocrinol.* **24**, 225–253 (2003).

24. A. Yadav, M. A. Kataria, V. Saini, A. Yadav, Role of leptin and adiponectin in insulin resistance. *Clin. Chim. Acta*. **417**, 80–84 (2013).

25. B. Lee, J. Shao, Adiponectin and lipid metabolism in skeletal muscle. *Acta Pharmaceutica Sinica B*. **2**, 335–340 (2012).

26. X. Hui, P. Gu, J. Zhang, T. Nie, Y. Pan, D. Wu, T. Feng, C. Zhong, Y. Wang, K. S. L. Lam, A. Xu, Adiponectin Enhances Cold-Induced Browning of Subcutaneous Adipose Tissue via Promoting M2 Macrophage Proliferation. *Cell Metab.* **22**, 279–290 (2015).

27. D. Porte, Central regulation of energy homeostasis: the key role of insulin. *Diabetes*. **55**, S155–S160 (2006).

28. G. Williams, J. A. Harrold, D. J. Cutler, The hypothalamus and the regulation of energy homeostasis: lifting the lid on a black box. *Proc. Nutr. Soc.* **59**, 385–396 (2000).

29. H. J. Grill, M. R. Hayes, Hindbrain neurons as an essential hub in the neuroanatomically distributed control of energy balance. *Cell Metab.* **16**, 296–309 (2012).

30. E. Gropp, M. Shanabrough, E. Borok, A. W. Xu, R. Janoschek, T. Buch, L. Plum, N. Balthasar, B. Hampel, A. Waisman, G. S. Barsh, T. L. Horvath, J. C. Brüning, Agouti-related peptide-expressing neurons are mandatory for feeding. *Nat. Neurosci.* **8**, 1289–1291 (2005).

31. J. D. Deem, C. L. Faber, G. J. Morton, AgRP neurons: Regulators of feeding, energy

expenditure, and behavior. *FEBS J.* **289**, 2362–2381 (2022).

32. J. N. Campbell, E. Z. Macosko, H. Fenselau, T. H. Pers, A. Lyubetskaya, D. Tenen, M. Goldman, A. M. J. Verstegen, J. M. Resch, S. A. McCarroll, E. D. Rosen, B. B. Lowell, L. T. Tsai, A molecular census of arcuate hypothalamus and median eminence cell types. *Nat. Neurosci.* **20**, 484–496 (2017).

33. N. Biglari, I. Gaziano, J. Schumacher, J. Radermacher, L. Paeger, P. Klemm, W. Chen, S. Corneliussen, C. M. Wunderlich, M. Sue, S. Vollmar, T. Klöckener, T. Sotelo-Hitschfeld, A. Abbasloo, F. Edenhofer, F. Reimann, F. M. Gribble, H. Fenselau, P. Kloppenburg, F. T. Wunderlich, J. C. Brüning, Functionally distinct POMC-expressing neuron subpopulations in hypothalamus revealed by intersectional targeting. *Nat. Neurosci.* **24**, 913–929 (2021).

34. W. Cheng, E. Ndoka, C. Hutch, K. Roelofs, A. MacKinnon, B. Khoury, J. Magrisso, K. S. Kim, C. J. Rhodes, D. P. Olson, R. J. Seeley, D. Sandoval, M. G. Myers, Leptin receptor-expressing nucleus tractus solitarius neurons suppress food intake independently of GLP1 in mice. *JCI Insight*. **5** (2020), doi:10.1172/jci.insight.134359.

35. D. I. Brierley, M. K. Holt, A. Singh, A. de Araujo, M. McDougle, M. Vergara, M. H. Afaghani, S. J. Lee, K. Scott, C. Maske, W. Langhans, E. Krause, A. de Kloet, F. M. Gribble, F. Reimann, L. Rinaman, G. de Lartigue, S. Trapp, Central and peripheral GLP-1 systems independently suppress eating. *Nat. Metab.* **3**, 258–273 (2021).

36. W. Qiu, C. R. Hutch, Y. Wang, J. Wloszek, R. A. Rucker, M. G. Myers, D. Sandoval, Multiple NTS neuron populations cumulatively suppress food intake. *eLife*. **12** (2023), doi:10.7554/eLife.85640.

37. C. W. Roman, S. R. Sloat, R. D. Palmiter, A tale of two circuits: CCKNTS neuron stimulation controls appetite and induces opposing motivational states by projections to distinct brain regions. *Neuroscience*. **358**, 316–324 (2017).

38. J. Chen, M. Cheng, L. Wang, L. Zhang, D. Xu, P. Cao, F. Wang, H. Herzog, S. Song, C. Zhan, A Vagal-NTS Neural Pathway that Stimulates Feeding. *Curr. Biol.* **30**, 3986-3998.e5 (2020).

39. K. A. van Galen, K. W. Ter Horst, M. J. Serlie, Serotonin, food intake, and obesity. *Obes. Rev.* **22**, e13210 (2021).

40. K. Nonogaki, The regulatory role of the central and peripheral serotonin network on feeding signals in metabolic diseases. *Int. J. Mol. Sci.* **23** (2022), doi:10.3390/ijms23031600.

41. I. Aklan, N. Sayar-Atasoy, F. Deng, H. Kim, Y. Yavuz, J. Rysted, C. Laule, D. Davis, Y. Li, D. Atasoy, Dorsal raphe serotonergic neurons suppress feeding through redundant forebrain circuits. *Mol. Metab.* **69**, 101676 (2023).

42. Y. Han, G. Xia, D. Srisai, F. Meng, Y. He, Y. Ran, Y. He, M. Farias, G. Hoang, I. Tóth, M. O. Dietrich, M.-H. Chen, Y. Xu, Q. Wu, Deciphering an AgRP-serotoninergic neural circuit in distinct control of energy metabolism from feeding. *Nat. Commun.* **12**, 3525 (2021).

43. I. Morales, K. C. Berridge, “Liking” and “wanting” in eating and food reward: Brain mechanisms and clinical implications. *Physiol. Behav.* **227**, 113152 (2020).

44. M. K. Estes, J. J. Bland, K. K. Ector, M. J. Puppa, D. W. Powell, D. B. Lester, A high fat western diet attenuates phasic dopamine release. *Neurosci. Lett.* **756**, 135952 (2021).

45. S. Valdivia, A. Patrone, M. Reynaldo, M. Perello, Acute high fat diet consumption activates the mesolimbic circuit and requires orexin signaling in a mouse model. *PLoS ONE*. **9**, e87478 (2014).

46. C. A. Siciliano, M. J. Ferris, S. R. Jones, Cocaine self-administration disrupts mesolimbic dopamine circuit function and attenuates dopaminergic responsiveness to cocaine. *Eur. J. Neurosci.* **42**, 2091–2096 (2015).

47. J. T. Yorgason, D. M. Hedges, J. D. Obray, E. Y. Jang, K. B. Bills, M. Woodbury, B. Williams, M. J. Parsons, M. A. Andres, S. C. Steffensen, Methamphetamine increases dopamine release in the nucleus accumbens through calcium-dependent processes. *Psychopharmacology (Berl)*. **237**, 1317–1330 (2020).

48. J. D. Salamone, M. Correa, The mysterious motivational functions of mesolimbic dopamine. *Neuron*. **76**, 470–485 (2012).

49. G. Aston-Jones, R. J. Smith, G. C. Sartor, D. E. Moorman, L. Massi, P. Tahsili-Fahadan, K. A. Richardson, Lateral hypothalamic orexin/hypocretin neurons: A role in reward-seeking and addiction. *Brain Res.* **1314**, 74–90 (2010).

50. K. Toshinai, Y. Date, N. Murakami, M. Shimada, M. S. Mondal, T. Shimbara, J.-L. Guan, Q.-P. Wang, H. Funahashi, T. Sakurai, S. Shioda, S. Matsukura, K. Kangawa, M. Nakazato, Ghrelin-induced food intake is mediated via the orexin pathway. *Endocrinology*. **144**, 1506–1512 (2003).

51. M. A. Katzman, M. P. Katzman, Neurobiology of the orexin system and its potential role in the regulation of hedonic tone. *Brain Sci.* **12** (2022), doi:10.3390/brainsci12020150.

52. F. Barrile, D. Cassano, G. Fernandez, P. N. De Francesco, M. Reynaldo, S. Cantel, J.-A. Fehrentz, J. Donato, H. B. Schiöth, J. M. Zigman, M. Perello, Ghrelin’s orexigenic action in the lateral hypothalamic area involves indirect recruitment of orexin neurons and arcuate nucleus activation. *Psychoneuroendocrinology*. **156**, 106333 (2023).

53. F. Zamanirad, M. Fattahi, H. Amirteymori, Z. Mousavi, A. Haghparast, The role of orexin-1 receptors within the ventral tegmental area in the extinction and reinstatement of methamphetamine place preference. *Behav. Brain Res.* **453**, 114608 (2023).

54. G. Aston-Jones, R. J. Smith, D. E. Moorman, K. A. Richardson, Role of lateral hypothalamic orexin neurons in reward processing and addiction. *Neuropharmacology*. **56 Suppl 1**, 112–121 (2009).

55. C. S. Thomas, A. Mohammadkhani, M. Rana, M. Qiao, C. Baimel, S. L. Borgland, Optogenetic stimulation of lateral hypothalamic orexin/dynorphin inputs in the ventral tegmental area potentiates mesolimbic dopamine neurotransmission and promotes reward-seeking behaviours. *Neuropsychopharmacology*. **47**, 728–740 (2022).

56. J. M. Wenzel, J. F. Cheer, Endocannabinoid Regulation of Reward and Reinforcement through Interaction with Dopamine and Endogenous Opioid Signaling. *Neuropsychopharmacology*. **43**, 103–115 (2018).

57. M. Solinas, S. Yasar, S. R. Goldberg, Endocannabinoid system involvement in brain reward processes related to drug abuse. *Pharmacol. Res.* **56**, 393–405 (2007).

58. L. H. Parsons, Y. L. Hurd, Endocannabinoid signalling in reward and addiction. *Nat. Rev. Neurosci.* **16**, 579–594 (2015).

59. C. Ravinet Trillou, C. Delgorge, C. Menet, M. Arnone, P. Soubrié, CB1 cannabinoid receptor knockout in mice leads to leanness, resistance to diet-induced obesity and enhanced leptin sensitivity. *Int. J. Obes. Relat. Metab. Disord.* **28**, 640–648 (2004).

60. J. L. Wiley, J. J. Burston, D. C. Leggett, O. O. Alekseeva, R. K. Razdan, A. Mahadevan, B. R. Martin, CB1 cannabinoid receptor-mediated modulation of food intake in mice. *Br. J. Pharmacol.* **145**, 293–300 (2005).

61. C. M. Friemel, A. Zimmer, M. Schneider, The CB1 receptor as an important mediator of hedonic reward processing. *Neuropsychopharmacology*. **39**, 2387–2396 (2014).

62. M. H. Brodermann, Pain, pleasure and placebo: the cannabinoids in reward processing and the perception of pain. *Ment. Health Addict. Res.* **1** (2016), doi:10.15761/MHAR.1000115.

63. C. S. Pittendrigh, S. Daan, A functional analysis of circadian pacemakers in nocturnal rodents. *J. Comp. Physiol.* **106**, 223–252 (1976).

64. K. P. Wright, A. W. McHill, B. R. Birks, B. R. Griffin, T. Rusterholz, E. D. Chinoy, Entrainment of the human circadian clock to the natural light-dark cycle. *Curr. Biol.* **23**, 1554–1558 (2013).

65. L. Pickel, H.-K. Sung, Feeding rhythms and the circadian regulation of metabolism. *Front. Nutr.* **7**, 39 (2020).

66. J. M. Hurley, J. J. Loros, J. C. Dunlap, Circadian Oscillators: Around the Transcription-Translation Feedback Loop and on to Output. *Trends Biochem. Sci.* **41**, 834–846 (2016).

67. N. Gekakis, D. Staknis, H. B. Nguyen, F. C. Davis, L. D. Wilsbacher, D. P. King, J. S. Takahashi, C. J. Weitz, Role of the CLOCK protein in the mammalian circadian mechanism. *Science*. **280**, 1564–1569 (1998).

68. Y. O. Abe, H. Yoshitane, D. W. Kim, S. Kawakami, M. Koebis, K. Nakao, A. Aiba, J. K. Kim, Y. Fukada, Rhythmic transcription of Bmal1 stabilizes the circadian timekeeping system in mammals. *Nat. Commun.* **13**, 4652 (2022).

69. I. Kwon, J. Lee, S. H. Chang, N. C. Jung, B. J. Lee, G. H. Son, K. Kim, K. H. Lee, BMAL1 shuttling controls transactivation and degradation of the CLOCK/BMAL1 heterodimer. *Mol. Cell. Biol.* **26**, 7318–7330 (2006).

70. J. S. Takahashi, Transcriptional architecture of the mammalian circadian clock. *Nat. Rev. Genet.* **18**, 164–179 (2017).

71. M. H. Hastings, M. Brancaccio, E. S. Maywood, Circadian pacemaking in cells and circuits of the suprachiasmatic nucleus. *J. Neuroendocrinol.* **26**, 2–10 (2014).

72. C. C. Petersen, F. Cao, A. R. Stinchcombe, R. E. Mistlberger, Multiple entrained oscillator model of food anticipatory circadian rhythms. *Sci. Rep.* **12**, 9306 (2022).

73. D. F. Patton, R. E. Mistlberger, Circadian adaptations to meal timing: neuroendocrine mechanisms. *Front. Neurosci.* **7**, 185 (2013).

74. R. E. Mistlberger, Neurobiology of food anticipatory circadian rhythms. *Physiol. Behav.* **104**, 535–545 (2011).

75. K.-F. Storch, C. J. Weitz, Daily rhythms of food-anticipatory behavioral activity do not require the known circadian clock. *Proc Natl Acad Sci USA*. **106**, 6808–6813 (2009).

76. J. S. Pendergast, S. Yamazaki, The Mysterious Food-Entrainable Oscillator: Insights from Mutant and Engineered Mouse Models. *J. Biol. Rhythms*. **33**, 458–474 (2018).

77. K. A. Stokkan, S. Yamazaki, H. Tei, Y. Sakaki, M. Menaker, Entrainment of the circadian clock in the liver by feeding. *Science*. **291**, 490–493 (2001).

78. A. J. Davidson, A. S. Poole, S. Yamazaki, M. Menaker, Is the food-entrainable circadian oscillator in the digestive system? *Genes Brain Behav.* **2**, 32–39 (2003).

79. P. Crosby, R. Hamnett, M. Putker, N. P. Hoyle, M. Reed, C. J. Karam, E. S. Maywood, A. Stangherlin, J. E. Chesham, E. A. Hayter, L. Rosenbrier-Ribeiro, P. Newham, H. Clevers, D. A. Bechtold, J. S. O'Neill, Insulin/IGF-1 Drives PERIOD Synthesis to Entrain Circadian Rhythms with Feeding Time. *Cell*. **177**, 896-909.e20 (2019).

80. Q. Tang, E. Godschall, C. D. Brennan, Q. Zhang, R.-J. Abraham-Fan, S. P. Williams, T. B. Güngül, R. Onoharigho, A. Buyukaksakal, R. Salinas, J. J. Olivieri, C. D. Deppmann, J. N. Campbell, B. Podyma, A. D. Güler, A leptin-responsive hypothalamic circuit inputs to the circadian feeding network. *BioRxiv* (2023), doi:10.1101/2023.02.24.529901.

81. S.-H. Yoo, S. Yamazaki, P. L. Lowrey, K. Shimomura, C. H. Ko, E. D. Buhr, S. M. Siepka, H.-K. Hong, W. J. Oh, O. J. Yoo, M. Menaker, J. S. Takahashi, PERIOD2::LUCIFERASE real-time reporting of circadian dynamics reveals persistent circadian oscillations in mouse peripheral tissues. *Proc Natl Acad Sci USA*. **101**, 5339–5346 (2004).

82. R. Chavan, C. Feillet, S. S. F. Costa, J. E. Delorme, T. Okabe, J. A. Ripperger, U. Albrecht, Liver-derived ketone bodies are necessary for food anticipation. *Nat. Commun.* **7**, 10580 (2016).

83. S. Chen, M. Feng, S. Zhang, Z. Dong, Y. Wang, W. Zhang, C. Liu, Angptl8 mediates food-driven resetting of hepatic circadian clock in mice. *Nat. Commun.* **10**, 3518 (2019).

84. J. LeSauter, N. Hoque, M. Weintraub, D. W. Pfaff, R. Silver, Stomach ghrelin-secreting cells as food-entrainable circadian clocks. *Proc Natl Acad Sci USA*. **106**, 13582–13587 (2009).

85. T. P. Vahl, D. L. Drazen, R. J. Seeley, D. A. D'Alessio, S. C. Woods, Meal-anticipatory glucagon-like peptide-1 secretion in rats. *Endocrinology*. **151**, 569–575 (2010).

86. D. L. Williams, Expecting to eat: glucagon-like peptide-1 and the anticipation of meals.

Endocrinology. **151**, 445–447 (2010).

87. M. Hastings, J. S. O'Neill, E. S. Maywood, Circadian clocks: regulators of endocrine and metabolic rhythms. *J. Endocrinol.* **195**, 187–198 (2007).

88. E. Poggiogalle, H. Jamshed, C. M. Peterson, Circadian regulation of glucose, lipid, and energy metabolism in humans. *Metab. Clin. Exp.* **84**, 11–27 (2018).

89. I. D. Blum, E. W. Lamont, T. Rodrigues, A. Abizaid, Isolating neural correlates of the pacemaker for food anticipation. *PLoS ONE*. **7**, e36117 (2012).

90. M. F. Wiater, A.-J. Li, T. T. Dinh, H. T. Jansen, S. Ritter, Leptin-sensitive neurons in the arcuate nucleus integrate activity and temperature circadian rhythms and anticipatory responses to food restriction. *Am. J. Physiol. Regul. Integr. Comp. Physiol.* **305**, R949-60 (2013).

91. Q. Tang, E. Godschall, C. D. Brennan, Q. Zhang, R.-J. Abraham-Fan, S. P. Williams, T. B. Güngül, R. Onoharigho, A. Buyukaksakal, R. Salinas, I. R. Sajonia, J. J. Olivieri, O. Y. Calhan, C. D. Deppmann, J. N. Campbell, B. Podyma, A. D. Güler, Leptin receptor neurons in the dorsomedial hypothalamus input to the circadian feeding network. *Sci. Adv.* **9**, eadh9570 (2023).

92. T. Kuo, thesis, UNIVERSITY OF CALIFORNIA, SAN FRANCISCO Approved: (2019).

93. J. J. Gooley, A. Schomer, C. B. Saper, The dorsomedial hypothalamic nucleus is critical for the expression of food-entrainable circadian rhythms. *Nat. Neurosci.* **9**, 398–407 (2006).

94. M. Mieda, S. C. Williams, J. A. Richardson, K. Tanaka, M. Yanagisawa, The dorsomedial hypothalamic nucleus as a putative food-entrainable circadian pacemaker. *Proc Natl Acad Sci USA*. **103**, 12150–12155 (2006).

95. G. J. Landry, G. R. Yamakawa, I. C. Webb, R. J. Mear, R. E. Mistlberger, The dorsomedial hypothalamic nucleus is not necessary for the expression of circadian food-anticipatory activity in rats. *J. Biol. Rhythms*. **22**, 467–478 (2007).

96. G. J. Landry, M. M. Simon, I. C. Webb, R. E. Mistlberger, Persistence of a behavioral food-anticipatory circadian rhythm following dorsomedial hypothalamic ablation in rats. *Am. J. Physiol. Regul. Integr. Comp. Physiol.* **290**, R1527-34 (2006).

97. T. Moriya, R. Aida, T. Kudo, M. Akiyama, M. Doi, N. Hayasaka, N. Nakahata, R. Mistlberger, H. Okamura, S. Shibata, The dorsomedial hypothalamic nucleus is not necessary for food-anticipatory circadian rhythms of behavior, temperature or clock gene expression in mice. *Eur. J. Neurosci.* **29**, 1447–1460 (2009).

98. P. Domenech, E. Koechlin, Executive control and decision-making in the prefrontal cortex. *Curr. Opin. Behav. Sci.* **1**, 101–106 (2015).

99. A. N. Santiago, E. A. Makowicz, M. Du, C. Aoki, Food Restriction Engages Prefrontal Corticostriatal Cells and Local Microcircuitry to Drive the Decision to Run versus Conserve Energy. *Cereb. Cortex*. **31**, 2868–2885 (2021).

100. F. T. Gallo, M. B. Zanoni Saad, A. Silva, J. F. Morici, M. Miranda, M. C. Anderson, N. V.

Weisstaub, P. Bekinschtein, Dopamine modulates adaptive forgetting in medial prefrontal cortex. *J. Neurosci.* **42**, 6620–6636 (2022).

101. B. T. S. Carneiro, J. F. Araujo, The food-entrainable oscillator: a network of interconnected brain structures entrained by humoral signals? *Chronobiol. Int.* **26**, 1273–1289 (2009).

102. H.-R. Berthoud, H. Münzberg, C. D. Morrison, Blaming the brain for obesity: integration of hedonic and homeostatic mechanisms. *Gastroenterology*. **152**, 1728–1738 (2017).

103. Overweight and Obesity - Causes and Risk Factors | NHLBI, NIH, (available at https://www.nhlbi.nih.gov/health/overweight-and-obesity/causes).

104. H. Wu, C. M. Ballantyne, Metabolic inflammation and insulin resistance in obesity. *Circ. Res.* **126**, 1549–1564 (2020).

105. T. Kawai, M. V. Autieri, R. Scalia, Adipose tissue inflammation and metabolic dysfunction in obesity. *Am J Physiol, Cell Physiol*. **320**, C375–C391 (2021).

106. Z. Weijie, Z. Meng, W. Chunxiao, M. Lingjie, Z. Anguo, Z. Yan, C. Xinran, X. Yanjiao, S. Li, Obesity-induced chronic low-grade inflammation in adipose tissue: A pathway to Alzheimer's disease. *Ageing Res. Rev.* **99**, 102402 (2024).

107. M. S. Ellulu, I. Patimah, H. Khaza'ai, A. Rahmat, Y. Abed, Obesity and inflammation: the linking mechanism and the complications. *Arch. Med. Sci.* **13**, 851–863 (2017).

108. D. Khanna, S. Khanna, P. Khanna, P. Kahar, B. M. Patel, Obesity: A Chronic Low-Grade Inflammation and Its Markers. *Cureus*. **14**, e22711 (2022).

109. B. H. Ahn, M. Kim, S.-Y. Kim, Brain circuits for promoting homeostatic and non-homeostatic appetites. *Exp. Mol. Med.* **54**, 349–357 (2022).

110. M. Lutter, E. J. Nestler, Homeostatic and hedonic signals interact in the regulation of food intake. *J. Nutr.* **139**, 629–632 (2009).

111. G. Hulsegge, K. I. Proper, B. Loef, H. Paagman, J. R. Anema, W. van Mechelen, The mediating role of lifestyle in the relationship between shift work, obesity and diabetes. *Int. Arch. Occup. Environ. Health*. **94**, 1287–1295 (2021).

112. Q. Zhang, S. Y. Chair, S. H. S. Lo, J. P.-C. Chau, M. Schwade, X. Zhao, Association between shift work and obesity among nurses: A systematic review and meta-analysis. *Int. J. Nurs. Stud.* **112**, 103757 (2020).

113. V. M. O'Brien, F. M. Nea, L. K. Pourshahidi, M. B. E. Livingstone, L. Bardon, C. Kelly, J. M. Kearney, C. A. Corish, Overweight and obesity in shift workers: associated dietary and lifestyle factors. *Eur. J. Public Health*. **30**, 579–584 (2020).

114. J. A. J. Martyn, M. Kaneki, S. Yasuhara, Obesity-induced insulin resistance and hyperglycemia: etiologic factors and molecular mechanisms. *Anesthesiology*. **109**, 137–148 (2008).

115. U. Hoffler, K. Hobbie, R. Wilson, R. Bai, A. Rahman, D. Malarkey, G. Travlos, B. I. Ghanayem, Diet-induced obesity is associated with hyperleptinemia, hyperinsulinemia, hepatic steatosis, and glomerulopathy in C57Bl/6J mice. *Endocrine*. **36**, 311–325 (2009).

116. A. M. Y. Zhang, E. A. Wellberg, J. L. Kopp, J. D. Johnson, Hyperinsulinemia in obesity, inflammation, and cancer. *Diabetes Metab. J.* **45**, 285–311 (2021).

117. D. Pretz, C. Le Foll, M. Z. Rizwan, T. A. Lutz, A. Tups, Hyperleptinemia as a contributing factor for the impairment of glucose intolerance in obesity. *FASEB J.* **35**, e21216 (2021).

118. R. Kumar, K. Mal, M. K. Razaq, M. Magsi, M. K. Memon, S. Memon, M. N. Afroz, H. F. Siddiqui, A. Rizwan, Association of leptin with obesity and insulin resistance. *Cureus*. **12**, e12178 (2020).

119. H. E. Bays, C. Kirkpatrick, K. C. Maki, P. P. Toth, R. T. Morgan, J. Tondt, S. M. Christensen, D. Dixon, T. A. Jacobson, Obesity, dyslipidemia, and cardiovascular disease: A joint expert review from the obesity medicine association and the National Lipid Association 2024. *Obesity Pillars*, 100108 (2024).

120. B. Klop, J. W. F. Elte, M. C. Cabezas, Dyslipidemia in obesity: mechanisms and potential targets. *Nutrients*. **5**, 1218–1240 (2013).

121. M. Obradovic, E. Sudar-Milovanovic, S. Soskic, M. Essack, S. Arya, A. J. Stewart, T. Gojobori, E. R. Isenovic, Leptin and obesity: role and clinical implication. *Front Endocrinol (Lausanne)*. **12**, 585887 (2021).

122. J. Sripetchwandee, N. Chattipakorn, S. C. Chattipakorn, Links Between Obesity-Induced Brain Insulin Resistance, Brain Mitochondrial Dysfunction, and Dementia. *Front Endocrinol (Lausanne)*. **9**, 496 (2018).

123. A. C. Incollingo Rodriguez, E. S. Epel, M. L. White, E. C. Standen, J. R. Seckl, A. J. Tomiyama, Hypothalamic-pituitary-adrenal axis dysregulation and cortisol activity in obesity: A systematic review. *Psychoneuroendocrinology*. **62**, 301–318 (2015).

124. J. A. Whitworth, P. M. Williamson, G. Mangos, J. J. Kelly, Cardiovascular consequences of cortisol excess. *Vasc. Health Risk Manag.* **1**, 291–299 (2005).

125. H. K. Karlsson, L. Tuominen, S. Helin, P. Salminen, P. Nuutila, L. Nummenmaa, Mesolimbic opioid-dopamine interaction is disrupted in obesity but recovered by weight loss following bariatric surgery. *Transl. Psychiatry*. **11**, 259 (2021).

126. R. G. Boswell, M. N. Potenza, C. M. Grilo, The Neurobiology of Binge-eating Disorder Compared with Obesity: Implications for Differential Therapeutics. *Clin. Ther.* **43**, 50–69 (2021).

127. M. B. Parent, S. Higgs, L. G. Cheke, S. E. Kanoski, Memory and eating: A bidirectional relationship implicated in obesity. *Neurosci. Biobehav. Rev.* **132**, 110–129 (2022).

128. A. K. Fitch, S. Malhotra, R. Conroy, Differentiating monogenic and syndromic obesities from polygenic obesity: Assessment, diagnosis, and management. *Obes. Pillars*. **11**, 100110 (2024).

129. K. M. Fock, J. Khoo, Diet and exercise in management of obesity and overweight. *J. Gastroenterol. Hepatol.* **28 Suppl 4**, 59–63 (2013).

130. K. D. Brownell, J. Rodin, Medical, metabolic, and psychological effects of weight cycling. *Arch. Intern. Med.* **154**, 1325–1330 (1994).

131. I. N. Love, Thyroid extract in juvenile obesity: a clinical note. *JAMA*. **XXXIV**, 975 (1900).

132. T. D. Müller, C. Clemmensen, B. Finan, R. D. DiMarchi, M. H. Tschöp, Anti-Obesity Therapy: from Rainbow Pills to Polyagonists. *Pharmacol. Rev.* **70**, 712–746 (2018).

133. M. L. Tainter, A. B. Stockton, W. C. Cutting, Use of dinitrophenol in obesity and related conditions. *JAMA*. **101**, 1472 (1933).

134. W. C. Cutting, H. G. Mehrtens, M. L. Tainter, Actions and uses of dinitrophenol. *JAMA*. **101**, 193 (1933).

135. Public health weekly reports for OCTOBER 24, 1919. *Public Health Rep.* **34**, 2335–2430 (1919).

136. J. Grundlingh, P. I. Dargan, M. El-Zanfaly, D. M. Wood, 2,4-dinitrophenol (DNP): a weight loss agent with significant acute toxicity and risk of death. *J. Med. Toxicol.* **7**, 205–212 (2011).

137. S. J. Kish, Pharmacologic mechanisms of crystal meth. *CMAJ*. **178**, 1679–1682 (2008).

138. D.-Y. Kuo, S.-F. Yang, S.-C. Chu, S.-C. Chu, C.-H. Chen, Y.-S. Hsieh, Amphetamine-evoked changes of oxidative stress and neuropeptide Y gene expression in hypothalamus: regulation by the protein kinase C-delta signaling. *Chem. Biol. Interact.* **180**, 193–201 (2009).

139. S.-C. Chu, P.-N. Chen, Y.-S. Hsieh, C.-H. Yu, M.-H. Lin, Y.-H. Lin, D.-Y. Kuo, Involvement of hypothalamic PI3K-STAT3 signalling in regulating appetite suppression mediated by amphetamine. *Br. J. Pharmacol.* **171**, 3223–3233 (2014).

140. T. Zheng, L. Liu, J. Shi, X. Yu, W. Xiao, R. Sun, Y. Zhou, J. Aa, G. Wang, The metabolic impact of methamphetamine on the systemic metabolism of rats and potential markers of methamphetamine abuse. *Mol. Biosyst.* **10**, 1968–1977 (2014).

141. R. K. Jan, R. R. Kydd, B. R. Russell, Functional and structural brain changes associated with methamphetamine abuse. *Brain Sci.* **2**, 434–482 (2012).

142. S. Moeller, H. B. Huttner, T. Struffert, H. H. Müller, Irreversible brain damage caused by methamphetamine. *Alcoholism and Drug Addiction*. **29**, 39–41 (2016).

143. T. D. Müller, M. Blüher, M. H. Tschöp, R. D. DiMarchi, Anti-obesity drug discovery: advances and challenges. *Nat. Rev. Drug Discov.* **21**, 201–223 (2022).

144. E. Colman, Anorectics on trial: a half century of federal regulation of prescription appetite suppressants. *Ann. Intern. Med.* **143**, 380–385 (2005).

145. P. A. Cohen, A. Goday, J. P. Swann, The return of rainbow diet pills. *Am. J. Public Health*. **102**, 1676–1686 (2012).

146. N. T. Bello, N.-C. Liang, The use of serotonergic drugs to treat obesity--is there any hope? *Drug Des. Devel. Ther.* **5**, 95–109 (2011).

147. K. Conde, S. Fang, Y. Xu, Unraveling the serotonin saga: from discovery to weight regulation and beyond - a comprehensive scientific review. *Cell Biosci.* **13**, 143 (2023).

148. R. S. Stafford, D. C. Radley, National trends in antiobesity medication use. *Arch. Intern.*

Med. **163**, 1046–1050 (2003).

149. R. M. Pinder, R. N. Brogden, P. R. Sawyer, T. M. Speight, G. S. Avery, Fenfluramine: a review of its pharmacological properties and therapeutic efficacy in obesity. *Drugs*. **10**, 241–323 (1975).

150. R. Davis, D. Faulds, Dexfenfluramine. An updated review of its therapeutic use in the management of obesity. *Drugs*. **52**, 696–724 (1996).

151. D. E. Arterburn, P. K. Crane, D. L. Veenstra, The efficacy and safety of sibutramine for weight loss: a systematic review. *Arch. Intern. Med.* **164**, 994–1003 (2004).

152. L. K. Heisler, E. E. Jobst, G. M. Sutton, L. Zhou, E. Borok, Z. Thornton-Jones, H. Y. Liu, J. M. Zigman, N. Balthasar, T. Kishi, C. E. Lee, C. J. Aschkenasi, C.-Y. Zhang, J. Yu, O. Boss, K. G. Mountjoy, P. G. Clifton, B. B. Lowell, J. M. Friedman, T. Horvath, M. A. Cowley, Serotonin reciprocally regulates melanocortin neurons to modulate food intake. *Neuron*. **51**, 239–249 (2006).

153. J. C. G. Halford, J. A. Harrold, E. J. Boyland, C. L. Lawton, J. E. Blundell, Serotonergic drugs : effects on appetite expression and use for the treatment of obesity. *Drugs*. **67**, 27–55 (2007).

154. T. A. Wadden, R. I. Berkowitz, F. Silvestry, R. A. Vogt, M. G. St John Sutton, A. J. Stunkard, G. D. Foster, J. L. Aber, The fen-phen finale: a study of weight loss and valvular heart disease. *Obes. Res.* **6**, 278–284 (1998).

155. S. R. Smith, N. J. Weissman, C. M. Anderson, M. Sanchez, E. Chuang, S. Stubbe, H. Bays, W. R. Shanahan, Behavioral Modification and Lorcaserin for Overweight and Obesity Management (BLOOM) Study Group, Multicenter, placebo-controlled trial of lorcaserin for weight management. *N. Engl. J. Med.* **363**, 245–256 (2010).

156. L. M. Zeltser, Distinct hypothalamic and brainstem contributions to lorcaserin action. *Cell Metab.* **28**, 533–534 (2018).

157. P. De Deurwaerdère, M. Ramos, R. Bharatiya, E. Puginier, A. Chagraoui, J. Manem, E. Cuboni, M. Pierucci, G. Deidda, M. Casarrubea, G. Di Giovanni, Lorcaserin bidirectionally regulates dopaminergic function site-dependently and disrupts dopamine brain area correlations in rats. *Neuropharmacology*. **166**, 107915 (2020).

158. E. A. Bohula, S. D. Wiviott, D. K. McGuire, S. E. Inzucchi, J. Kuder, K. Im, C. L. Fanola, A. Qamar, C. Brown, A. Budaj, A. Garcia-Castillo, M. Gupta, L. A. Leiter, N. J. Weissman, H. D. White, T. Patel, B. Francis, W. Miao, C. Perdomo, S. Dhadda, CAMELLIA–TIMI 61 Steering Committee and Investigators, Cardiovascular safety of lorcaserin in overweight or obese patients. *N. Engl. J. Med.* **379**, 1107–1117 (2018).

159. S. M. Smith, M. Meyer, K. E. Trinkley, Phentermine/topiramate for the treatment of obesity. *Ann. Pharmacother.* **47**, 340–349 (2013).

160. A. Ballinger, Orlistat in the treatment of obesity. *Expert Opin. Pharmacother.* **1**, 841–847 (2000).

161. F. X. Pi-Sunyer, L. J. Aronne, H. M. Heshmati, J. Devin, J. Rosenstock, RIO-North

America Study Group, Effect of rimonabant, a cannabinoid-1 receptor blocker, on weight and cardiometabolic risk factors in overweight or obese patients: RIO-North America: a randomized controlled trial. *JAMA*. **295**, 761–775 (2006).

162. J.-P. Després, A. Golay, L. Sjöström, Rimonabant in Obesity-Lipids Study Group, Effects of rimonabant on metabolic risk factors in overweight patients with dyslipidemia. *N. Engl. J. Med.* **353**, 2121–2134 (2005).

163. T. Ugur, M. Bartels, B. Kis, N. Scherbaum, Psychosis following anti-obesity treatment with rimonabant. *Obes. Facts*. **1**, 103–105 (2008).

164. F. L. Greenway, K. Fujioka, R. A. Plodkowski, S. Mudaliar, M. Guttadauria, J. Erickson, D. D. Kim, E. Dunayevich, COR-I Study Group, Effect of naltrexone plus bupropion on weight loss in overweight and obese adults (COR-I): a multicentre, randomised, double-blind, placebo-controlled, phase 3 trial. *Lancet*. **376**, 595–605 (2010).

165. S. K. Billes, P. Sinnayah, M. A. Cowley, Naltrexone/bupropion for obesity: an investigational combination pharmacotherapy for weight loss. *Pharmacol. Res.* **84**, 1–11 (2014).

166. G.-J. Wang, J. Zhao, D. Tomasi, E. S. Kojori, R. Wang, C. E. Wiers, E. C. Caparelli, N. D. Volkow, Effect of combined naltrexone and bupropion therapy on the brain's functional connectivity. *Int J Obes (Lond)*. **42**, 1890–1899 (2018).

167. J. M. Friedman, The discovery and development of GLP-1 based drugs that have revolutionized the treatment of obesity. *Proc Natl Acad Sci USA*. **121**, e2415550121 (2024).

168. S. Mojsov, G. Heinrich, I. B. Wilson, M. Ravazzola, L. Orci, J. F. Habener, Preproglucagon gene expression in pancreas and intestine diversifies at the level of post-translational processing. *J. Biol. Chem.* **261**, 11880–11889 (1986).

169. P. K. Lund, R. H. Goodman, P. C. Dee, J. F. Habener, Pancreatic preproglucagon cDNA contains two glucagon-related coding sequences arranged in tandem. *Proc Natl Acad Sci USA*. **79**, 345–349 (1982).

170. J. Eng, Exendin peptides. *Mt Sinai J Med*. **59**, 147–149 (1992).

171. J. Eng, W. A. Kleinman, L. Singh, G. Singh, J. P. Raufman, Isolation and characterization of exendin-4, an exendin-3 analogue, from Heloderma suspectum venom. Further evidence for an exendin receptor on dispersed acini from guinea pig pancreas. *J. Biol. Chem.* **267**, 7402–7405 (1992).

172. D. Tang, H. Tian, J. Wu, J. Cheng, C. Luo, W. Sai, X. Song, X. Gao, W. Yao, C-terminal site-specific PEGylated Exendin-4 analog: A long-acting glucagon like Peptide-1 receptor agonist, on glycemic control and beta cell function in diabetic db/db mice. *J. Pharmacol. Sci.* **138**, 23–30 (2018).

173. M. Briones, M. Bajaj, Exenatide: a GLP-1 receptor agonist as novel therapy for Type 2 diabetes mellitus. *Expert Opin. Pharmacother.* **7**, 1055–1064 (2006).

174. J. Dushay, C. Gao, G. S. Gopalakrishnan, M. Crawley, E. K. Mitten, E. Wilker, J.

Mullington, E. Maratos-Flier, Short-term exenatide treatment leads to significant weight loss in a subset of obese women without diabetes. *Diabetes Care*. **35**, 4–11 (2012).

175. S. P. Marso, G. H. Daniels, K. Brown-Frandsen, P. Kristensen, J. F. Mann, M. A. Nauck, S. E. Nissen, S. Pocock, N. R. Poulter, L. S. Ravn, W. M. Steinberg, M. Stockner, B. Zinman, R. M. Bergenstal, J. B. Buse, LEADER Steering Committee, LEADER Trial Investigators, Liraglutide and Cardiovascular Outcomes in Type 2 Diabetes. *N. Engl. J. Med.* **375**, 311–322 (2016).

176. J. van Can, B. Sloth, C. B. Jensen, A. Flint, E. E. Blaak, W. H. M. Saris, Effects of the once-daily GLP-1 analog liraglutide on gastric emptying, glycemic parameters, appetite and energy metabolism in obese, non-diabetic adults. *Int J Obes (Lond)*. **38**, 784–793 (2014).

177. X. Pi-Sunyer, A. Astrup, K. Fujioka, F. Greenway, A. Halpern, M. Krempf, D. C. W. Lau, C. W. le Roux, R. Violante Ortiz, C. B. Jensen, J. P. H. Wilding, SCALE Obesity and Prediabetes NN8022-1839 Study Group, A randomized, controlled trial of 3.0 mg of liraglutide in weight management. *N. Engl. J. Med.* **373**, 11–22 (2015).

178. B. Bode, Liraglutide: a review of the first once-daily GLP-1 receptor agonist. *Am. J. Manag. Care*. **17**, S59-70 (2011).

179. S. P. Marso, S. C. Bain, A. Consoli, F. G. Eliaschewitz, E. Jódar, L. A. Leiter, I. Lingvay, J. Rosenstock, J. Seufert, M. L. Warren, V. Woo, O. Hansen, A. G. Holst, J. Pettersson, T. Vilsbøll, SUSTAIN-6 Investigators, Semaglutide and Cardiovascular Outcomes in Patients with Type 2 Diabetes. *N. Engl. J. Med.* **375**, 1834–1844 (2016).

180. J. P. H. Wilding, R. L. Batterham, S. Calanna, M. Davies, L. F. Van Gaal, I. Lingvay, B. M. McGowan, J. Rosenstock, M. T. D. Tran, T. A. Wadden, S. Wharton, K. Yokote, N. Zeuthen, R. F. Kushner, STEP 1 Study Group, Once-Weekly Semaglutide in Adults with Overweight or Obesity. *N. Engl. J. Med.* **384**, 989–1002 (2021).

181. C. De Block, C. Bailey, C. Wysham, A. Hemmingway, S. E. Allen, J. Peleshok, Tirzepatide for the treatment of adults with type 2 diabetes: An endocrine perspective. *Diabetes Obes. Metab.* **25**, 3–17 (2023).

182. A. M. Jastreboff, L. J. Aronne, N. N. Ahmad, S. Wharton, L. Connery, B. Alves, A. Kiyosue, S. Zhang, B. Liu, M. C. Bunck, A. Stefanski, SURMOUNT-1 Investigators, Tirzepatide once weekly for the treatment of obesity. *N. Engl. J. Med.* **387**, 205–216 (2022).

183. L. J. Aronne, N. Sattar, D. B. Horn, H. E. Bays, S. Wharton, W.-Y. Lin, N. N. Ahmad, S. Zhang, R. Liao, M. C. Bunck, I. Jouravskaya, M. A. Murphy, SURMOUNT-4 Investigators, Continued Treatment With Tirzepatide for Maintenance of Weight Reduction in Adults With Obesity: The SURMOUNT-4 Randomized Clinical Trial. *JAMA*. **331**, 38–48 (2024).

184. P. J. Rodriguez, B. M. Goodwin Cartwright, S. Gratzl, R. Brar, C. Baker, T. J. Gluckman, N. L. Stucky, Semaglutide vs tirzepatide for weight loss in adults with overweight or obesity. *JAMA Intern. Med.* **184**, 1056–1064 (2024).

185. B. Rader, R. Hazan, J. S. Brownstein, Changes in adult obesity trends in the US. *JAMA Health Forum*. **5**, e243685 (2024).

186. Authors, C. Vannabouathong, C. Crotty, K. Le, D. Eurich, P. Dyrda, *Current Utilization Patterns of Glucagon-Like Peptide-1 Receptor Agonists: Report* (Canadian Agency for Drugs and Technologies in Health, Ottawa (ON), 2022), *CADTH health technology review*.

187. E. Harris, Poll: Roughly 12% of US Adults Have Used a GLP-1 Drug, Even If Unaffordable. *JAMA*. **332**, 8 (2024).

188. A. M. Angelidi, M. J. Belanger, A. Kokkinos, C. C. Koliaki, C. S. Mantzoros, Novel noninvasive approaches to the treatment of obesity: from pharmacotherapy to gene therapy. *Endocr. Rev.* **43**, 507–557 (2022).

189. J. S. El-Sayed Moustafa, P. Froguel, From obesity genetics to the future of personalized obesity therapy. *Nat. Rev. Endocrinol.* **9**, 402–413 (2013).

190. I. Mohammed, B. Haris, T. Al-Barazenji, D. Vasudeva, S. Tomei, I. Al Azwani, H. Dauleh, S. Shehzad, S. Chirayath, G. Mohamadsalih, G. Petrovski, A. Khalifa, D. R. Love, M. Al-Shafai, K. Hussain, Understanding the Genetics of Early-Onset Obesity in a Cohort of Children From Qatar. *J. Clin. Endocrinol. Metab.* **108**, 3201–3213 (2023).

191. C. A. Meehan, E. Cochran, A. Kassai, R. J. Brown, P. Gorden, Metreleptin for injection to treat the complications of leptin deficiency in patients with congenital or acquired generalized lipodystrophy. *Expert Rev. Clin. Pharmacol.* **9**, 59–68 (2016).

192. C. Chaves, T. Kay, J. Anselmo, Early onset obesity due to a mutation in the human leptin receptor gene. *Endocrinol. Diabetes Metab. Case Rep.* **2022** (2022), doi:10.1530/EDM-21-0124.

193. H. Krude, H. Biebermann, W. Luck, R. Horn, G. Brabant, A. Grüters, Severe early-onset obesity, adrenal insufficiency and red hair pigmentation caused by POMC mutations in humans. *Nat. Genet.* **19**, 155–157 (1998).

194. K. L. Ayers, B. S. Glicksberg, A. S. Garfield, S. Longerich, J. A. White, P. Yang, L. Du, T. W. Chittenden, J. R. Gulcher, S. Roy, F. Fiedorek, K. Gottesdiener, S. Cohen, K. E. North, E. E. Schadt, S. D. Li, R. Chen, L. H. T. Van der Ploeg, Melanocortin 4 receptor pathway dysfunction in obesity: patient stratification aimed at MC4R agonist treatment. *J. Clin. Endocrinol. Metab.* **103**, 2601–2612 (2018).

195. C. Vaisse, K. Clement, E. Durand, S. Hercberg, B. Guy-Grand, P. Froguel, Melanocortin-4 receptor mutations are a frequent and heterogeneous cause of morbid obesity. *J. Clin. Invest.* **106**, 253–262 (2000).

196. P. Kühnen, K. Clément, S. Wiegand, O. Blankenstein, K. Gottesdiener, L. L. Martini, K. Mai, U. Blume-Peytavi, A. Grüters, H. Krude, Proopiomelanocortin Deficiency Treated with a Melanocortin-4 Receptor Agonist. *N. Engl. J. Med.* **375**, 240–246 (2016).

197. R. J. F. Loos, G. S. H. Yeo, The genetics of obesity: from discovery to biology. *Nat. Rev. Genet.* **23**, 120–133 (2022).

198. R. Mahmoud, V. Kimonis, M. G. Butler, Genetics of obesity in humans: A clinical review. *Int. J. Mol. Sci.* **23** (2022), doi:10.3390/ijms231911005.

199. Y. Kaur, R. J. de Souza, W. T. Gibson, D. Meyre, A systematic review of genetic syndromes with obesity. *Obes. Rev.* **18**, 603–634 (2017).

200. Office of the Surgeon General (US), Background on Obesity (2010).

201. J. S. White, Straight talk about high-fructose corn syrup: what it is and what it ain't. *Am. J. Clin. Nutr.* **88**, 1716S-1721S (2008).

202. G. A. Bray, S. J. Nielsen, B. M. Popkin, Consumption of high-fructose corn syrup in beverages may play a role in the epidemic of obesity. *Am. J. Clin. Nutr.* **79**, 537–543 (2004).

203. M. E. Bocarsly, E. S. Powell, N. M. Avena, B. G. Hoebel, High-fructose corn syrup causes characteristics of obesity in rats: increased body weight, body fat and triglyceride levels. *Pharmacol. Biochem. Behav.* **97**, 101–106 (2010).

204. A. Mohammadbeigi, A. Asgarian, E. Moshir, H. Heidari, S. Afrashteh, S. Khazaei, H. Ansari, Fast food consumption and overweight/obesity prevalence in students and its association with general and abdominal obesity. *J. Prev. Med. Hyg.* **59**, E236–E240 (2018).

205. G. R. Faria, A brief history of bariatric surgery. *Porto Biomedical Journal*. **2**, 90–92 (2017).

206. E. E. Mason, C. Ito, Gastric bypass in obesity. *Surg. Clin. North Am.* **47**, 1345–1351 (1967).

207. D. E. Arterburn, D. A. Telem, R. F. Kushner, A. P. Courcoulas, Benefits and risks of bariatric surgery in adults: A review. *JAMA*. **324**, 879–887 (2020).

208. Types of Weight-loss Surgery - NIDDK, (available at https://www.niddk.nih.gov/health-information/weight-management/bariatric-surgery/types).

209. B. Doble, S. Wordsworth, C. A. Rogers, R. Welbourn, J. Byrne, J. M. Blazeby, By-Band-Sleeve Trial Management Group, What are the real procedural costs of bariatric surgery? A systematic literature review of published cost analyses. *Obes. Surg.* **27**, 2179–2192 (2017).

210. R. Lim, A. Beekley, D. C. Johnson, K. A. Davis, Early and late complications of bariatric operation. *Trauma Surg. Acute Care Open*. **3**, e000219 (2018).

211. M. Ramadan, M. Loureiro, K. Laughlan, R. Caiazzo, A. Iannelli, L. Brunaud, S. Czernichow, M. Nedelcu, D. Nocca, Risk of Dumping Syndrome after Sleeve Gastrectomy and Roux-en-Y Gastric Bypass: Early Results of a Multicentre Prospective Study. *Gastroenterol. Res. Pract.* **2016**, 2570237 (2016).

212. J. S. Garrow, G. T. Gardiner, Maintenance of weight loss in obese patients after jaw wiring. *Br Med J (Clin Res Ed)*. **282**, 858–860 (1981).

213. S. Rodgers, R. Burnet, A. Goss, P. Phillips, R. Goldney, C. Kimber, D. Thomas, P.

Harding, P. Wise, Jaw wiring in treatment of obesity. *Lancet*. **1**, 1221–1222 (1977).

214. P. Castelnuovo-Tedesco, D. C. Buchanan, H. David Hall, Jaw-wiring for obesity. *Gen. Hosp. Psychiatry*. **2**, 156–159 (1980).

215. K. D. Hall, J. Guo, Obesity energetics: body weight regulation and the effects of diet composition. *Gastroenterology*. **152**, 1718-1727.e3 (2017).

216. R. Dalle Grave, M. Sartirana, S. Calugi, Personalized cognitive-behavioural therapy for obesity (CBT-OB): theory, strategies and procedures. *Biopsychosoc. Med.* **14**, 5 (2020).

217. M. Laudenslager, Z. W. Chaudhry, S. Rajagopal, S. Clynes, K. A. Gudzune, Commercial weight loss programs in the management of obesity: an update. *Curr. Obes. Rep.* **10**, 90–99 (2021).

218. T. Fang, H. Cao, Y. Wang, Y. Gong, Z. Wang, Global Scientific Trends on Healthy Eating from 2002 to 2021: A Bibliometric and Visualized Analysis. *Nutrients*. **15** (2023), doi:10.3390/nu15061461.

219. M. Kamiński, K. Skonieczna-Żydecka, J. K. Nowak, E. Stachowska, Global and local diet popularity rankings, their secular trends, and seasonal variation in Google Trends data. *Nutrition*. **79–80**, 110759 (2020).

220. A. Pan, E. S. Schernhammer, Q. Sun, F. B. Hu, Rotating night shift work and risk of type 2 diabetes: two prospective cohort studies in women. *PLoS Med.* **8**, e1001141 (2011).

221. I. Z. Zimberg, S. A. Fernandes Junior, C. A. Crispim, S. Tufik, M. T. de Mello, Metabolic impact of shift work. *Work*. **41 Suppl 1**, 4376–4383 (2012).

222. J. D. Johnston, J. M. Ordovás, F. A. Scheer, F. W. Turek, Circadian rhythms, metabolism, and chrononutrition in rodents and humans. *Adv. Nutr.* **7**, 399–406 (2016).

223. D. M. Arble, J. Bass, A. D. Laposky, M. H. Vitaterna, F. W. Turek, Circadian timing of food intake contributes to weight gain. *Obesity (Silver Spring)*. **17**, 2100–2102 (2009).

224. M. Hatori, C. Vollmers, A. Zarrinpar, L. DiTacchio, E. A. Bushong, S. Gill, M. Leblanc, A. Chaix, M. Joens, J. A. J. Fitzpatrick, M. H. Ellisman, S. Panda, Time-restricted feeding without reducing caloric intake prevents metabolic diseases in mice fed a high-fat diet. *Cell Metab.* **15**, 848–860 (2012).

225. E. F. Sutton, R. Beyl, K. S. Early, W. T. Cefalu, E. Ravussin, C. M. Peterson, Early Time-Restricted Feeding Improves Insulin Sensitivity, Blood Pressure, and Oxidative Stress Even without Weight Loss in Men with Prediabetes. *Cell Metab.* **27**, 1212-1221.e3 (2018).

226. S. Cienfuegos, K. Gabel, F. Kalam, M. Ezpeleta, E. Wiseman, V. Pavlou, S. Lin, M. L. Oliveira, K. A. Varady, Effects of 4- and 6-h Time-Restricted Feeding on Weight and Cardiometabolic Health: A Randomized Controlled Trial in Adults with Obesity. *Cell Metab.* **32**, 366-378.e3 (2020).

227. V. Acosta-Rodríguez, F. Rijo-Ferreira, M. Izumo, P. Xu, M. Wight-Carter, C. B. Green, J. S. Takahashi, Circadian alignment of early onset caloric restriction promotes longevity in male C57BL/6J mice. *Science*. **376**, 1192–1202 (2022).

228. A. Zarrinpar, A. Chaix, S. Panda, Daily eating patterns and their impact on health and disease. *Trends Endocrinol. Metab.* **27**, 69–83 (2016).

229. Q. Tang, D. R. Assali, A. D. Güler, A. D. Steele, Dopamine systems and biological rhythms: Let's get a move on. *Front. Integr. Neurosci.* **16**, 957193 (2022).

230. C. P. Richter, A behavioristic study of the activity of the rat. *Comp. Psychol, Monog*. **1**, 1–54 (1922).

231. F. K. Stephan, J. M. Swann, C. L. Sisk, Anticipation of 24-hr feeding schedules in rats with lesions of the suprachiasmatic nucleus. *Behav. Neural Biol.* **25**, 346–363 (1979).

232. F. K. Stephan, J. M. Swann, C. L. Sisk, Entrainment of circadian rhythms by feeding schedules in rats with suprachiasmatic lesions. *Behav. Neural Biol.* **25**, 545–554 (1979).

233. A. P. Patton, M. H. Hastings, The suprachiasmatic nucleus. *Curr. Biol.* **28**, R816–R822 (2018).

234. R. E. Mistlberger, Food as circadian time cue for appetitive behavior. [version 1; peer review: 5 approved]. *F1000Res.* **9** (2020), doi:10.12688/f1000research.20829.1.

235. A. J. Davidson, Lesion studies targeting food-anticipatory activity. *Eur. J. Neurosci.* **30**, 1658–1664 (2009).

236. J. R. Trzeciak, A. D. Steele, Studying food entrainment: Models, methods, and musings. *Front. Nutr.* **9**, 998331 (2022).

237. T. C. Chou, T. E. Scammell, J. J. Gooley, S. E. Gaus, C. B. Saper, J. Lu, Critical role of dorsomedial hypothalamic nucleus in a wide range of behavioral circadian rhythms. *J. Neurosci.* **23**, 10691–10702 (2003).

238. C. L. Faber, J. D. Deem, B. A. Phan, T. P. Doan, K. Ogimoto, Z. Mirzadeh, M. W. Schwartz, G. J. Morton, Leptin receptor neurons in the dorsomedial hypothalamus regulate diurnal patterns of feeding, locomotion, and metabolism. *eLife*. **10** (2021), doi:10.7554/eLife.63671.

239. M. Verwey, Z. Khoja, J. Stewart, S. Amir, Differential regulation of the expression of Period2 protein in the limbic forebrain and dorsomedial hypothalamus by daily limited access to highly palatable food in food-deprived and free-fed rats. *Neuroscience*. **147**, 277–285 (2007).

240. G. Acosta-Galvan, C.-X. Yi, J. van der Vliet, J. H. Jhamandas, P. Panula, M. Angeles-Castellanos, M. Del Carmen Basualdo, C. Escobar, R. M. Buijs, Interaction between hypothalamic dorsomedial nucleus and the suprachiasmatic nucleus determines intensity of food anticipatory behavior. *Proc Natl Acad Sci USA*. **108**, 5813–5818 (2011).

241. D. T. Krieger, H. Hauser, L. C. Krey, Suprachiasmatic nuclear lesions do not abolish food-shifted circadian adrenal and temperature rhythmicity. *Science*. **197**, 398–399 (1977).

242. N. N. Takasu, G. Kurosawa, I. T. Tokuda, A. Mochizuki, T. Todo, W. Nakamura, Circadian regulation of food-anticipatory activity in molecular clock-deficient mice. *PLoS ONE*. **7**,

e48892 (2012).

243. D. C. Fernandez, R. Komal, J. Langel, J. Ma, P. Q. Duy, M. A. Penzo, H. Zhao, S. Hattar, Retinal innervation tunes circuits that drive nonphotic entrainment to food. *Nature*. **581**, 194–198 (2020).

244. J. Mendoza, S. Gourmelen, S. Dumont, D. Sage-Ciocca, P. Pévet, E. Challet, Setting the main circadian clock of a diurnal mammal by hypocaloric feeding. *J Physiol (Lond)*. **590**, 3155–3168 (2012).

245. J. Mendoza, C. Graff, H. Dardente, P. Pevet, E. Challet, Feeding cues alter clock gene oscillations and photic responses in the suprachiasmatic nuclei of mice exposed to a light/dark cycle. *J. Neurosci.* **25**, 1514–1522 (2005).

246. J. Mendoza, Food intake and addictive-like eating behaviors: Time to think about the circadian clock(s). *Neurosci. Biobehav. Rev.* **106**, 122–132 (2019).

247. P. Xu, S. Berto, A. Kulkarni, B. Jeong, C. Joseph, K. H. Cox, M. E. Greenberg, T.-K. Kim, G. Konopka, J. S. Takahashi, NPAS4 regulates the transcriptional response of the suprachiasmatic nucleus to light and circadian behavior. *Neuron*. **109**, 3268-3282.e6 (2021).

248. S. Wen, D. Ma, M. Zhao, L. Xie, Q. Wu, L. Gou, C. Zhu, Y. Fan, H. Wang, J. Yan, Spatiotemporal single-cell analysis of gene expression in the mouse suprachiasmatic nucleus. *Nature Neuroscience* (2020).

249. E. S. Lein, M. J. Hawrylycz, N. Ao, M. Ayres, A. Bensinger, A. Bernard, A. F. Boe, M. S. Boguski, K. S. Brockway, E. J. Byrnes, L. Chen, L. Chen, T.-M. Chen, M. C. Chin, J. Chong, B. E. Crook, A. Czaplinska, C. N. Dang, S. Datta, N. R. Dee, A. R. Jones, Genome-wide atlas of gene expression in the adult mouse brain. *Nature*. **445**, 168–176 (2007).

250. P. M. Fuller, J. Lu, C. B. Saper, Differential rescue of light- and food-entrainable circadian rhythms. *Science*. **320**, 1074–1077 (2008).

251. G. J. Landry, B. A. Kent, D. F. Patton, M. Jaholkowski, E. G. Marchant, R. E. Mistlberger, Evidence for time-of-day dependent effect of neurotoxic dorsomedial hypothalamic lesions on food anticipatory circadian rhythms in rats. *PLoS ONE*. **6**, e24187 (2011).

252. A. Rastogi, E. M. Mintz, Neural correlates of food anticipatory activity in mice subjected to once- or twice-daily feeding periods. *Eur. J. Neurosci.* **46**, 2265–2275 (2017).

253. Z. A. Knight, K. Tan, K. Birsoy, S. Schmidt, J. L. Garrison, R. W. Wysocki, A. Emiliano, M. I. Ekstrand, J. M. Friedman, Molecular profiling of activated neurons by phosphorylated ribosome capture. *Cell*. **151**, 1126–1137 (2012).

254. C. Caglar, J. Friedman, Restriction of food intake by PPP1R17-expressing neurons in the DMH. *Proc Natl Acad Sci USA*. **118** (2021), doi:10.1073/pnas.2100194118.

255. R. E. Mistlberger, S. Yamazaki, J. S. Pendergast, G. J. Landry, T. Takumi, W. Nakamura, Comment on “Differential rescue of light- and food-entrainable circadian rhythms”. *Science*. **322**, 675; author reply 675 (2008).

256. R. E. Mistlberger, R. M. Buijs, E. Challet, C. Escobar, G. J. Landry, A. Kalsbeek, P. Pevet, S. Shibata, Standards of evidence in chronobiology: critical review of a report that restoration of Bmal1 expression in the dorsomedial hypothalamus is sufficient to restore circadian food anticipatory rhythms in Bmal1-/- mice. *J. Circadian Rhythms*. **7**, 3 (2009).

257. J. S. Pendergast, W. Nakamura, R. C. Friday, F. Hatanaka, T. Takumi, S. Yamazaki, Robust food anticipatory activity in BMAL1-deficient mice. *PLoS ONE*. **4**, e4860 (2009).

258. M. Izumo, M. Pejchal, A. C. Schook, R. P. Lange, J. A. Walisser, T. R. Sato, X. Wang, C. A. Bradfield, J. S. Takahashi, Differential effects of light and feeding on circadian organization of peripheral clocks in a forebrain Bmal1 mutant. *eLife*. **3** (2014), doi:10.7554/eLife.04617.

259. S. Lee, A. L. Bookout, C. E. Lee, L. Gautron, M. J. Harper, C. F. Elias, B. B. Lowell, J. K. Elmquist, Laser-capture microdissection and transcriptional profiling of the dorsomedial nucleus of the hypothalamus. *J. Comp. Neurol.* **520**, 3617–3632 (2012).

260. A. S. Garfield, B. P. Shah, C. R. Burgess, M. M. Li, C. Li, J. S. Steger, J. C. Madara, J. N. Campbell, D. Kroeger, T. E. Scammell, B. A. Tannous, M. G. Myers, M. L. Andermann, M. J. Krashes, B. B. Lowell, Dynamic GABAergic afferent modulation of AgRP neurons. *Nat. Neurosci.* **19**, 1628–1635 (2016).

261. S. Lee, C. E. Lee, C. F. Elias, J. K. Elmquist, Expression of the diabetes-associated gene TCF7L2 in adult mouse brain. *J. Comp. Neurol.* **517**, 925–939 (2009).

262. D. W. Kim, K. Liu, Z. Q. Wang, Y. S. Zhang, A. Bathini, M. P. Brown, S. H. Lin, P. W. Washington, C. Sun, S. Lindtner, B. Lee, H. Wang, T. Shimogori, J. L. R. Rubenstein, S. Blackshaw, Gene regulatory networks controlling differentiation, survival, and diversification of hypothalamic Lhx6-expressing GABAergic neurons. *Commun. Biol.* **4**, 95 (2021).

263. H.-Y. M. Cheng, H. Dziema, J. Papp, D. P. Mathur, M. Koletar, M. R. Ralph, J. M. Penninger, K. Obrietan, The molecular gatekeeper Dexras1 sculpts the photic responsiveness of the mammalian circadian clock. *J. Neurosci.* **26**, 12984–12995 (2006).

264. J. R. M. Harvey, A. E. Plante, A. L. Meredith, Ion channels controlling circadian rhythms in suprachiasmatic nucleus excitability. *Physiol. Rev.* **100**, 1415–1454 (2020).

265. M. Díaz-Muñoz, M. A. Dent, D. Granados-Fuentes, A. C. Hall, A. Hernández-Cruz, M. E. Harrington, R. Aguilar-Roblero, Circadian modulation of the ryanodine receptor type 2 in the SCN of rodents. *Neuroreport*. **10**, 481–486 (1999).

266. D. Imoto, I. Yamamoto, H. Matsunaga, T. Yonekura, M.-L. Lee, K. X. Kato, T. Yamasaki, S. Xu, T. Ishimoto, S. Yamagata, K.-I. Otsuguro, M. Horiuchi, N. Iijima, K. Kimura, C. Toda, Refeeding activates neurons in the dorsomedial hypothalamus to inhibit food intake and promote positive valence. *Mol. Metab.* **54**, 101366 (2021).

267. J. Berrios, C. Li, J. C. Madara, A. S. Garfield, J. S. Steger, M. J. Krashes, B. B. Lowell, Food cue regulation of AGRP hunger neurons guides learning. *Nature*. **595**, 695–700 (2021).

268. C. M. Mazzone, J. Liang-Guallpa, C. Li, N. S. Wolcott, M. H. Boone, M. Southern, N. P. Kobzar, I. de A. Salgado, D. M. Reddy, F. Sun, Y. Zhang, Y. Li, G. Cui, M. J. Krashes, High-fat food biases hypothalamic and mesolimbic expression of consummatory drives. *Nat. Neurosci.* **23**, 1253–1266 (2020).

269. G. J. Landry, H. Opiol, E. G. Marchant, I. Pavlovski, R. J. Mear, D. K. Hamson, R. E. Mistlberger, Scheduled daily mating induces circadian anticipatory activity rhythms in the male rat. *PLoS ONE*. **7**, e40895 (2012).

270. D. M. Edgar, W. C. Dement, Regularly scheduled voluntary exercise synchronizes the mouse circadian clock. *Am. J. Physiol.* **261**, R928-33 (1991).

271. M. Garaulet, P. Gómez-Abellán, J. J. Alburquerque-Béjar, Y. C. Lee, J. M. Ordovás, F. A. J. L. Scheer, Timing of food intake predicts weight loss effectiveness. *Int J Obes (Lond)*. **37**, 604–611 (2013).

272. A. Chaix, T. Lin, H. D. Le, M. W. Chang, S. Panda, Time-Restricted Feeding Prevents Obesity and Metabolic Syndrome in Mice Lacking a Circadian Clock. *Cell Metab.* **29**, 303-319.e4 (2019).

273. R. M. Grippo, Q. Tang, Q. Zhang, S. R. Chadwick, Y. Gao, E. B. Altherr, L. Sipe, A. M. Purohit, N. M. Purohit, M. D. Sunkara, K. J. Cios, M. Sidikpramana, A. J. Spano, J. N. Campbell, A. D. Steele, J. Hirsh, C. D. Deppmann, M. Wu, M. M. Scott, A. D. Güler, Dopamine Signaling in the Suprachiasmatic Nucleus Enables Weight Gain Associated with Hedonic Feeding. *Curr. Biol.* **30**, 196-208.e8 (2020).

274. R. E. Mistlberger, D. J. Skene, Nonphotic entrainment in humans? *J. Biol. Rhythms*. **20**, 339–352 (2005).

275. P. Lewis, H. Oster, H. W. Korf, R. G. Foster, T. C. Erren, Food as a circadian time cue - evidence from human studies. *Nat. Rev. Endocrinol.* **16**, 213–223 (2020).

276. Z. Xie, Y. Sun, Y. Ye, D. Hu, H. Zhang, Z. He, H. Zhao, H. Yang, Y. Mao, Randomized controlled trial for time-restricted eating in healthy volunteers without obesity. *Nat. Commun.* **13**, 1003 (2022).

277. R. L. Leshan, M. Björnholm, H. Münzberg, M. G. Myers, Leptin receptor signaling and action in the central nervous system. *Obesity (Silver Spring)*. **14 Suppl 5**, 208S-212S (2006).

278. L. Madisen, T. A. Zwingman, S. M. Sunkin, S. W. Oh, H. A. Zariwala, H. Gu, L. L. Ng, R. D. Palmiter, M. J. Hawrylycz, A. R. Jones, E. S. Lein, H. Zeng, A robust and high-throughput Cre reporting and characterization system for the whole mouse brain. *Nat. Neurosci.* **13**, 133–140 (2010).

279. N. Habib, Y. Li, M. Heidenreich, L. Swiech, I. Avraham-Davidi, J. J. Trombetta, C. Hession, F. Zhang, A. Regev, Div-Seq: Single-nucleus RNA-Seq reveals dynamics of rare adult newborn neurons. *Science*. **353**, 925–928 (2016).

280. Y. Hao, S. Hao, E. Andersen-Nissen, W. M. Mauck, S. Zheng, A. Butler, M. J. Lee, A. J. Wilk, C. Darby, M. Zager, P. Hoffman, M. Stoeckius, E. Papalexi, E. P. Mimitou, J. Jain, A. Srivastava, T. Stuart, L. M. Fleming, B. Yeung, A. J. Rogers, R. Satija, Integrated

analysis of multimodal single-cell data. *Cell*. **184**, 3573-3587. (2021).

281. J. L. Michaud, F. Boucher, A. Melnyk, F. Gauthier, E. Goshu, E. Lévy, G. A. Mitchell, J. Himms-Hagen, C. M. Fan, Sim1 haploinsufficiency causes hyperphagia, obesity and reduction of the paraventricular nucleus of the hypothalamus. *Hum. Mol. Genet.* **10**, 1465–1473 (2001).

282. D. W. Kim, P. W. Washington, Z. Q. Wang, S. H. Lin, C. Sun, B. T. Ismail, H. Wang, L. Jiang, S. Blackshaw, The cellular and molecular landscape of hypothalamic patterning and differentiation from embryonic to late postnatal development. *Nat. Commun.* **11**, 4360 (2020).

283. Z. Mészár, F. Girard, C. B. Saper, M. R. Celio, The lateral hypothalamic parvalbumin-immunoreactive (PV1) nucleus in rodents. *J. Comp. Neurol.* **520**, 798–815 (2012).

284. L. E. Mickelsen, M. Bolisetty, B. R. Chimileski, A. Fujita, E. J. Beltrami, J. T. Costanzo, J. R. Naparstek, P. Robson, A. C. Jackson, Single-cell transcriptomic analysis of the lateral hypothalamic area reveals molecularly distinct populations of inhibitory and excitatory neurons. *Nat. Neurosci.* **22**, 642–656 (2019).

285. P. Panula, H. Y. Yang, E. Costa, Histamine-containing neurons in the rat hypothalamus. *Proc Natl Acad Sci USA*. **81**, 2572–2576 (1984).

286. T. Watanabe, Y. Taguchi, H. Hayashi, J. Tanaka, S. Shiosaka, M. Tohyama, H. Kubota, Y. Terano, H. Wada, Evidence for the presence of a histaminergic neuron system in the rat brain: an immunohistochemical analysis. *Neurosci. Lett.* **39**, 249–254 (1983).

287. W. D. Todd, A. Venner, C. Anaclet, R. Y. Broadhurst, R. De Luca, S. S. Bandaru, L. Issokson, L. M. Hablitz, O. Cravetchi, E. Arrigoni, J. N. Campbell, C. N. Allen, D. P. Olson, P. M. Fuller, Suprachiasmatic VIP neurons are required for normal circadian rhythmicity and comprised of molecularly distinct subpopulations. *Nat. Commun.* **11**, 4410 (2020).

288. L. Erben, M.-X. He, A. Laeremans, E. Park, A. Buonanno, A Novel Ultrasensitive In Situ Hybridization Approach to Detect Short Sequences and Splice Variants with Cellular Resolution. *Mol. Neurobiol.* **55**, 6169–6181 (2018).

289. M. Dharmalingam, U. Sriram, M. P. Baruah, Liraglutide: A review of its therapeutic use as a once daily GLP-1 analog for the management of type 2 diabetes mellitus. *Indian J. Endocrinol. Metab.* **15**, 9–17 (2011).

290. D. J. Drucker, M. A. Nauck, The incretin system: glucagon-like peptide-1 receptor agonists and dipeptidyl peptidase-4 inhibitors in type 2 diabetes. *Lancet*. **368**, 1696–1705 (2006).

291. L. B. Knudsen, J. Lau, The discovery and development of liraglutide and semaglutide. *Front Endocrinol (Lausanne)*. **10**, 155 (2019).

292. D. J. Drucker, Mechanisms of Action and Therapeutic Application of Glucagon-like Peptide-1. *Cell Metab.* **27**, 740–756 (2018).

293. R. Loomba, M. L. Hartman, E. J. Lawitz, R. Vuppalanchi, J. Boursier, E. Bugianesi, M. Yoneda, C. Behling, O. W. Cummings, Y. Tang, B. Brouwers, D. A. Robins, A. Nikooie, M. C. Bunck, A. Haupt, A. J. Sanyal, SYNERGY-NASH Investigators, Tirzepatide for Metabolic Dysfunction-Associated Steatohepatitis with Liver Fibrosis. *N. Engl. J. Med.* **391**, 299–310 (2024).

294. L. A. Abushamat, P. A. Shah, R. H. Eckel, S. A. Harrison, D. Barb, The Emerging Role of Glucagon-Like Peptide-1 Receptor Agonists for the Treatment of Metabolic Dysfunction-Associated Steatohepatitis. *Clin. Gastroenterol. Hepatol.* **22**, 1565–1574 (2024).

295. C. Bosch, S. Carriazo, M. J. Soler, A. Ortiz, B. Fernandez-Fernandez, Tirzepatide and prevention of chronic kidney disease. *Clin. Kidney J.* **16**, 797–808 (2023).

296. V. Perkovic, K. R. Tuttle, P. Rossing, K. W. Mahaffey, J. F. E. Mann, G. Bakris, F. M. M. Baeres, T. Idorn, H. Bosch-Traberg, N. L. Lausvig, R. Pratley, FLOW Trial Committees and Investigators, Effects of Semaglutide on Chronic Kidney Disease in Patients with Type 2 Diabetes. *N. Engl. J. Med.* **391**, 109–121 (2024).

297. J. Nowell, E. Blunt, P. Edison, Incretin and insulin signaling as novel therapeutic targets for Alzheimer's and Parkinson's disease. *Mol. Psychiatry*. **28**, 217–229 (2023).

298. K. O. Kopp, E. J. Glotfelty, Y. Li, N. H. Greig, Glucagon-like peptide-1 (GLP-1) receptor agonists and neuroinflammation: Implications for neurodegenerative disease treatment. *Pharmacol. Res.* **186**, 106550 (2022).

299. D. J. Drucker, The benefits of GLP-1 drugs beyond obesity. *Science*. **385**, 258–260 (2024).

300. W. Wang, N. D. Volkow, N. A. Berger, P. B. Davis, D. C. Kaelber, R. Xu, Associations of semaglutide with incidence and recurrence of alcohol use disorder in real-world population. *Nat. Commun.* **15**, 4548 (2024).

301. F. Quddos, Z. Hubshman, A. Tegge, D. Sane, E. Marti, A. S. Kablinger, K. M. Gatchalian, A. L. Kelly, A. G. DiFeliceantonio, W. K. Bickel, Semaglutide and Tirzepatide reduce alcohol consumption in individuals with obesity. *Sci. Rep.* **13**, 20998 (2023).

302. W. Wang, N. D. Volkow, N. A. Berger, P. B. Davis, D. C. Kaelber, R. Xu, Association of semaglutide with reduced incidence and relapse of cannabis use disorder in real-world populations: a retrospective cohort study. *Mol. Psychiatry*. **29**, 2587–2598 (2024).

303. D. Arillotta, G. Floresta, G. D. Papanti Pelletier, A. Guirguis, J. M. Corkery, G. Martinotti, F. Schifano, Exploring the Potential Impact of GLP-1 Receptor Agonists on Substance Use, Compulsive Behavior, and Libido: Insights from Social Media Using a Mixed-Methods Approach. *Brain Sci.* **14** (2024), doi:10.3390/brainsci14060617.

304. L. L. Baggio, D. J. Drucker, Glucagon-like peptide-1 receptors in the brain: controlling food intake and body weight. *The Journal of Clinical Investigation* (2014).

305. C. B. G. Salinas, T. T.-H. Lu, S. Gabery, K. Marstal, T. Alanentalo, A. J. Mercer, A. Cornea, K. Conradsen, J. Hecksher-Sørensen, A. B. Dahl, L. B. Knudsen, A. Secher, Integrated brain atlas for unbiased mapping of nervous system effects following

liraglutide treatment. *Sci. Rep.* **8**, 10310 (2018).

306. A. Secher, J. Jelsing, A. F. Baquero, J. Hecksher-Sørensen, M. A. Cowley, L. S. Dalbøge, G. Hansen, K. L. Grove, C. Pyke, K. Raun, L. Schäffer, M. Tang-Christensen, S. Verma, B. M. Witgen, N. Vrang, L. Bjerre Knudsen, The arcuate nucleus mediates GLP-1 receptor agonist liraglutide-dependent weight loss. *J. Clin. Invest.* **124**, 4473–4488 (2014).

307. S. Sisley, R. Gutierrez-Aguilar, M. Scott, D. A. D'Alessio, D. A. Sandoval, R. J. Seeley, Neuronal GLP1R mediates liraglutide's anorectic but not glucose-lowering effect. *The Journal of Clinical Investigation* (2014).

308. J. M. Adams, H. Pei, D. A. Sandoval, R. J. Seeley, R. B. Chang, S. D. Liberles, D. P. Olson, Liraglutide Modulates Appetite and Body Weight Through Glucagon-Like Peptide 1 Receptor-Expressing Glutamatergic Neurons. *Diabetes*. **67**, 1538–1548 (2018).

309. K.-P. Huang, A. A. Acosta, M. Y. Ghidewon, A. D. McKnight, M. S. Almeida, N. T. Nyema, N. D. Hanchak, N. Patel, Y. S. K. Gbenou, A. E. Adriaenssens, K. A. Bolding, A. L. Alhadeff, Dissociable hindbrain GLP1R circuits for satiety and aversion. *Nature*. **632**, 585–593 (2024).

310. K. S. Kim, J. S. Park, E. Hwang, M. J. Park, H. Y. Shin, Y. H. Lee, K. M. Kim, L. Gautron, E. Godschall, B. Portillo, K. Grose, S.-H. Jung, S. L. Baek, Y. H. Yun, D. Lee, E. Kim, J. Ajwani, S. H. Yoo, A. D. Güler, K. W. Williams, H. J. Choi, GLP-1 increases preingestive satiation via hypothalamic circuits in mice and humans. *Science*. **385**, 438–446 (2024).

311. A. N. Webster, J. J. Becker, C. Li, D. C. Schwalbe, D. Kerspern, E. O. Karolczak, C. Bundon, R. A. Onoharigho, M. Crook, M. Jalil, E. N. Godschall, E. G. Dame, A. Dawer, D. M. Belmont-Rausch, T. H. Pers, A. Lutas, N. Habib, A. D. Guler, M. J. Krashes, J. N. Campbell, Molecular Connectomics Reveals a Glucagon-Like Peptide 1 Sensitive Neural Circuit for Satiety. *BioRxiv* (2024), doi:10.1101/2023.10.31.564990.

312. FDA clarifies policies for compounders as national GLP-1 supply begins to stabilize | FDA, (available at https://www.fda.gov/drugs/drug-safety-and-availability/fda-clarifies-policies-compounders-national-glp-1-supply-begins-stabilize).

313. H. P. Whitley, J. M. Trujillo, J. J. Neumiller, Special Report: Potential Strategies for Addressing GLP-1 and Dual GLP-1/GIP Receptor Agonist Shortages. *Clin. Diabetes*. **41**, 467–473 (2023).

314. C. Chandrashekar, F. Lin, Y. Nishiuchi, S. F. Mohammed, B. F. White, Y. Arsenakis, E. Yuliantie, P. Zhao, S. van Dun, A. Koijen, Y. Kajihara, D. Wootten, G. T. Dodd, L. J. van den Bos, J. D. Wade, M. A. Hossain, Engineering of a Biologically Active Glycosylated Glucagon-Like Peptide-1 Analogue. *J. Med. Chem.* **67**, 7276–7282 (2024).

315. G. R. Barredo‐Vacchelli, J. A. Rodríguez, J. A. Eloy, S. A. Camperi, A novel method for liraglutide synthesis and purification. *Peptide Science*. **116** (2024), doi:10.1002/pep2.24351.

316. J. He, Y. Chu, Small-molecule GLP-1 secretagogs: challenges and recent advances.

Drug Discov. Today (2020), doi:10.1016/j.drudis.2020.08.003.

317. Dave Ricks, CEO of Eli Lilly | The All-In Interview - YouTube, (available at https://youtu.be/023exhA9irY?si=zvw1aQ6cVXtNlfy5&t=2181).

318. S. Wharton, T. Blevins, L. Connery, J. Rosenstock, S. Raha, R. Liu, X. Ma, K. J. Mather, A. Haupt, D. Robins, E. Pratt, C. Kazda, M. Konig, GZGI Investigators, Daily Oral GLP-1 Receptor Agonist Orforglipron for Adults with Obesity. *N. Engl. J. Med.* **389**, 877–888 (2023).

319. D. Dutta, L. Nagendra, B. Anne, M. Kumar, M. Sharma, A. B. M. Kamrul-Hasan, Orforglipron, a novel non-peptide oral daily glucagon-like peptide-1 receptor agonist as an anti-obesity medicine: A systematic review and meta-analysis. *Obes. Sci. Pract.* **10**, e743 (2024).

320. Eli Lilly and Company Q3 2024 Earnings Call. *Eli Lilly and Company Q3 2024 Earnings Call* (2024), (available at https://investor.lilly.com/static-files/cdedba2e-c4a7-4047-9e61-4ac3b1e2cd73).

321. A. R. Saxena, D. N. Gorman, R. M. Esquejo, A. Bergman, K. Chidsey, C. Buckeridge, D. A. Griffith, A. M. Kim, Danuglipron (PF-06882961) in type 2 diabetes: a randomized, placebo-controlled, multiple ascending-dose phase 1 trial. *Nat. Med.* **27**, 1079–1087 (2021).

322. A. R. Saxena, J. P. Frias, L. S. Brown, D. N. Gorman, S. Vasas, N. Tsamandouras, M. J. Birnbaum, Efficacy and Safety of Oral Small Molecule Glucagon-Like Peptide 1 Receptor Agonist Danuglipron for Glycemic Control Among Patients With Type 2 Diabetes: A Randomized Clinical Trial. *JAMA Netw. Open*. **6**, e2314493 (2023).

323. D. A. Griffith, D. J. Edmonds, J.-P. Fortin, A. S. Kalgutkar, J. B. Kuzmiski, P. M. Loria, A. R. Saxena, S. W. Bagley, C. Buckeridge, J. M. Curto, D. R. Derksen, J. M. Dias, M. C. Griffor, S. Han, V. M. Jackson, M. S. Landis, D. Lettiere, C. Limberakis, Y. Liu, A. M. Mathiowetz, D. A. Tess, A Small-Molecule Oral Agonist of the Human Glucagon-like Peptide-1 Receptor. *J. Med. Chem.* **65**, 8208–8226 (2022).

324. X. Zhang, M. J. Belousoff, P. Zhao, A. J. Kooistra, T. T. Truong, S. Y. Ang, C. R. Underwood, T. Egebjerg, P. Šenel, G. D. Stewart, Y.-L. Liang, A. Glukhova, H. Venugopal, A. Christopoulos, S. G. B. Furness, L. J. Miller, S. Reedtz-Runge, C. J. Langmead, D. E. Gloriam, R. Danev, D. Wootten, Differential GLP-1R Binding and Activation by Peptide and Non-peptide Agonists. *Mol. Cell*. **80**, 485-500.e7 (2020).

325. T. Kawai, B. Sun, H. Yoshino, D. Feng, Y. Suzuki, M. Fukazawa, S. Nagao, D. B. Wainscott, A. D. Showalter, B. A. Droz, T. S. Kobilka, M. P. Coghlan, F. S. Willard, Y. Kawabe, B. K. Kobilka, K. W. Sloop, Structural basis for GLP-1 receptor activation by LY3502970, an orally active nonpeptide agonist. *Proc Natl Acad Sci USA*. **117**, 29959–29967 (2020).

326. Search for: Other terms: orforglipron, Phase: 3 | Card Results | ClinicalTrials.gov, (available at https://clinicaltrials.gov/search?term=orforglipron&aggFilters=phase:3).

327. D. Arillotta, G. Floresta, A. Guirguis, J. M. Corkery, V. Catalani, G. Martinotti, S. L. Sensi,

F. Schifano, GLP-1 Receptor Agonists and Related Mental Health Issues; Insights from a Range of Social Media Platforms Using a Mixed-Methods Approach. *Brain Sci.* **13** (2023), doi:10.3390/brainsci13111503.

328. E. Kornelius, J.-Y. Huang, S.-C. Lo, C.-N. Huang, Y.-S. Yang, The risk of depression, anxiety, and suicidal behavior in patients with obesity on glucagon like peptide-1 receptor agonist therapy. *Sci. Rep.* **14**, 24433 (2024).

329. X. Chen, P. Zhao, W. Wang, L. Guo, Q. Pan, The Antidepressant Effects of GLP-1 Receptor Agonists: A Systematic Review and Meta-Analysis. *Am. J. Geriatr. Psychiatry*. **32**, 117–127 (2024).

330. J. A. Engel, E. Jerlhag, Role of appetite-regulating peptides in the pathophysiology of addiction: implications for pharmacotherapy. *CNS Drugs*. **28**, 875–886 (2014).

331. K. P. Skibicka, The central GLP-1: implications for food and drug reward. *Front. Neurosci.* **7**, 181 (2013).

332. S. Falk, J. Petersen, C. Svendsen, C. R. Romero-Leguizamón, S. H. Jørgensen, N. Krauth, M. Q. Ludwig, K. Lundø, U. Roostalu, G. Skovbjerg, D. A. G. Nielsen, A. L. Ejdrup, T. H. Pers, O. Dmytriyeva, J. Hecksher-Sørensen, U. Gether, K. A. Kohlmeier, C. Clemmensen, GLP-1 and nicotine combination therapy engages hypothalamic and mesolimbic pathways to reverse obesity. *Cell Rep.* **42**, 112466 (2023).

333. C. M. Liu, S. E. Kanoski, Homeostatic and non-homeostatic controls of feeding behavior: Distinct vs. common neural systems. *Physiol. Behav.* **193**, 223–231 (2018).

334. S. Gabery, C. G. Salinas, S. J. Paulsen, J. Ahnfelt-Rønne, T. Alanentalo, A. F. Baquero, S. T. Buckley, E. Farkas, C. Fekete, K. S. Frederiksen, H. C. C. Helms, J. F. Jeppesen, L. M. John, C. Pyke, J. Nøhr, T. T. Lu, J. Polex-Wolf, V. Prevot, K. Raun, L. Simonsen, W. F. J. Hogendorf, Semaglutide lowers body weight in rodents via distributed neural pathways. *JCI Insight*. **5** (2020), doi:10.1172/jci.insight.133429.

335. J. Liu, K. Conde, P. Zhang, V. Lilascharoen, Z. Xu, B. K. Lim, R. J. Seeley, J. J. Zhu, M. M. Scott, Z. P. Pang, Enhanced AMPA Receptor Trafficking Mediates the Anorexigenic Effect of Endogenous Glucagon-like Peptide-1 in the Paraventricular Hypothalamus. *Neuron*. **96**, 897-909.e5 (2017).

336. A. L. Alhadeff, B. D. Mergler, D. J. Zimmer, C. A. Turner, D. J. Reiner, H. D. Schmidt, H. J. Grill, M. R. Hayes, Endogenous Glucagon-like Peptide-1 Receptor Signaling in the Nucleus Tractus Solitarius is Required for Food Intake Control. *Neuropsychopharmacology*. **42**, 1471–1479 (2017).

337. N. Zeng, E. J. Cutts, C. B. Lopez, S. Kaur, M. Duran, S. A. Virkus, J. A. Hardaway, Anatomical and Functional Characterization of Central Amygdala Glucagon-Like Peptide 1 Receptor Expressing Neurons. *Front. Behav. Neurosci.* **15**, 724030 (2021).

338. H. H. Hansen, J. Perens, U. Roostalu, J. L. Skytte, C. G. Salinas, P. Barkholt, D. D. Thorbek, K. T. G. Rigbolt, N. Vrang, J. Jelsing, J. Hecksher-Sørensen, Whole-brain activation signatures of weight-lowering drugs. *Mol. Metab.* **47**, 101171 (2021).

339. J. Petersen, M. Q. Ludwig, V. Juozaityte, P. Ranea-Robles, C. Svendsen, E. Hwang, A.

W. Kristensen, N. Fadahunsi, J. Lund, A. W. Breum, C. V. Mathiesen, L. Sachs, R. Moreno-Justicia, R. Rohlfs, J. C. Ford, J. D. Douros, B. Finan, B. Portillo, K. Grose, J. E. Petersen, C. Clemmensen, GLP-1-directed NMDA receptor antagonism for obesity treatment. *Nature*. **629**, 1133–1141 (2024).

340. C. Zhang, J. A. Kaye, Z. Cai, Y. Wang, S. L. Prescott, S. D. Liberles, Area Postrema Cell Types that Mediate Nausea-Associated Behaviors. *Neuron*. **109**, 461-472.e5 (2021).

341. Pfizer Nixes Twice-Daily Oral GLP-1 Candidate After High Rates of Side Effects - BioSpace, (available at https://www.biospace.com/pfizer-nixes-twice-daily-oral-glp-1-candidate-after-high-rates-of-side-effects).

342. M. E. J. Lean, R. Carraro, N. Finer, H. Hartvig, M. L. Lindegaard, S. Rössner, L. Van Gaal, A. Astrup, NN8022-1807 Investigators, Tolerability of nausea and vomiting and associations with weight loss in a randomized trial of liraglutide in obese, non-diabetic adults. *Int J Obes (Lond)*. **38**, 689–697 (2014).

343. T. D. Pereira, N. Tabris, A. Matsliah, D. M. Turner, J. Li, S. Ravindranath, E. S. Papadoyannis, E. Normand, D. S. Deutsch, Z. Y. Wang, G. C. McKenzie-Smith, C. C. Mitelut, M. D. Castro, J. D'Uva, M. Kislin, D. H. Sanes, S. D. Kocher, S. S.-H. Wang, A. L. Falkner, J. W. Shaevitz, M. Murthy, SLEAP: A deep learning system for multi-animal pose tracking. *Nat. Methods*. **19**, 486–495 (2022).

344. C. Weinreb, J. E. Pearl, S. Lin, M. A. M. Osman, L. Zhang, S. Annapragada, E. Conlin, R. Hoffmann, S. Makowska, W. F. Gillis, M. Jay, S. Ye, A. Mathis, M. W. Mathis, T. Pereira, S. W. Linderman, S. R. Datta, Keypoint-MoSeq: parsing behavior by linking point tracking to pose dynamics. *Nat. Methods*. **21**, 1329–1339 (2024).

345. R. J. Rodgers, P. Holch, A. J. Tallett, Behavioural satiety sequence (BSS): separating wheat from chaff in the behavioural pharmacology of appetite. *Pharmacol. Biochem. Behav.* **97**, 3–14 (2010).

346. S. J. Lee, G. Sanchez-Watts, J.-P. Krieger, A. Pignalosa, P. N. Norell, A. Cortella, K. G. Pettersen, D. Vrdoljak, M. R. Hayes, S. E. Kanoski, W. Langhans, A. G. Watts, Loss of dorsomedial hypothalamic GLP-1 signaling reduces BAT thermogenesis and increases adiposity. *Mol. Metab.* **11**, 33–46 (2018).

347. K. G. Harikumar, D. Wootten, D. I. Pinon, C. Koole, A. M. Ball, S. G. B. Furness, B. Graham, M. Dong, A. Christopoulos, L. J. Miller, P. M. Sexton, Glucagon-like peptide-1 receptor dimerization differentially regulates agonist signaling but does not affect small molecule allostery. *Proc Natl Acad Sci USA*. **109**, 18607–18612 (2012).

348. H. J. Choe, Y. M. Cho, Peptidyl and Non-Peptidyl Oral Glucagon-Like Peptide-1 Receptor Agonists. *Endocrinol Metab (Seoul)*. **36**, 22–29 (2021).

349. Z. Zheng, Y. Zong, Y. Ma, Y. Tian, Y. Pang, C. Zhang, J. Gao, Glucagon-like peptide-1 receptor: mechanisms and advances in therapy. *Signal Transduct. Target. Ther.* **9**, 234 (2024).

350. H. Zhang, T. Wu, Y. Wu, Y. Peng, X. Wei, T. Lu, Y. Jiao, Binding sites and design

strategies for small molecule GLP-1R agonists. *Eur. J. Med. Chem.* **275**, 116632 (2024).

351. H. Wang, R. Lou, Y. Wang, L. Hao, Q. Wang, R. Li, J. Su, S. Liu, X. Zhou, X. Gao, Q. Hao, Z. Chen, Y. Xu, C. Wu, Y. Zheng, Q. Guo, L. Bai, Parallel gut-to-brain pathways orchestrate feeding behaviors. *Nat. Neurosci.* (2024), doi:10.1038/s41593-024-01828-8.

352. A. L. Alhadeff, L. E. Rupprecht, M. R. Hayes, GLP-1 neurons in the nucleus of the solitary tract project directly to the ventral tegmental area and nucleus accumbens to control for food intake. *Endocrinology*. **153**, 647–658 (2012).

353. A. L. Alhadeff, H. J. Grill, Hindbrain nucleus tractus solitarius glucagon-like peptide-1 receptor signaling reduces appetitive and motivational aspects of feeding. *Am. J. Physiol. Regul. Integr. Comp. Physiol.* **307**, R465-70 (2014).

354. R. Merkel, N. Hernandez, V. Weir, Y. Zhang, M. T. Rich, R. C. Crist, B. C. Reiner, H. D. Schmidt, An endogenous GLP-1 circuit engages VTA GABA neurons to regulate mesolimbic dopamine neurons and attenuate cocaine seeking. *BioRxiv* (2024), doi:10.1101/2024.06.20.599574.

355. A. N. Webster, J. J. Becker, C. Li, D. C. Schwalbe, D. Kerspern, E. O. Karolczak, C. B. Bundon, R. A. Onoharigho, M. Crook, M. Jalil, E. N. Godschall, E. G. Dame, A. Dawer, D. M. Belmont-Rausch, T. H. Pers, A. Lutas, N. Habib, A. D. Güler, M. J. Krashes, J. N. Campbell, Molecular connectomics reveals a glucagon-like peptide 1-sensitive neural circuit for satiety. *Nat. Metab.* **6**, 2354–2373 (2024).

356. S. Sisley, R. Gutierrez-Aguilar, M. Scott, D. A. D'Alessio, D. A. Sandoval, R. J. Seeley, Neuronal GLP1R mediates liraglutide's anorectic but not glucose-lowering effect. *J. Clin. Invest.* **124**, 2456–2463 (2014).

357. S. M. Fortin, M. F. Roitman, Central GLP-1 receptor activation modulates cocaine-evoked phasic dopamine signaling in the nucleus accumbens core. *Physiol. Behav.* **176**, 17–25 (2017).

358. E. Egecioglu, J. A. Engel, E. Jerlhag, The glucagon-like peptide 1 analogue Exendin-4 attenuates the nicotine-induced locomotor stimulation, accumbal dopamine release, conditioned place preference as well as the expression of locomotor sensitization in mice. *PLoS ONE*. **8**, e77284 (2013).

359. P. J. Kenny, Reward mechanisms in obesity: new insights and future directions. *Neuron*. **69**, 664–679 (2011).

360. M. K. Klausen, M. Thomsen, G. Wortwein, A. Fink-Jensen, The role of glucagon-like peptide 1 (GLP-1) in addictive disorders. *Br. J. Pharmacol.* **179**, 625–641 (2022).

361. D. Vallöf, P. Maccioni, G. Colombo, M. Mandrapa, J. W. Jörnulf, E. Egecioglu, J. A. Engel, E. Jerlhag, The glucagon-like peptide 1 receptor agonist liraglutide attenuates the reinforcing properties of alcohol in rodents. *Addict. Biol.* **21**, 422–437 (2016).

362. F. Alex, G. ALEX, RE. GRAMFORTINRIA. F. Bertr, T. BERTR, THIRION, Scikit-learn: Machine Learning in Python.

363. A. B. Wiltschko, T. Tsukahara, A. Zeine, R. Anyoha, W. F. Gillis, J. E. Markowitz, R. E.

Peterson, J. Katon, M. J. Johnson, S. R. Datta, Revealing the structure of pharmacobehavioral space through motion sequencing. *Nat. Neurosci.* **23**, 1433–1443 (2020).

364. M. Ottolini, B. S. Barker, R. P. Gaykema, M. H. Meisler, M. K. Patel, Aberrant sodium channel currents and hyperexcitability of medial entorhinal cortex neurons in a mouse model of SCN8A encephalopathy. *J. Neurosci.* **37**, 7643–7655 (2017).

365. E. R. Wengert, R. M. Miralles, K. C. A. Wedgwood, P. K. Wagley, S. M. Strohm, P. S. Panchal, A. M. Idrissi, I. C. Wenker, J. A. Thompson, R. P. Gaykema, M. K. Patel, Somatostatin-Positive Interneurons Contribute to Seizures in SCN8A Epileptic Encephalopathy. *J. Neurosci.* **41**, 9257–9273 (2021).

366. R. K. A. Bunton-Stasyshyn, J. L. Wagnon, E. R. Wengert, B. S. Barker, A. Faulkner, P. K. Wagley, K. Bhatia, J. M. Jones, M. R. Maniaci, J. M. Parent, H. P. Goodkin, M. K. Patel, M. H. Meisler, Prominent role of forebrain excitatory neurons in SCN8A encephalopathy. *Brain*. **142**, 362–375 (2019).

367. J. R. Jones, T. Simon, L. Lones, E. D. Herzog, SCN VIP Neurons Are Essential for Normal Light-Mediated Resetting of the Circadian System. *J. Neurosci.* **38**, 7986–7995 (2018).

368. P. Botta, A. Fushiki, A. M. Vicente, L. A. Hammond, A. C. Mosberger, C. R. Gerfen, D. Peterka, R. M. Costa, An Amygdala Circuit Mediates Experience-Dependent Momentary Arrests during Exploration. *Cell*. **183**, 605-619.e22 (2020).

369. The increase in appetite for obesity drugs | J.P. Morgan Research, (available at https://www.jpmorgan.com/insights/global-research/current-events/obesity-drugs).

370. L. Wang, Designing a Dual GLP-1R/GIPR Agonist from Tirzepatide: Comparing Residues Between Tirzepatide, GLP-1, and GIP. *Drug Des. Devel. Ther.* **16**, 1547–1559 (2022).

371. M. Chakravarthy, F. A. Argüelles-Tello, A. L. A. Sun, M. Elliott, L. Acosta, J. E. Rankin, S. K. Hansen, 75-LB: CT-388, a Novel Once-Weekly Dual GLP-1 and GIP Receptor Modulator, Is Safe, Well-Tolerated, and Produces More than 8% Weight Loss in Four Weeks in Overweight and Obese Adults. *Diabetes*. **72** (2023), doi:10.2337/db23-75-LB.

372. H. Wan, N. Xu, L. Wang, Y. Liu, S. Fatahi, M. H. Sohouli, N. S. Guimarães, Effect of survodutide, a glucagon and GLP-1 receptor dual agonist, on weight loss: a meta-analysis of randomized controlled trials. *Diabetol. Metab. Syndr.* **16**, 264 (2024).

373. M. M. Véniant, S.-C. Lu, L. Atangan, R. Komorowski, S. Stanislaus, Y. Cheng, B. Wu, J. R. Falsey, T. Hager, V. A. Thomas, M. Ambhaikar, L. Sharpsten, Y. Zhu, V. Kurra, R. Jeswani, R. K. Oberoi, J. R. Parnes, N. Honarpour, J. Neutel, J. L. Strande, A GIPR antagonist conjugated to GLP-1 analogues promotes weight loss with improved metabolic parameters in preclinical and phase 1 settings. *Nat. Metab.* **6**, 290–303 (2024).

374. A. M. Jastreboff, L. M. Kaplan, J. P. Frías, Q. Wu, Y. Du, S. Gurbuz, T. Coskun, A. Haupt, Z. Milicevic, M. L. Hartman, Retatrutide Phase 2 Obesity Trial Investigators,

Triple-Hormone-Receptor Agonist Retatrutide for Obesity - A Phase 2 Trial. *N. Engl. J. Med.* **389**, 514–526 (2023).

375. E. Pratt, X. Ma, R. Liu, D. Robins, T. Coskun, K. W. Sloop, A. Haupt, C. Benson, Orforglipron (LY3502970), a novel, oral non-peptide glucagon-like peptide-1 receptor agonist: A Phase 1b, multicentre, blinded, placebo-controlled, randomized, multiple-ascending-dose study in people with type 2 diabetes. *Diabetes Obes. Metab.* **25**, 2642–2649 (2023).

376. J. Crawford, A. S. Dobs, W. J. Evans, C. Prado, D. Rodriguez, I. Shalev, K. Gary Barnette, M. Steiner, 2066-LB: Potential to Optimize Weight Loss with Enobosarm—Meta-analysis of Body Composition from Three Randomized Clinical Trials Support the Ability of Enobosarm to Preserve Muscle while Reducing Fat. *Diabetes*. **73** (2024), doi:10.2337/db24-2066-LB.

377. J. P. Frias, S. Deenadayalan, L. Erichsen, F. K. Knop, I. Lingvay, S. Macura, C. Mathieu, S. D. Pedersen, M. Davies, Efficacy and safety of co-administered once-weekly cagrilintide 2·4 mg with once-weekly semaglutide 2·4 mg in type 2 diabetes: a multicentre, randomised, double-blind, active-controlled, phase 2 trial. *Lancet*. **402**, 720–730 (2023).

378. J. O. N. Griffin, U. Hövelmann, A. E. Melgaard, S. Macura, M. Hammer, T. Johansen, M. B. Olsen, 1668-P: Novel Once-Weekly Amylin Analog Petrelintide (ZP8396) Is Well Tolerated with Improved GI Tolerability after Multiple Dosing. *Diabetes*. **73** (2024), doi:10.2337/db24-1668-P.

379. A. G. Niethammer, Z. Zheng, A. Timmer, T.-L. Lee, First-in-Human Evaluation of Oral Denatonium Acetate (ARD-101), a Potential Bitter Taste Receptor Agonist: A Randomized, Double-Blind, Placebo-Controlled Phase 1 Trial in Healthy Adults. *Clin. Pharmacol. Drug Dev.* **11**, 997–1006 (2022).

380. M. H. Jensen, S. J. Sanni, D. Riber, J. J. Holst, M. M. Rosenkilde, A. H. Sparre-Ulrich, AT-7687, a novel GIPR peptide antagonist, combined with a GLP-1 agonist, leads to enhanced weight loss and metabolic improvements in cynomolgus monkeys. *Mol. Metab.* **88**, 102006 (2024).

381. P. Shah, M. White, A. Sievert, A. Conway, A. Kneepkens, G. Sayuk, M. Lisker-Melman, J. Elwing, Semaglutide improves metabolic dysfunction-associated steatohepatitis: A 10-year retrospective study. *JGH Open*. **8**, e13037 (2024).

382. P. N. Newsome, K. Buchholtz, K. Cusi, M. Linder, T. Okanoue, V. Ratziu, A. J. Sanyal, A.-S. Sejling, S. A. Harrison, NN9931-4296 Investigators, A Placebo-Controlled Trial of Subcutaneous Semaglutide in Nonalcoholic Steatohepatitis. *N. Engl. J. Med.* **384**, 1113–1124 (2021).

383. E. M. Apperloo, J. L. Gorriz, M. J. Soler, S. Cigarrán Guldris, J. M. Cruzado, M. J. Puchades, M. López-Martínez, F. Waanders, G. D. Laverman, A. van der Aart-van der Beek, K. Hoogenberg, A. P. van Beek, J. Verhave, S. B. Ahmed, R. E. Schmieder, C. Wanner, D. Z. I. Cherney, N. Jongs, H. J. L. Heerspink, Semaglutide in patients with overweight or obesity and chronic kidney disease without diabetes: a randomized

double-blind placebo-controlled clinical trial. *Nat. Med.* **31**, 278–285 (2025).

384. A. Malhotra, R. R. Grunstein, I. Fietze, T. E. Weaver, S. Redline, A. Azarbarzin, S. A. Sands, R. J. Schwab, J. P. Dunn, S. Chakladar, M. C. Bunck, J. Bednarik, SURMOUNT-OSA Investigators, Tirzepatide for the treatment of obstructive sleep apnea and obesity. *N. Engl. J. Med.* **391**, 1193–1205 (2024).

385. M.-H. Chuang, J.-Y. Chen, H.-Y. Wang, Z.-H. Jiang, V.-C. Wu, Clinical Outcomes of Tirzepatide or GLP-1 Receptor Agonists in Individuals With Type 2 Diabetes. *JAMA Netw. Open*. **7**, e2427258 (2024).

386. M. Packer, M. R. Zile, C. M. Kramer, S. J. Baum, S. E. Litwin, V. Menon, J. Ge, G. J. Weerakkody, Y. Ou, M. C. Bunck, K. C. Hurt, M. Murakami, B. A. Borlaug, SUMMIT Trial Study Group, Tirzepatide for Heart Failure with Preserved Ejection Fraction and Obesity. *N. Engl. J. Med.* **392**, 427–437 (2025).

387. A. M. Lincoff, K. Brown-Frandsen, H. M. Colhoun, J. Deanfield, S. S. Emerson, S. Esbjerg, S. Hardt-Lindberg, G. K. Hovingh, S. E. Kahn, R. F. Kushner, I. Lingvay, T. K. Oral, M. M. Michelsen, J. Plutzky, C. W. Tornøe, D. H. Ryan, SELECT Trial Investigators, Semaglutide and Cardiovascular Outcomes in Obesity without Diabetes. *N. Engl. J. Med.* **389**, 2221–2232 (2023).

388. W. Wang, Q. Wang, X. Qi, M. Gurney, G. Perry, N. D. Volkow, P. B. Davis, D. C. Kaelber, R. Xu, Associations of semaglutide with first-time diagnosis of Alzheimer's disease in patients with type 2 diabetes: Target trial emulation using nationwide real-world data in the US. *Alzheimers Dement*. **20**, 8661–8672 (2024).

389. Y. Zhang, C. Tang, Y. He, Y. Zhang, Q. Li, T. Zhang, B. Zhao, A. Tong, Q. Zhong, Z. Zhong, Semaglutide ameliorates Alzheimer's disease and restores oxytocin in APP/PS1 mice and human brain organoid models. *Biomed. Pharmacother.* **180**, 117540 (2024).

390. W. G. Meissner, P. Remy, C. Giordana, D. Maltête, P. Derkinderen, J.-L. Houéto, M. Anheim, I. Benatru, T. Boraud, C. Brefel-Courbon, N. Carrière, H. Catala, O. Colin, J.-C. Corvol, P. Damier, E. Dellapina, D. Devos, S. Drapier, M. Fabbri, V. Ferrier, LIXIPARK Study Group, Trial of lixisenatide in early parkinson's disease. *N. Engl. J. Med.* **390**, 1176–1185 (2024).

391. D. Adam, Diabetes drug slows development of Parkinson's disease. *Nature* (2024), doi:10.1038/d41586-024-00974-0.

392. N. D. Volkow, R. Xu, GLP‐1R agonist medications for addiction treatment. *Addiction*. **120**, 198–200 (2025).

393. S. Martinelli, A. Mazzotta, M. Longaroni, N. Petrucciani, Potential role of glucagon-like peptide-1 (GLP-1) receptor agonists in substance use disorder: A systematic review of randomized trials. *Drug Alcohol Depend.* **264**, 112424 (2024).

394. E. N. Godschall, T. B. Gungul, I. R. Sajonia, A. K. Buyukaksakal, S. Ogilvie, A. B. Keeler, Y. Zhang, T. C. J. Deutsch, Y. Shi, N. J. Conley, A. N. Webster, O. Y. Calhan, A. Akkoub, K. Malik, K. I. West, A. Karthikeyan, G. van Gerven, M. K. Patel, J. N. Campbell, C. D. Deppmann, A. D. Güler, A Brain Reward Circuit Inhibited By Next-Generation Weight

Loss Drugs. *BioRxiv* (2024), doi:10.1101/2024.12.12.628169.

395. T. D. Filippatos, T. V. Panagiotopoulou, M. S. Elisaf, Adverse Effects of GLP-1 Receptor Agonists. *Rev. Diabet. Stud.* **11**, 202–230 (2014).

396. Y. Xie, T. Choi, Z. Al-Aly, Mapping the effectiveness and risks of GLP-1 receptor agonists. *Nat. Med.* (2025), doi:10.1038/s41591-024-03412-w.

397. D. P. Cardinali, G. M. Brown, S. R. Pandi-Perumal, Chronotherapy. *Handb. Clin. Neurol.* **179**, 357–370 (2021).

398. K. Wang, Y. Sun, P. Lin, J. Song, R. Zhao, W. Li, X. Hou, C. Wang, L. Wang, P. Zhu, L. Chen, Liraglutide activates AMPK signaling and partially restores normal circadian rhythm and insulin secretion in pancreatic islets in diabetic mice. *Biol. Pharm. Bull.* **38**, 1142–1149 (2015).

399. J. Fang, P. Miller, P. S. Grigson, Sleep is increased by liraglutide, a glucagon-like peptide-1 receptor agonist, in rats. *Brain Res. Bull.* **192**, 142–155 (2023).

400. R. Salgado-Delgado, M. Angeles-Castellanos, N. Saderi, R. M. Buijs, C. Escobar, Food intake during the normal activity phase prevents obesity and circadian desynchrony in a rat model of night work. *Endocrinology*. **151**, 1019–1029 (2010).

401. D. Daniels, E. G. Mietlicki-Baase, Glucagon-Like Peptide 1 in the Brain: Where Is It Coming From, Where Is It Going? *Diabetes*. **68**, 15–17 (2019).

402. S. C. Cork, J. E. Richards, M. K. Holt, F. M. Gribble, F. Reimann, S. Trapp, Distribution and characterisation of Glucagon-like peptide-1 receptor expressing cells in the mouse brain. *Mol. Metab.* **4**, 718–731 (2015).